Investigation on Aspheric Surface Polishing with a Doughnut-Shaped Magnetic Compound Fluid (MCF) Tool

ドーナツ型磁気混合流体（MCF）ツールを用いた非球面研磨の研究

By

Ming Feng

Submitted in Partial Fulfillment

of

the Requirements for

the Degree Doctor of Philosophy

Supervised by

Professor Teruo Bitoh

Graduate School of Systems Science and Technology

Akita Prefectural University

Akita, Japan

November 2019

Contents

Abstract

Aspheric elements have become essential optical surfaces for modifying optical systems due to their abilities to enhance the imaging quality. However, the tool marks and sub-damage were remained inevitably by the pre-manufacture techniques, such as the single point diamond turning (SDPT) and the high precision grinding. In order to improve the surface quality, the polishing process was demanded to eliminate these defects. The magnetic field-assisted polishing method was prominent for this purpose. A magnetic compound fluid (MCF) was developed by compositing a magnetic field (MF) and a magnetorheological (MR) fluid. MCFs exhibited higher magnetic pressure and apparent viscosity than MFs and a better dispersity of nonmagnetic particles than MR fluids under a magnetic field, while maintaining a fluid-like behavior. The MCF slurry contains usually carbonyl-iron-particles (CIPs), water-based MF with nm-sized magnetite particles, abrasive particles, and α-cellulose. However, MCF slurry has not been used to polish aspheric surfaces, due to the complex material removal profile induced by the conventional polishing methods. By the inspiration of conventional MCF polishing tools, i.e., the mountain-shaped MCF tool and MCF wheel, a novel doughnut-shaped MCF tool was proposed for polishing aspheric surfaces. Under a rotary magnetic field which was generated by the revolution of the eccentrically located ring-shaped magnet, the magnetic lines of force constantly revolved around the MCF carrier, leading the clusters formed by CIPs to alert their orientations to stir abrasive particles. The renewing working area

prolonged the life of the MCF tool to a limited extent. In this study, polishing with the novel MCF polishing tool under the rotary magnetic field was extensively studied from the investigation on feasibility polishing, the fundamental properties of the MCF tool (including the formation process, the optimal geometry of the MCF tool, and behavior of CIPs and APs), the evolution and equivalent control law of surface roughness (including the indentation model for a single abrasive particle, polishing forces, and prediction model for surface roughness), and the investigation experimentally on the effect of parameters on removal of material/tool marks and surface quality. According to the results, the aspheric surface was polished successfully.

The fundamental properties of rheological behaviors of MCF slurry were studied, which demonstrated that the shear stress and viscosity were affected significantly by CIPs concentration and magnetic field strength. Thus, the polishing principle with the novel polishing tool was given out according to the properties of the MCF slurry, and the experimental setup was constructed. The results of the feasibility polishing experiments showed that the top tip of the MCF tool was located at a distance D to the revolution center of MCF tool and performed better ability on removing material. The D could be obtained by using $D = (d_i + d_o)/4$, i.e., the middle portion of the working area. Simultaneously, the location and gesture control laws for polishing were given out. Because the workpiece was polished to the nano-precision scale in the experiments, it was certain that this method was potential to polished materials.

The variation process of external MCF slurry, terminal shape and the formation time were investigated for obtaining the perfect MCF tool under various process parameters,

namely magnet eccentricity r_e, supplied MCF slurry amount V, MCF slurry carrier rotational speed n_c, and magnet revolution speed n_m. The internal structure of the MCF tool was observed, based on which the behavior of CIPs and APs were thereby confirmed through theoretical analysis and polishing experiments. The model of material removal was proposed. The results showed that a perfect MCF tool could be obtained when the eccentricity r_e, the rotation speed of the MCF carrier n_c, the revolution speed of the magnet n_m, and the amount of MCF slurry supplied V were proper. The CIPs were gathered to form the ferric clusters along the magnetic flux lines. The Aps, at a given working gap, can squeeze the work-surface. The squeezing action was much more intense when larger APs and the MCF slurry with a higher magnetization were employed. The material removal model suggested that the material was removed due to the APs and the relative motion between the work-surface and APs.

In order to study the evolution and equivalent control law of surface roughness, the motion analysis, and indentation model were established theoretically by explaining in detail the normal force and tangential force induced by the MCF tool. Simultaneously, numerical analysis for predicting the surface roughness under variable parameters was conducted. The prediction model on surface roughness was verified by a series of experiments. As a result, the relationship between parameters and surface roughness was obtained, thus, the surface roughness can be predicted by giving the proper parameters.

The investigation on polishing aspheric surfaces was conducted experimentally. The representative material removal profile on the generatrix, the process of removing tool marks, and typical surface roughness were investigated. The effects of parameters,

including working gap h, revolution speed of MCF carrier n_c, amount of MCF slurry supplied, CIPs concentration and APs size on polishing performance were conducted. With the optimized conditions, the aspheric surface was polished successfully. As a result, a V-shaped generatrix was obtained on the polished conic surface. A similar surface roughness at the circumference and different surface roughness on the generatrix were found. The tool marks composited of periodic peaks and valleys with relatively low frequencies were diminished gradually with the polishing time. A smaller working gap was proper for polishing. The 1 mm of working gap h was selected in the experiments. Higher revolution speed of MCF carrier n_c and larger amount of MCF slurry were applied, and then a larger material removal rate, larger polishing area, and better surface roughness were achieved. Better performance on the material/tool marks removal rate when a higher CIPs concentration was applied. However, the best surface quality was attained with the CIPs concentration of 45 wt.% in this study, rather than 55 or 35 wt.%. Larger APs were beneficial for obtaining higher material/tool marks removal rates. However, a better surface quality was achieved when the APs of 1 μm in diameter were preferred rather than 0.5 or 2 μm. The aspheric surface was polished successfully without the tool marks on the surface. Furthermore, the shape of the workpiece was kept in a favorable extent.

According to the above results, the magnetic field-assisted polishing using the novel MCF tool is a promising technique for the nano-precision finishing of aspheric surfaces.

Chapter I Introduction

1.1 Aspheric surfaces

The aspheric surfaces can replace the conventional spherical surfaces in the optical systems, due to their prominent performances in eliminating spherical aberration and also reducing other optical aberrations such as astigmatism. A single aspheric element can not only improve the imaging quality and save energies for a complex multi-optical system, but make the device much smaller and lighter, and sometimes cheaper [1]. For examples, aspheric elements are often used in the design of multi-element wide-angle and fast normal lenses to reduce aberrations; they are also employed in catadioptric systems and combined with other reflective elements, such as the aspherical Schmidt corrector plate in the Schmidt cameras, the Schmidt–Cassegrain telescopes, and ultra-high-power laser devices; Small molded aspheric elements can be applied to collimate diode lasers. The typical applications of the aspheric elements are shown in Fig. 1.1.

(a) Lenses (b) Reflection systems (c) Cameras (d) Telescopes

Fig. 1.1. Application of the aspheric elements.

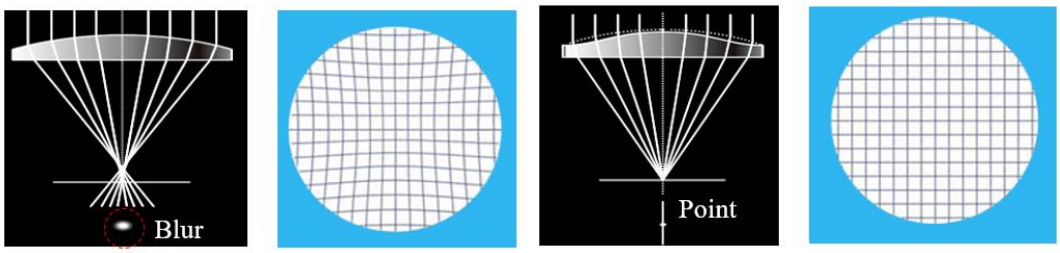

(a) Spherical imaging quality (b) Aspheric imaging quality

Fig. 1.2. Spherical/aspheric elements imaging quality.

The comparation of imaging quality between spherical/aspheric elements is shown in Fig. 1.2. It is obvious that the lights focus on a point when the aspheric element is used, rather than many points when the spherical element is used. Therefore, the resultant image is clearer with the aspheric element. This is because the slope at the aspheric surface is different along the generatrix, which is prone to focus the lights to a small area. The variations of the slopes are so important that a specific function is designed technically for convenient controlling the variation rules:

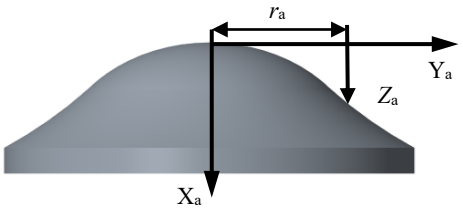

Fig. 1.3. Design of aspheric elements.

$$Z_a(r_a) = \frac{cr_a^2}{1+\sqrt{1-(1+k)c^2r_a^2}} + A_1r_a^4 + A_2r_a^6 + A_3r_a^8 \quad (1)$$

where Z_a is the depth of the curve, r_a is the distance from the center, c is curvature (c = 1/Radius), K is the conic constant, A_x is higher-order terms. Giving the values of these parameters into the prescribed equation, the generatrix of the aspheric surface can be determined, and therefore, the desired slope can be obtained [3-4].

Those optical instruments require materials with properties of low-weight, high-strength and stiffness, appropriate thermal conductivity, good manufacturability and low-cost. The conventional materials for aspheric optical elements can be roughly divided into metals (e.g. aluminum and aluminum alloy, copper), optical plastics (e.g. TPX, SAN), optical crystals (e.g. alkaline earth fluorides, laser crystals), IR materials (e.g. metallic germanium, silicon, gallium arsenide) and Glasses. However, the increasing demanding on performance, tolerances and capabilities have immensely prompted researchers to exploit new materials like CFC, SiC, CSiC and other specific materials. These materials are not only unaffordable but also unavailable or unreliable for all applications. Aluminum and aluminum alloys are eligible because of their heritage and the extensive knowledge of their properties, reliable and predictable behaviors, thus they are always essential for complex and accurate optical systems.

Optical processing technologies have been developed for around hundreds of years. Generating cutting methods are regarded as the earliest aspherical machining technologies [5]. Because these methods are extremely depended on the experience of workers, the form accuracy and surface quality are hard to be ensured. Therefore, these methods are great blindness so that they always waste plenty of time and cost larger, and are not satisfied for meeting the high precision demanding in modern optical industry. Ultra-precision single point diamond turning (SPDT) technology is proposed as one of the efficient methods for machining optical parts, which is dependent on the reliability of the machines and the high quality of the single-crystal diamond cutting tools [6]. It is suitable for processing infrared crystal materials and non-ferrous metal materials. Ultra-precision grinding mainly aims at

machining hard and brittle materials in their plastic domains [7-8]. Recognizing that the two technologies can process a wide range of aspheric surfaces and reduce the machining allowance efficiently with satisfying precision, they are essential pre-processing methods in the manufacture of aspheric surfaces. However, tool marks and sub-surface damage are unavoidable when materials are machined using the two methods, limiting the application of the two methods for high precision optical systems. To meet the strict requirements of aspheric elements, a polishing processing is applied to remove the defects induced by the pre-processing and enhance the surface quality.

To develop the proper polishing technology and improve the quality of the optical aspheric surfaces, especially to reduce the tool marks and sub-damage, W. J. Rupp and other stuffs first proposed a novel method for polishing aspheric surfaces based on computer-controlled optical surfacing (CCOS), which can process the surface using a small grinding head with the preset processing path, resident time, and polishing pressure. The introduction of the CNC machining technology greatly promotes the development of the aspheric surface processing technology. For example, a mirror with a diameter of 500 mm was successfully polished to a RMS of 0.04 μm and Ra of 5 nm in three months with the CCOS equipment provided by the American corporation Itek [9]. However, the material removal in CCOS is uneven in general because of the wear of the rigid polishing tool and low percentage of the contact area. The problem was solved by transforming rigid polishing to flexible polishing. One of the proposed flexible polishing methods is bonnet polishing, by which an axisymmetric aspheric element made of molten silicon was polished by Walker. The results showed that the PV was reduced from 2 to 0.19 μm and a Ra of 1.8 nm was

obtained after 120 min of polishing [10]. Another typical method is fluid jet polishing (FJP). Beaucamp et al. [11] proposed the FJP process for electroless nickel-plated die polishing, which decreased the PV from 387 to 47 nm and removed the turning marks. Although aspheric surfaces can be polished to a mirror surface, the disadvantages of these methods are still evident. Bonnet polishing was developed to offset the defects of CCOS, but an exact load device was still needed to control the polishing pressure. In FJP, the wear of the nozzle is inevitable due to the friction between the fluid and nozzle, leading to an unstable material removal rate. To solve these problems, a magnetic field-assisted polishing method was presented to smooth the aspheric surface. In this method, a magnetic fluid (MF) or magnetorheological fluid (MRF) slurry could form a controllable flexible polishing tool under a supplied magnetic field [12]. For instance, Tani et al. developed a polishing method by blending SiC particles into a MF to achieve a smaller surface roughness R_{max} than 0.04 μm on acrylic resin [13]. However, the polishing methods based on MFs are difficult to apply for polishing aspheric surfaces because of the low efficiency and controllability of the material removal rate due to its low magnetic pressure and apparent viscosity. Therefore, magnetorheological fluids (MRFs) have been proposed to polish aspheric surfaces by mixing micro-sized carbon iron particles into the base fluid. Jacobs improved an aspheric element composed of SLAM55 appreciably using a MRF slurry, and the final form error was reduced from 3.7 to 0.2 μm [14]. Hence, the magnetic field-assisted polishing processes are regarded as the proper polishing method for the reduction of tool marks and sub-damage. The magnetic field-assisted polishing processes will be introduced in detailed in the following.

1.2 Review of the magnetic field-assisted polishing processes

Magnetic field-assisted polishing is a promising surface finishing technique, in which a magnetic fluid (MF), magnetorheological fluid (MRF), or magnetic compound fluid (MCF) slurry is employed to form the flexible polishing tool. Once a magnetic field is applied, flexible chain-shaped magnetic clusters are instantly formed within the polishing tool along the magnetic lines of force, the non-magnetic particles are enforced to move to the surface of the polishing tool, and the dimensions and orientations of these ferric clusters can be changed according to the shape of the work-surface. The magnetic field-assisted polishing is first proposed by the Russian researchers, they set up an apparatus to polish workpiece with the MF slurry, the surface was polished successfully but the efficiency was not satisfied. In order to improve the polishing ability, the MRF slurry and MRF-based slurry are invented. A diamond-turned polymethylmethacrylate (PMMA) part was polished successfully to a root mean squared (RMS) surface roughness 0.5 nm using magnetorheological finishing (MRF) [15]. A ball end process using MRF slurry was proposed for finishing three-dimensional surfaces [16]. A mirror freeform surface of a prosthetic knee joint implant constructed with a titanium alloy was obtained by a magnetorheological fluid-based finishing (MRFF) process [17]. The surface quality of an aspheric element composed of SLAM55 was improved appreciably using a MRF slurry, and the form error was reduced from 3.7 to 0.2 μm [18]. These studies demonstrated that polishing with MRF has the potential for polishing a variety of surfaces due to its flexibility, controllability, and efficient control over the abrading forces acting on the workpiece. However, under a given magnetic field, the low particle dispersity in a MRF slurry leads to

a difficulty in stabilizing their performances in surface finishing.

To overcome the disadvantages of MRF slurries, Shimada et al. [19] developed a magnetic compound fluid (MCF) slurry, which can be obtained generally by blending micro-sized carbonyl-iron-particles (CIPs), abrasive particles (APs), and α-cellulose into a magnetic fluid (MF) containing nano-sized magnetite particles (MPs). Due to the advantages of MFs, the dispersibility of the APs in the new slurry is better than in MRF slurry, resulting in better polishing performance. Shimada consequently proposed a new contact-free surface finishing method for polishing workpieces with micro 3D structures using the MCF slurry [20], and thereby, mirror surface finishing of a brass specimen with rib-shaped grooves was performed successfully. According to the reports of Shimada, Needle-like magnetic clusters were observed within MCF slurry [21], smaller clearance improved the polishing results and shortened the polishing time, and magnetic field strength determined the distributions of the abrasives [22]. In addition, shear force in the contact-free finishing process was strengthened when α-cellulose was mixed into the MCF slurry and the material removal depended on the shear stress along the rotation direction of the polishing tool rather than the normal stress (nearly zero during polishing). Based on the works of Shimada et al., Furuya et al. [23] and Wu et al. [24] experimentally investigated the fundamental characteristics of contact-free MCF polishing at the flat surfaces constructed by stainless steel and acrylic resin and optimized the polishing conditions. Jiao et al. [25] employed a MCF wheel for ultra-fine finishing and investigated the performance of the wheel by polishing the fused silica glass. To further enhance the performance of Shimada's method, Wu and Sato [26] investigated the fundamental performance in the flat

and three-dimensional surface finishing of metal workpieces with a mount-shaped MCF polishing tool. With the proposed method, Guo [27] and Wang [28] improved the surface qualities of flat surfaces and micro-scaled V-grooves, respectively. Nano-scale precision could be obtained at a series of materials and surfaces with different shapes, meaning that MCF slurry is prominent in polishing.

1.3 Magnetic compound fluid (MCF) polishing tools

According to the reports mentioned above, the MCF polishing tools can be divided into two types, the detailed description of the polishing tools are as follows:

One of the conventional MCF polishing tools, which was proposed by Wu and Sato, shaped like a mountain under the rotary magnetic field that was generated by revolting a disk-shaped magnet with an eccentric distance. Guo systematically studied the properties of the mountain-shaped polishing tool, including the formation process, tool appearance, and internal structure. It is figured out that as a certain volume of MCF slurry is put onto the inferior surface of the MCF carrier, chain-shaped magnetic clusters composed of nm-sized magnetic particles and nm-sized CIPs are formed along the magnetic lines of force immediately. Dimensions of the clusters depend on the compositions of MCF slurry and the strength/applying method of the magnetic field. Within the MCF slurry, non-magnetic abrasive particles are entrapped into the clusters or distributed between clusters, and most of them are encouraged to be close to the top of the clusters due to gravity and magnetic levitation force. In addition, α-cellulose fibers interwoven with the clusters to increase the viscosity of MCF slurry. The other polishing tool is the MCF wheel, which was proposed by Jiao [29]. With a ring-shaped magnet which is magnetized along the axis direction, the

MCF wheel is formed by attaching the MCF slurry to the side face of the magnet when the magnet is rotated. The material removal profile and internal structure of the MCF wheel were studied by Jiao. It was figured out that the most material was removed near the two boundaries rather than the middle portion. Clusters formed along the magnetic line of force, abrasive particles attached to the clusters, and α-cellulose fibers linked clusters together. This proposed MCF wheel could be used for polishing flat workpieces with a series of materials including optical glasses, ceramics, and metals.

Although the two MCF tools exhibited high polishing performances regardless of the work-material, the conventional mountain-shaped MCF polishing tool and MCF wheel are not suitable for polishing aspheric surfaces due to the complex material removal profile on the work-surface. To simplify the material removal profile, Guo intended to invent a doughnut-shaped polishing tool by rotating a disk-shaped magnet with an adjustable eccentricity. However, strict conditions, such as a large eccentric ratio and a precise amount of required of MCF slurry, were necessary to form the satisfactory polishing tool.

Although the magnetic field over the magnet surface reduces more rapidly as the distance increases, comparing the ring-shaped magnet with the disk-shaped magnet, the gradient of the magnetic field is larger than that of the disk-shaped magnet, as shown in Fig. 1.4, which means that the polishing forces have no obvious different. In order to invent an effective method for polishing aspheric surfaces conveniently, a novel doughnut-shaped polishing tool was proposed in this work by using the ring-shaped magnet. The specific description of the novel polishing tool and its properties were going to be given out in the rest works.

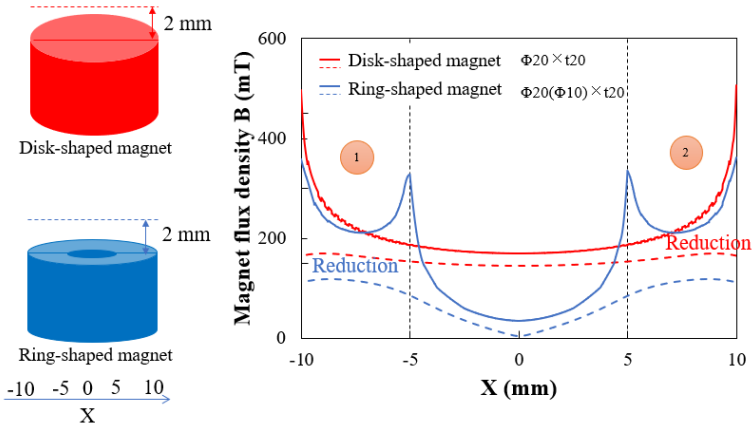

Fig. 1.4. Distribution of the magnetic field over the upper surface of the magnets.

1.4 Overview of the thesis

The objectives of this thesis research work are to clarify the properties of the novel MCF polishing tool for polishing aspheric surfaces. The works concerned about the MCF tool itself, including the fundamental investigations on the formation process, geometry, and polishing ability, and so on. For the purpose, the detailed researches were divided into several chapters as follows:

Chapter I first briefly introduced the aspheric surfaces, including the crucial roles in optical fields, the material for the products and the manufacturing methods, to clarify the objectives and meaning of this research. The magnetic field-assisted polishing processes were reviewed from aspects of different polishing methods, polishing of workpieces with different structures constructed by different materials, and their polishing effects. A series of popular techniques were outlined for demonstrating the excellent performance of magnetic field-assisted polishing processes on polishing. Then, the development of MCF polishing tools was reviewed, including the characteristics of the mountain-shaped polishing tool and MCF wheel.

Chapter II first depicted metrology and characterization in the whole experiments. Then

the fundamental properties of rheological behaviors of MCF slurry were studied. After that, the processing principle was thereby proposed and the experimental apparatus was constructed. At last, the feasibility of polishing was conducted.

Chapter III first investigates the variation process of external MCF slurry, terminal shape and the formation time under a rotary magnetic field with various process parameters, namely magnet eccentricity r_e, supplied MCF slurry amount V, MCF slurry carrier rotational speed n_c, and magnet revolution speed n_m. Then, the internal structure of the MCF tool was observed, based on which the behavior of CIPs and APs were thereby confirmed through theoretical analysis and polishing experiments. Finally, the model of material removal was proposed.

Chapter IV reports the evolution and equivalent control law of surface roughness. The kinematic analysis and indentation model were studied theoretically by explaining in detail the normal force and tangential force induced by the MCF tool. Simultaneously, numerical analysis for predicting the surface roughness under variable parameters were conducted. After then, the prediction model on surface roughness was established and verified. Finally, the relationship between parameters and surface roughness was established, thus, the surface roughness can be predicted in advance by giving the proper parameters for roughly pointing out the basic rules of the novel method.

Chapter V focuses on the experimental investigation on aspheric surface polishing for researching the method in detail. The representative material removal profile on the generatrix, the process of removing tool marks, and typical surface roughness were investigated. The effects of parameters, including working gap h, revolution speed of MCF

carrier n_c, amount of MCF slurry supplied, CIPs concentration and APs size on polishing performance were conducted. With the optimized conditions, the aspheric surface was polished successfully.

Chapter VI represents the summaries of this work and gives suggestions for future work on the novel polishing method.

References

[1] Arezki Y, Zhang X, Mehdi-Souzani C, Anwer N, Nouira H. Investigation of minimum zone assessment methods for aspheric shapes. Precis Eng. 2018;52:300-307.

[2] Chen F, Yin S, Huang H, Ohmori H. Fabrication of small aspheric moulds using single point inclined axis grinding. Precis Eng. 2015;39:107-115.

[3] Liu Y-T, Zhang L. An investigation into the aspheric ultraprecision machining using the response surface methodology. Precis Eng. 2016;44:203-210.

[4] Murakami S, Yanagida Y, Hatsuzawa T. Aspherical Lens Design Using Computational Lithography. Precis Eng. 2017;50:372-381.

[5] Meyer PA, Veldhuis SC, Elbestawi MA. Predicting the effect of vibration on ultraprecision machining surface finish as described by surface finish lobes. Int J Mach Tool Manu. 2009;49:1165-1174.

[6] Li M, Lyu B, Yuan J, Dong C, Dai W. Shear-thickening polishing method. Int J Mach Tool Manu. 2015;94:88-99.

[7] Wang H, Lin W. Removal model of rotation & revolution type polishing method. Precis Eng. 2017;50:515-521.

[8] Li M, Lyu B, Yuan J, Yao W, Zhou F, Zhong M. Evolution and equivalent control law of surface roughness in shear-thickening polishing. Int J Mach Tool Manu. 2016;108:113-126.

[9] Zheng W, Cao T, Zhang X. Applications of a novel general removal function model in the CCOS. Proc Spie. 2000;4231:51-58.

[10] Jones RA. Computer-controlled optical surfacing with orbital tool motion. Opt Eng. 1985;25:785-790.

[11] Walker DD, Beaucamp ATH. New results extending the Precessions process to smoothing ground aspheres and producing freeform parts. Opt Manu. 2005;5869:79-87.

[12] Beaucamp A, Namba Y, Freeman R. Dynamic multiphase modeling and optimization of fluid jet polishing process. CIRP Annals. 2012;61:315-318.

[13] Peng W, Li S, Guan C, Li Y, Hu X. Ultra-precision optical surface fabricated by hydrodynamic effect polishing combined with magnetorheological finishing. Optik. 2018;156:374-383.

[14] Tani Y, Kawata K, Nakayama K. Development of High-Efficient Fine Finishing Process Using Magnetic Fluid. CIRP Annals. 1984;33:217-220.

[15] Jacobs SD. Magnetorheological finishing: a deterministic process for optics manufacturing. Optic. 1995;2976:18-23.

[16] Shimada K, Akagami Y, Kamiyama S, Fujita T, Miyazaki T, Shibayama A. New Microscopic Polishing with Magnetic Compound Fluid (MCF). J Intel Mat Syst Str. 2002;13:405-408.

[17] Guo H, Wu Y, Lu D, Fujimoto M, Nomura M. Effects of pressure and shear stress on material removal rate in ultra-fine polishing of optical glass with magnetic compound fluid slurry. J Mater Process Tech. 2014;214:2759-2769.

[18] Wang Y, Wu Y, Nomura M. Fundamental investigation on nano-precision surface finishing of electroless Ni–P-plated STAVAX steel using magnetic compound fluid slurry. Precis Eng. 2017;48:32-44.

[19] Wang Y, Wu Y, Nomura M. Feasibility study on surface finishing of miniature V-grooves with magnetic compound fluid slurry. Precis Eng. 2016;45:67-78.

[20] Guo H, Wu Y. Ultrafine polishing of optical polymer with zirconia-coated carbonyl-iron-particle-based magnetic compound fluid slurry. Int J Adv Manuf Tech. 2015;85:253-261.

[21] Feng M, Wu YB. Fundamental Investigation on the Polishing Aspheric Elements with Doughnut-Shaped MCF Slurry. Key Eng Mater. 2018;792:179-184.

[22] Wu S-T, Chen J-Y, Wu S-H. A Rotary Encoder With an Eccentrically Mounted Ring Magnet. IEEE Transactions on Instrumentation and Measurement. 2014;63:1907-1915.

[23] Jiao L, Wu Y, Wang X, Guo H, Liang Z. Fundamental performance of Magnetic Compound Fluid (MCF) wheel in ultra-fine surface finishing of optical glass. Int J Mach Tool Manu. 2013;75:109-118.

[24] You LW, Yong BW, Nomura M. Nano-Precision Polishing of Oxygen-Free Copper Using MCF (Magnetic Compound Fluid) Slurry. Adv Mater Res. 2016;1136:455-460.

[25] Shimada K, Wu Y, Wong YC. Effect of magnetic cluster and magnetic field on polishing using magnetic compound fluid (MCF). J Magn Magn Mater. 2003;262:242-247.

[26] Shimada, K, Fujita, T, Oka, H, Akagami, Y, Kamiyama, S. Hydrodynamic and magnetized characteristics of MCF (magnetic compound fluid). Trans. Jpn. Soc. Mech. Eng. 2001;67: 3034–3040.

[27] Ahmad A. Handbook of optomechanical engineering1997.

[28] Peverini L, Kozhevnikov IV, Rommeveaux A, Vaerenbergh PV, Claustre L, Guillet S, et al. Ion beam profiling of aspherical X-ray mirrors. Nucl Instrum Methods Phys Res Sect A. 2010;616:115-118.

[29] Horst RT, Tromp N. Directly polished lightweight aluminum mirror. Adv Optic. 2008;7018: 08-18.

Chapter II MCF Slurry and Polishing Principle

2.1 Metrology and characterization

2.1.1 MCF slurry kinematic analysis

As displayed in Fig. 2.1, a high-speed motion analysis microscope (VW6000 by Keyence Co., Ltd.) was employed to observe the formation process and behaviors of the novel doughnut-shaped MCF polishing tool under a rotary magnetic field generated by the revolution of the ring-shaped magnet.

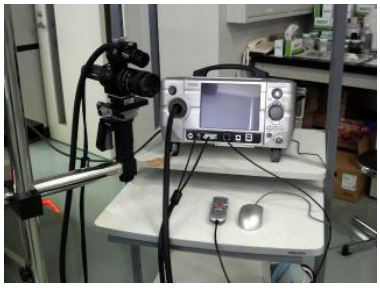

Fig. 2.1. Keyence VW6000 high-speed motion analysis microscope.

2.1.2 Surface profile

As shown in Fig. 2.2, a stylus-based profilometer (PGI Freeform by Taylor Hobson Inc.) was used to measure the cross-sectional profiles (at least three profiles) of a work-surface.

Fig. 2.2. Taylor Hobson PGI Freeform profilometer.

2.1.3 Surface quality characterization

As displayed in Fig. 2.3, scanning electron microscope (SEM, ERA-8900 by Elionix) was used to observe the internal structure of the MCF polishing tool. Elemental composition analyses were carried out using Energy Dispersive X-Ray Analysis (EDX, Genesis APEX by EDX) to observe the distribution of elements, such as Fe and Al.

Fig. 2.3. EDAX ERA-8900, 3D-SEM & EDX.

As shown in Fig. 2.4, the surface roughness was measured (at least five locations) using a non-contacting white-light interferometer which was equipped with a 10×, 50× Mirau interference objectives and provided measurement areas ranging from 350 μm×263 μm to 700 μm×526 μm (Newview 600, Zygo Corporation).

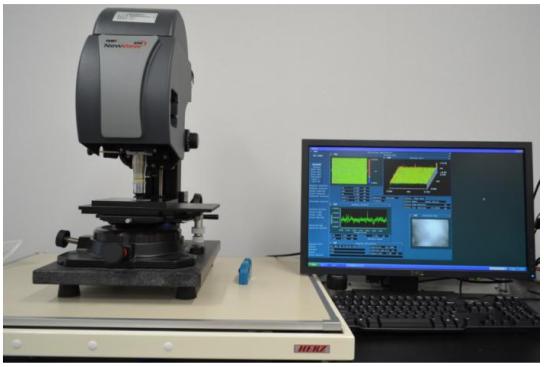

Fig. 2.4. Zygo New view 600 interferometer.

2.1.4 Force measurement

A force measurement system composed of a 3-component dynamometer (9256A1 by

Kistler Co., Ltd.), a charge amplifier and an oscilloscope was used to record the polishing forces. The sensitivities of the dynamometer, the charge amplifier, and the oscilloscope are (−10 pC/N (Fx, Fy) and −13 pC/N (Fz)), (0.01–9990 pC/M.U.) (2 mV/div–10 V/div), respectively.

2.1.5 Setups for mixing MCF slurry

Fig. 2.5. Ultrasonic mixer (Handy Sonic UR-20P, TOMY).

Based on the previous experiences, MCF slurry with a good dispersity of its components is crucial for the polishing performance. In order to obtain the well-blended MCF slurry, the following two devices are inevitable. The ultrasonic mixer with a 0.25 cm diameter active surface area enables the simple and efficient ultrasonic treatment to the small volume of MCF slurry. Agglomerated particles within the MCF slurry can be scattered easily under the frequency which can reach 28 KHz maximumly. The ultrasonic transformer is constructed by Titanium alloy so that it is reliable during mixing the MCF slurry. The iron particles, abrasive particles, and magnetic fluid were weighed by a high accuracy scale first and then mixed using this mixer. The particles within the slurry were mixed until they were well-blended.

Fig. 2.6. Planetary Centrifugal Mixer (AR-100, THINKY).

Then, a planetary centrifugal mixer, as shown in Fig. 2.6, was used for further mixing MCF slurry. The planetary centrifugal mixer with the dimensions of the height 328 mm, width 250 mm, diameter 250 mm was used to improve the quality of mixing the MCF slurry. The compact and suitable-anywhere design has enabled itself to be selected at many universities and research institutes where a large number of equipment, devices, and facilities limit their space. This setup is suitable for initial consideration in research and development where small amounts of materials are repeatedly tested. The mixer has the Memory function for the simple pre-setting of mixing conditions.

After treated by these steps, the satisfying MCF slurry could be attained.

2.2 MCF slurry

2.2.1 Preparation of MCF slurry

As exhibited in Fig. 2.7, components of MCF slurry used in this work are as follows: carbonyl-iron-particle (CIP, mean particle size 5 μm, BASF made), alumina (Al_2O_3) abrasive particles (mean size 1 μm, alpha, AP-D, deagglomerated aluminas, Struers Inc.), water-based magnetic fluid (MF, MSGW11 by Ferrite Corporation) containing nano-sized Fe_3O_4 and α-cellulose (Reagent, Nacalai Tesuque Inc.). The oil-based magnetic fluid MF will not be employed in this work because the water-based MF is more clean and friendly

to environment than oil-based MF.

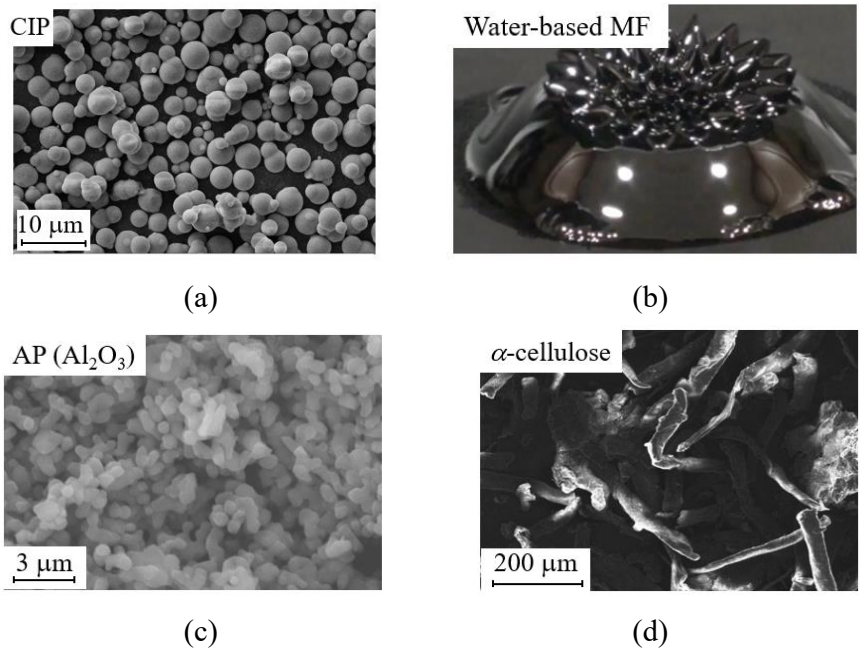

Fig. 2.7. SEM images of (a) the conventional CIP, (b) water-based MF, (c) Al_2O_3 abrasive particle, (d) α-cellulose.

2.2.2 Rheological behaviors of MCF slurry

Shimada et al. [1] developed the magnetic compound fluid (MCF) by mixing a magnetic (MF) and a magnetorheological fluid (MRF) with the same base solvent. Hence, MCF includes not only μm -sized iron particles but also nm-sized magnetite particles whereas there are no μm-sized magnetite particles within MRF. They confirmed that MCFs exhibit higher magnetic pressure and apparent viscosity than MFs and a more stable distribution of particles than MR fluids under a magnetic field while maintaining a fluid-like behavior.

In order to understand the fundamental characteristics of the MCF slurry under a magnetic field, i.e., the rheological behaviors of MCF slurry, the experimental investigations were conducted. The rotational rheometer (MCR-302, Anton Paar Corporation) was used for observing the variations of shear stress or viscosity with varied

magnetic fields or shear rates. Moreover, the relationship between the magnetization *M* of the MCF slurry and the magnetic flux density *B*, i.e., the *M-B* curve was measured by the physical property measurement system (PPMS-14LH).

The experiments were performed by employing different MCF slurries, i.e., MCF1-MCF3, with different components containing various concentrations of CIPs, as shown in Table 2.1. When testing the shear stress and viscosity, the volume of supplied MCF slurry was kept in 1.5 ml in each test and the testing distance was limited to 1 mm.

Table 2.1.

Different MCF slurries

	CIPs (wt.%) with diameter ~ 5μm	MF (wt.%)	APs (wt.%)	α-cellulose (wt.%)
MCF 1	55	30		
MCF 2	45	40	12 (1 μm)	3
MCF 3	35	50		

As illustrated in Fig. 2.8, the representative variations of shear stress τ with shear rate $\dot{r}$ are investigated under varied magnetic field by using MCF 2 slurry. Regardless of the magnetic field, the shear stress τ increased rapidly when the shear rate increased from 0 to 100 1/s, then it decreased slightly until shear rate increased to 300 1/s, after which, the shear rate τ started to increase with a very small increasing rate when shear rate increased continually. Thus, marks I, II, and III were made for distinguishing these typical statuses. Apparently, the induced shear stress τ was larger under higher magnetic field strength, 58 KPa of maximum shear stress τ was obtained when magnetic flux density *B* of 0.8 T and shear rate of 100 1/s were applied.

Additionally, the variations of viscosity η with shear rate are shown in Fig. 2.9. Regardless of the magnetic field, the viscosity sharply decreased when shear rate increase from 0 to 100 1/s, then the decrease rate descended slowly and kept stable gradually as the increase in the shear rate. It was demonstrated that the slurry performed like a solid at the beginning, when shear rate τ increased, the status was altered from solid-like to liquid, meaning that the slurry started to flow, and the flowability was enhanced sharply due to the increase in shear rate and kept a negligible increasing when shear rate was over 100 1/s.

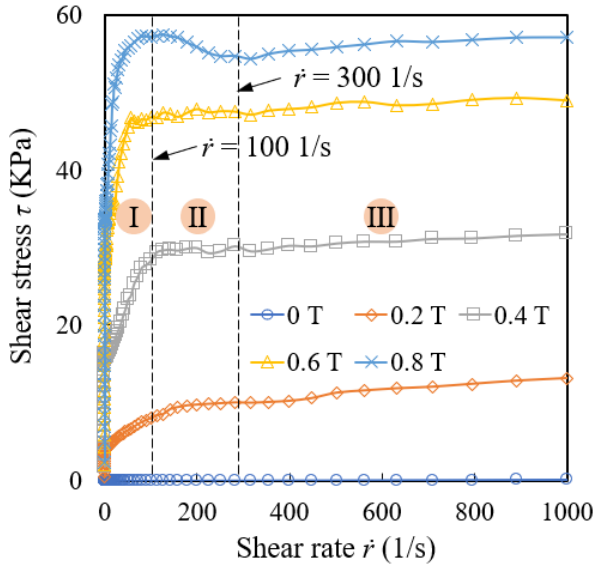

Fig. 2.8. Representative variations of shear stress with shear rate.

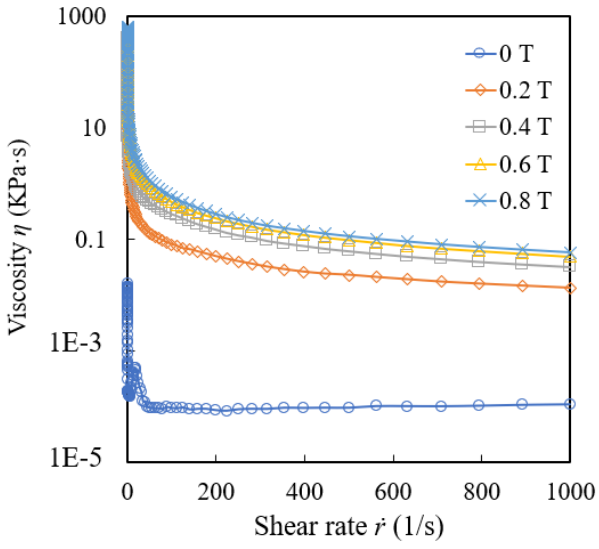

Fig. 2.9. Representative variations of viscosity with shear rate.

According to Figs. 2.8 and 2.9, the shear stress and viscosity were affected deeply by the magnetic field and shear rate, therefore, shear stress τ and viscosity η can be expressed by $\tau = f_1(B, \dot{r})$ and $\eta = f_2(B, \dot{r})$, respectively. Based on the data list in Figs. 2.8 and 2.9, the fitted expressions can be obtained with MATLAB as follows:

$$\tau = 49.28 + 52.14B + 0.001121\dot{r} - 53.11\dot{r}^{-0.0402} \quad \text{(R-squared = 0.87)} \qquad (2\text{-}1)$$

$$\eta = -12.4 + 137.7B\dot{r}^{-0.4175} \quad \text{(R-squared = 0.89)} \qquad (2\text{-}2)$$

With the Eqs. (2-1) and (2-2), the fundamental rheological behaviors of MCF slurry can be depicted precisely. In other words, the MCF slurry can be governed by giving proper magnetic field strength and shear rate.

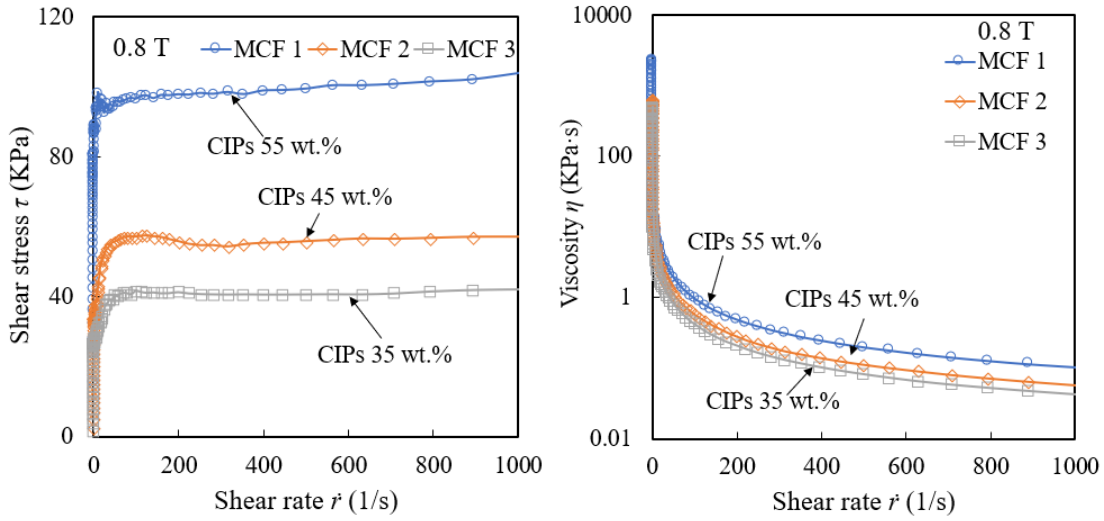

(a) (b)

Fig. 2.10. Representative variations of shear stress and viscosity with shear rate.

The variations of shear stress and viscosity with the shear rate with different MCF slurries are displayed in Fig. 2.10. It was found in Fig. 2.10(a) that higher CIPs concentration enabled higher shear stress of the formed polishing tool, implying that the polishing forces were greater by using higher CIPs concentration. As shown in Fig. 2.10(a),

the initial viscosity was higher when higher CIPs concentration was used, demonstrating that the tool was more solid and harder to flow swimmingly until enough external energies were applied.

In order to discover the reasonable explanations about the impacts of higher CIPs concentration on the fundamental characteristics of the polishing tool, the variations of the magnetization *M* of the MCF slurry and the magnetic flux density *B*, i.e., the *M*-*B* curve was given out, as shown in Fig. 2.11. With the increase of magnetic flux density *B*, the magnetization *M* of the MCF slurry was rapidly increased before 0.6 T, after then, *M* kept almost stable, meaning that the slurry reached a magnetic saturation state in which the formed tool was strongest to resist external engine. As the CIPs concentration increased, the corresponding *M* gradually increased under the applied magnetic field. Consequently, CIPs attracted each other tightly so that the formed ferric clusters were much stronger to prevent from being fractured during polishing [2], increasing the shear stress and solidity.

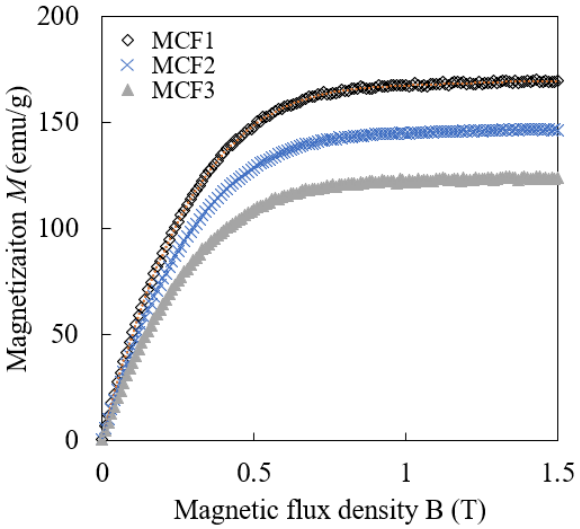

Fig. 2.11 The variations of the magnetization M of the MCF slurry and the magnetic flux density *B*, i.e., the *M*-*B* curves.

According to the investigation on the rheological behaviors of MCF slurry, it was

summarized that the polishing tool with above MCF slurry is potential to remove material and smooth aspheric surfaces under proper conditions. Consequently, the polishing principle for polishing aspheric surfaces is proposed in the following.

2.3 Polishing principle

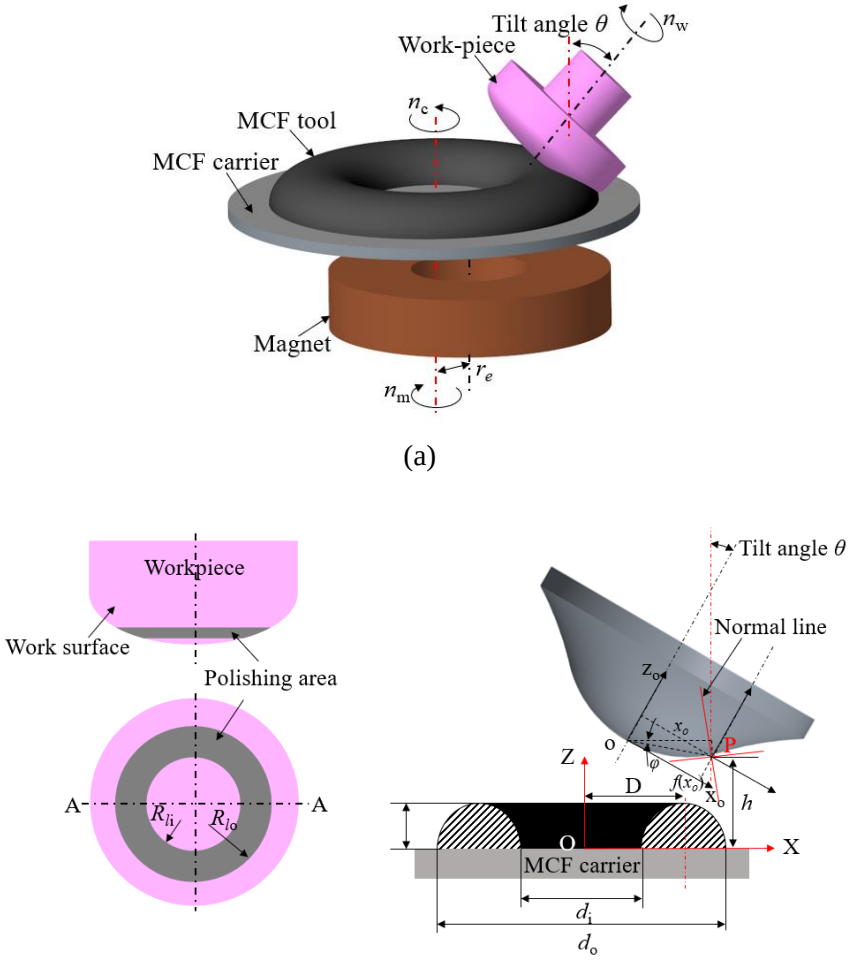

Fig. 2.12. Illustration of processing principle. Schematic drawings of (a) the proposed method, (b) the polishing area, and (c) the position of the workpiece relative to the polishing tool.

Figure 2.12(a) shows a schematic drawing of the aspheric surface polishing process with a doughnut-shaped MCF polishing tool (hereafter called the MCF tool for simplicity). For the simple formation of a MCF tool, a ring-shaped permanent magnet is employed, located below a disc-shaped non-magnetic MCF carrier with a small clearance. Once the magnet

revolves around the axis of the MCF carrier at a revolution speed n_m, with an adjustable eccentricity r_e a rotary magnetic field is generated. If a specified amount of MCF slurry V is supplied onto the upper surface of the MCF carrier, the MCF tool will form under the rotary magnetic field. When the workpiece contacts a portion of the MCF tool, which is hereafter called the working area, the working area of the MCF tool transforms its appearance based on the shape of work surface. Due to the rotation of the MCF tool, the working area is constantly renewed in one revolution, and thus, the working life of the MCF tool can be prolonged to a limited extent. As shown in Fig. 2.12(b), an annular polishing area with an inner radius R_{li} and outer radius R_{lo} is obtained after polishing using the MCF tool. Furthermore, once the different parts of the workpiece are polished sequentially by the MCF tool, the whole surface of the workpiece will eventually be polished by these overlapping annular polishing areas.

A detailed description of the polishing process is given in Fig. 2.12(c). A coordinate system XOZ is established, in which the origin is fixed at the center of the upper surface of the MCF carrier, the Z-axis overlaps with the rotation axis, and the X-axis is parallel to the upper surface of the MCF carrier. Considering the axially symmetric character of the MCF tool and aspheric workpiece, the relative position between the MCF tool and workpiece is discussed only in the cross-section in the XZ plane. The dimensions of the MCF tool, including the radius of the inner ring d_i and the outer ring d_o, the height H, and the cross-section profile, depend on the V and r_e. The cross-section profile of the MCF tool is similar to a semi-ellipse, the top tip of which is located a distance of D from the rotation axis of

the MCF carrier. Point P is intended to be polished with a proper gesture by the portion of the MCF tool where performs best on material removal capacity.

2.4 Experimental apparatus

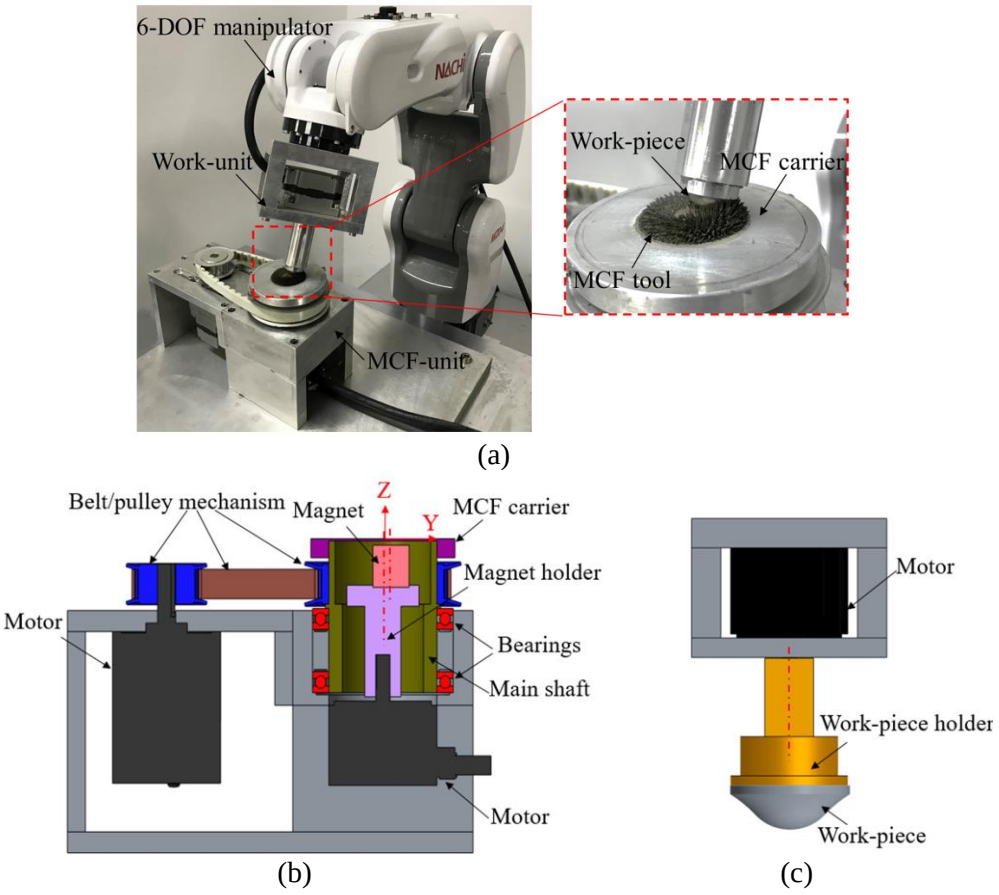

Fig. 2.13. Experimental setup: (a) schematic of the constructed rig, (b) the structures of the MCF unit, and (c) the work-unit.

To realize the processing principle in practice, an experimental setup was constructed based on a commercial 6-DOF manipulator, as shown in Fig. 2.13(a). A MCF unit (Fig. 2(b)) composed of a magnet holder, a ring-shaped permanent magnet (ND35, 30-mm outer diameter, 9-mm inner diameter, 20-mm thickness, 0.5 Tesla), and the MCF carrier (thin aluminum disc) were mounted onto a work-bench. The magnet was attached to the upper end of the magnet holder. The MCF carrier was rotationally driven by a motor via a belt/pulley mechanism, and the revolution motion of a magnet was obtained by

directly rotating its holder with another motor. A work-unit (Fig. 2.13(c)) was fixed onto the end tip of the 6-DOF manipulator to hold and rotate the workpiece. The control system of the 6-DOF manipulator was adequate for realizing the motions mentioned above.

The dimensions of the ring-shaped magnet, i.e., the 30 mm outer diameter, the 9 mm inner diameter and the 20 mm thickness, were determined in order to obtain a doughnut-shaped MCF tool with appropriate dimensions which is suitable for the precision and effective polishing of a convex aspheric work surface used in this work that will be detailed in the rest of Chapters.

2.5 Feasibility investigation on polishing

2.5.1 Experimental details

In this section, the polishing investigation was studied experimentally for examining the feasibility of material removal and surface smoothing by the proposed method. Further, the setup was modified for this purpose, as shown in Fig. 2.14. The dynamometer was mounted at the bottom of the MCF unit and simultaneously fixed into the work-bench. Flat workpieces (□50 mm, thickness 10 mm) were employed in this experiment, which can be considered as an aspheric element with infinite curve radius. The dynamometer started to work before the polishing tool contacting with the work surface and continued working within 60 seconds. The material is removed absolutely because forces are generated in the polished area. F_n and F_t are shortened forms of the normal force and the tangential force, respectively. During gradual loading, higher values F_z was observed due to compression of those ferric clusters. Once reaching the predetermined gap, all three forces came to their own states. The equations for calculating the two forces were represented by Eqs. (2-3) and

(2-4) based on the schematic graph shown in Fig. 2.15. F_z, F_y, F_x were measured synchronously during polishing.

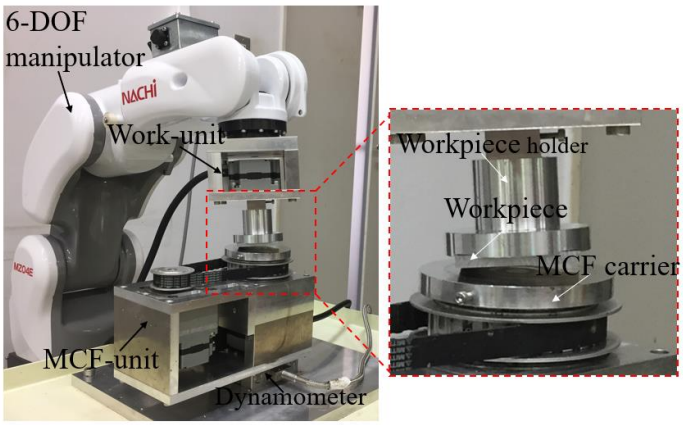

Fig. 2.14 Modified setup.

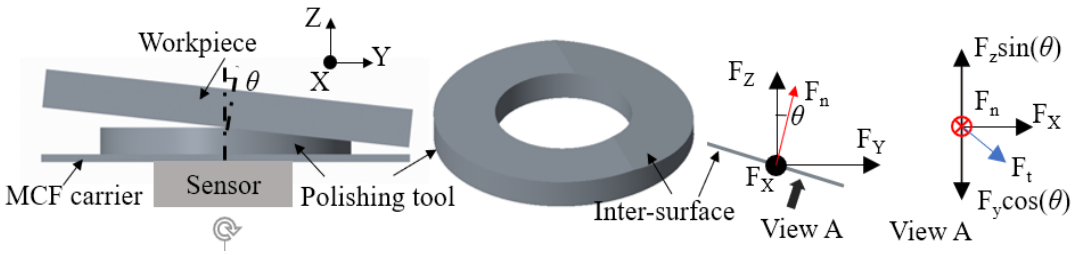

Fig. 2.15. Schematic graph for calculating normal force and tangential force.

$$F_n = F_z \cos\theta + F_y \cos\theta \tag{2-3}$$

$$F_t = \sqrt{(F_z \sin\theta - F_y \cos\theta)^2 + F_x^2} \tag{2-4}$$

2.5.2 Results and discussion

Fig. 2.16 showed the values of F_z, F_y, F_x, under the condition of working gap h = 3.5 mm, D = 0 mm (the center of upper surface of the workpiece was considered as point P), tilt angle $\theta = 6^{\circ}$, the volume of suppled MCF 2 slurry = 2.5 ml, r_e = 4 mm, n_c = 300 rpm, n_m = 500 rpm, and n_w = 1000 rpm. It is obvious that F_n behaves much higher when the MCF tool was compressed gradually by the workpiece, which is caused by the squeezing of those ferric clusters before the workpiece arrives predetermined location, then it went down and

kept variable in a small scale. At the end of the measurement, it raised higher again because of the recovery of the highly squeezed ferric clusters then decreasing to its initial state. It is also easy to see that the F_n was affected most by the F_z due to their consistent tendency during polishing. As to tangential force F_t, it grew stably no matter when the MCF tool was compressed gradually to its stable state or started to recover to its initial state. This indicates that there is no transformation of the ferric clusters caused by compression in the direction of the tangential force F_t. With the results, the mean value of those forces can be obtained. In this work, the normal force F_n and tangential force F_t is almost 1.4 N and 1.09 N during polishing, respectively.

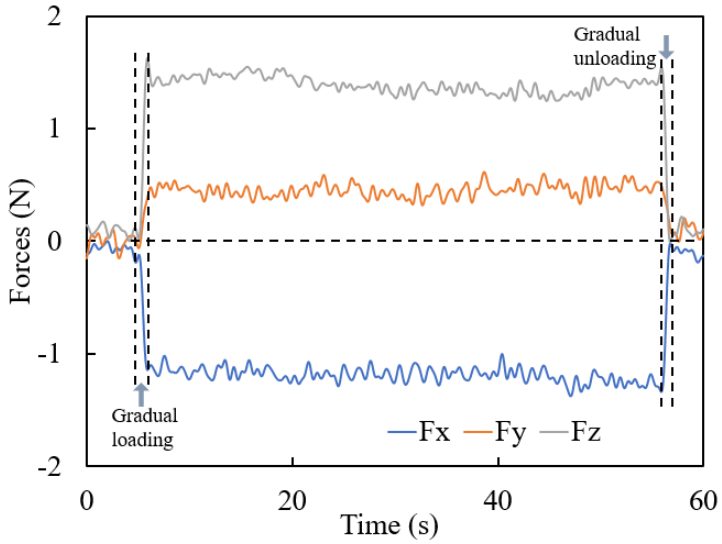

(a)

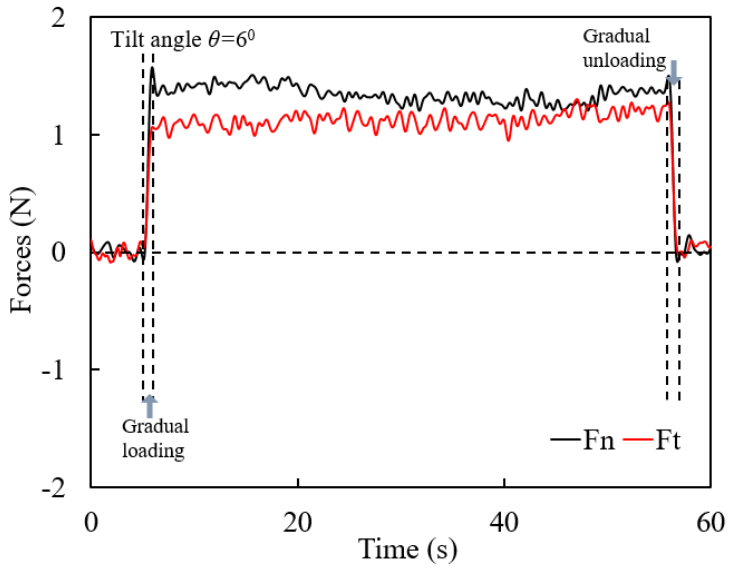

(b)

Fig. 2.16. Variation of forces during polishing: (a) the obtained F_z, F_y, F_x, (b) normal and tangential forces (F_n and F_t).

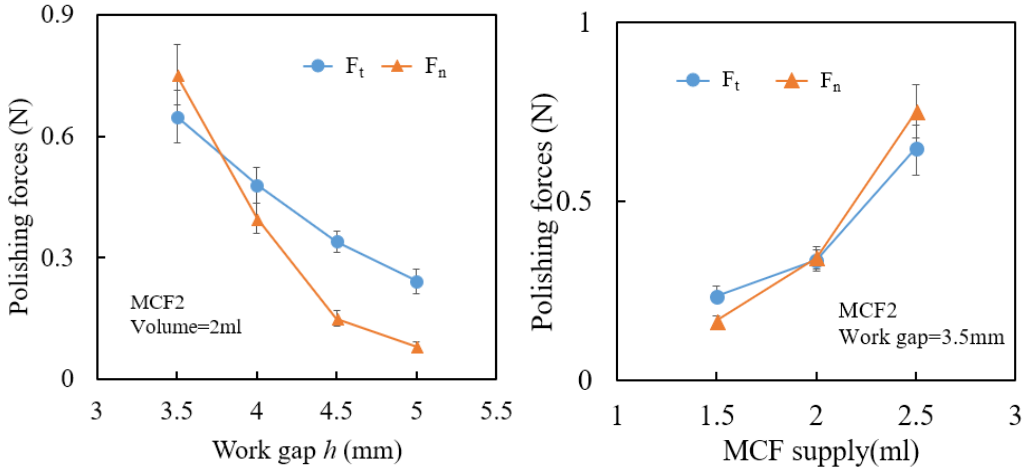

(a) (b)

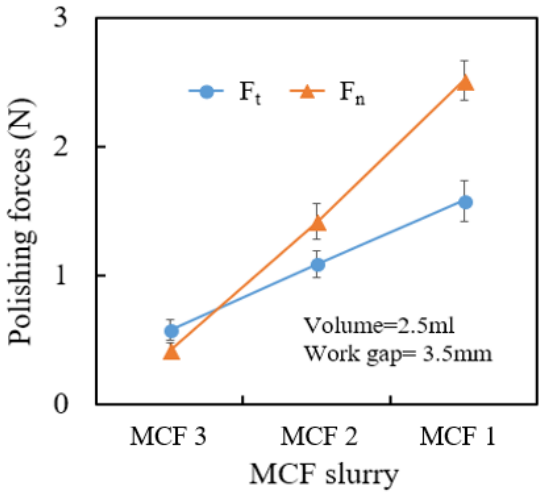

(c)

Fig. 2.17 Variations of forces with working gap *h*, the volume of MCF slurry supplied, and different MCF slurry.

Figs. 2.17(a), (b), and (c) give out the variations of polishing forces with different parameters during polishing. The discussions were carried out as followings:

The portion of the polishing tool which passed through the interface between the workpiece and polishing tool experienced the compression, resulting in the work surface and contact forces. Less working gap induced an increase in compression, increasing the contact forces and work surface. Further, the magnetic flux density is relatively greater when it is closer to magnet, inducing the enhancement of magnetic levitation force acting on the abrasive particles and magnetic attraction force on the CIPs, so that abrasive particles achieved a considerable energy for cutting material, and the CIPs were prone to be attracted leading that the active clusters generated by CIPs in this area were easier to prevent from being broken and improve shape restoration ability on forming ferric clusters. Due to working gap deeply influencing the contact forces, as well as magnetic levitation force acting on abrasive and the magnetic attraction force on active clusters, it affected significantly on the polishing forces.

The ferric clusters were formed by the CIPs when the magnetic field was applied, the number of ferric clusters was positively related to the number of CIPs within the polishing tool, and more volume of MCF slurry supplied could enhance the number of CIPs, leading that the width and height of the polishing tool were increased, i.e., the ferric clusters became longer and stronger. Hence, the compression was much more intensive at the working gap

comparing with small volume of MCF slurry supplied. Concurrently, the working area increased with the increase in the supplied volume. Therefore, forces was increased obviously with the increase of the volume of MCF slurry supplied.

The proportion of MF and CIPs within the MCF slurry was changed for experiments. Commonly, the concentration of CIPs influences tremendously on the intensity of magnetization of the polishing tool which has been demonstrated in Fig. 2.11. A higher magnetic flux density *B* within MCF tool can be achieved with a higher CIPs concentration. This means that the yield stress of the polishing tool that mainly relies on the magnetic flux density will increase with the increasing of CIPs concentration, thus the tangential force was increased. Additionally, the number of ferric clusters increases because more CIPs quantities contained within the MCF slurry which had higher CIPs concentration. Therefore, those formed ferric clusters also became longer and stronger so that they could provide much more powerful magnetic medium for abrasive particles, including the enhanced magnetic levitation force. Thus, those situations combined to increase the normal force.

The surface profile at the A-A cross-section was provided in Fig. 2.18. Most of material was removed in the middle of the polished area, i.e., between R_i and R_o, which corresponded to the middle portion of the working area, meaning that this portion of the working area performed better capacity on removing material. In addition, because the ferric clusters were almost vertical to the surface of the MCF carrier, the MCF tool had the highest point in the working area, which was almost located in the middle portion of the working area according to Fig. 2.19 where the appearance of the MCF tool with MCF 3 slurry was displayed. During polishing, the top tip of the MCF tool was compressed most to remove

material because the ferric clusters around this tip were almost vertical to the surface of the MCF carrier and longest than others. Based on above conditions, the MCF tool can be regarded as a ring-shaped like a regular doughnut and the distance of its top tip to the revolution center of the MCF tool can be obtained by $D = (d_i + d_o)/4$, where d_i and d_o are the diameters of inner and outer rings of the MCF tool. The surface roughness Ra is obtained during polishing, as shown in Fig. 2.20. The surface roughness Ra was variable with polishing time and measured after every 15 min. With MCF 1 slurry, 2.5 ml volume of supplied slurry and working gap h = 3.5 mm, the results showed that this method could smooth successfully the surface of the workpiece to Nano-precision scale. The best surface roughness Ra 10.789 nm has been obtained and it has the potential to polish small curve radius aspheric elements.

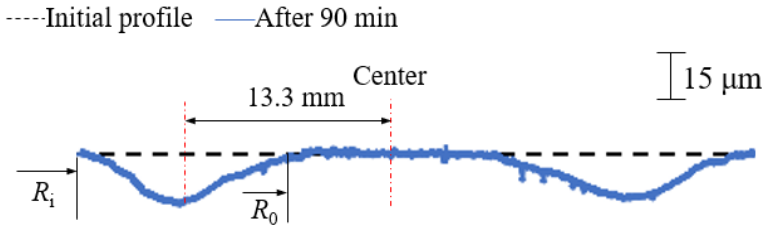

Fig. 2.18 Surface profile at the A-A cross-section.

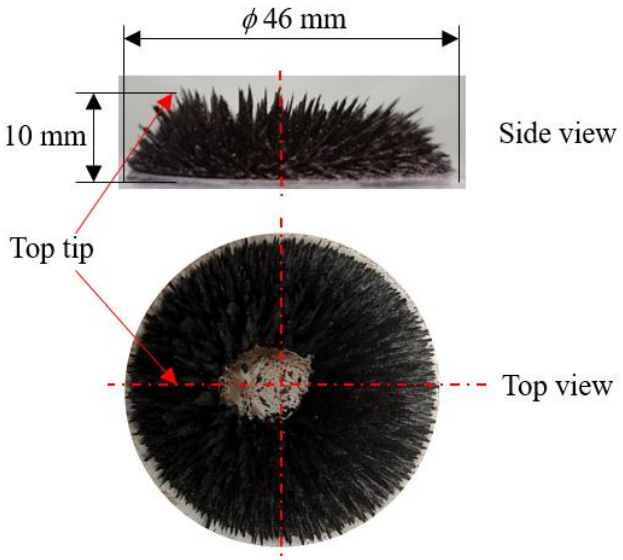

Fig. 2.19 Appearance of the MCF tool.

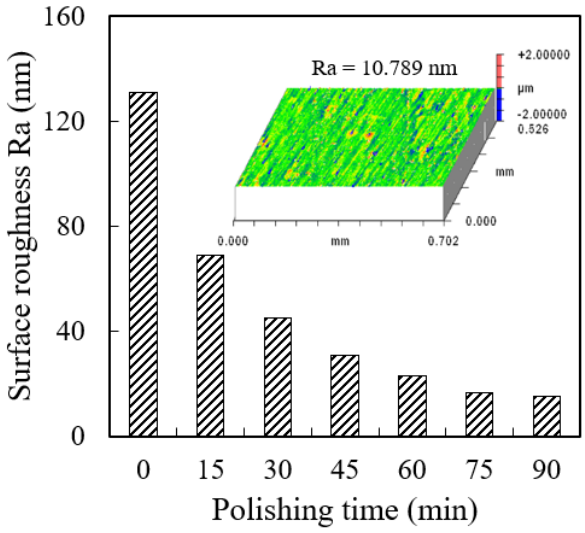

Fig. 2.20 Polishing results in 90 mins and the polished workpiece.

2.5.3 Location and gesture control of aspheric surfaces

As revealed in above report, the portion of the MCF tool locating around the top tip performs best in terms of material removal capacity, most likely for the following reason: the magnetic flux lines, which are vertical to the surface of the MCF carrier, rotate around the axis of the MCF carrier with radius *D* due to the rotary magnetic field, causing the abrasive particles to experience a higher total normal magnetic field strength in one revolution of the rotary magnetic field, which results in a higher total normal force acting on the abrasive particles to enhance the material removal rate [2-3]. According to these analyses, point P is intended to be polished by the top tip of the MCF tool. Meanwhile, its normal line should be parallel to the above-mentioned magnetic flux lines in this work, i.e., it is vertical to the upper surface of the MCF carrier. In practice, the two demands can be realized simultaneously by locating the top tip point o of the workpiece at the corresponding position with the given tilt angle of the workpiece. The detailed procedure was as follows:

As shown in Fig. 2.12(c), the coordinate system xoz is located in the cross-section of the workpiece, in which the origin is the point o and its z-axis coincides with the rotational axis of the workpiece. Subsequently, the tilt angle θ should be set at arctan($z_o' = f'(x_o)$), where $z_o = f(x_o)$ is an expression of the aspheric surface in the xoz-plane, to ensure the verticality of the normal line of point P to the upper surface of the MCF carrier. If the point P (x_o, $z_o = f(x_o)$) is chosen, the tilt angle θ can be subsequently obtained using the relationship $\theta = \arctan(f'(x_o))$. In addition, the distance of point P to the MCF carrier is the working gap h.

The position of the point o (X_o, Z_o) can be related to the point P (X, Z) in XZ-plane using the following equations, where the angle φ is the projection angle of oP in XZ-plane:

$$X_o = X - oP\cos\varphi, \tag{2-5}$$

$$Z_o = Z + oP\sin\varphi. \tag{2-6}$$

As mentioned above, the target position P (X, Z) in XZ-plane is P (D, h). To solve for (X_o, Z_o), the parameters and the following equations are substituted into Eqs. (2-5)–(2-6):

$$oP = \sqrt{x_o^2 + f(x_o)^2}, \tag{2-7}$$

$$\varphi = \theta - \arctan(f(x_o)/x_o), \tag{2-8}$$

yielding the following:

$$X_o = D - \sqrt{x_o^2 + f(x_o)^2}\cos(\theta - \arctan(f(x_o)/x_o)), \tag{2-9}$$

$$Z_o = h + \sqrt{x_o^2 + f(x_o)^2}\sin(\theta - \arctan(f(x_o)/x_o)). \tag{2-10}$$

It is in addition figured out from Fig. 2.12(c) that the MCF tool should be prepared with the appropriate dimensions according to the shape and size of the work surface; if the inner and outer diameters of the doughnut-shaped MCF tool are too small relative to the work surface size, when the target point P is polished with the right portion of the MCF tool, the

other different point on the same work surface might be unwillingly polished with the left portion of the MCF tool, resulting in the deteriorated form accuracy of work surface; by contrast if the MCF tool size is too big, the working area of the MCF tool would be too wide, leading to the difficulty in controlling the form accuracy and enhancing the polishing efficiency. Therefore, the dimensions of the MCF tool should be determined appropriately and thus as long as the polishing conditions including the motion path of the MCF tool on the work surface have been set optimally, the whole work surface could be finished precisely and effectively. The details will be further described in next chapter.

Summary

(1) The shear stress of the MCF 2 slurry increased with the increase in shear rate and magnetic field strength. Regardless of the magnetic field, when shear rate increased from 0 to 100 1/s, shear stress enhanced sharply and then a little decreased before shear rate reached 300 1/s, at last, it kept almost a small increase rate with the increase of shear rate. The maximum shear stress was almost 100 KPa when 0.8 T of magnetic flux density *B* and 1000 1/s of shear rate were applied.

(2) The viscosity of the MCF 2 slurry decreased with the increase in shear rate and increased with the increase in magnetic flux density *B*. When shear rate increased from 0 to 100 1/s, the viscosity decreased quickly, and then kept a small decrease rate as the increase in shear rate. With high magnetic field strength, MCF slurry was hard to change the character from a solid-like to a liquid, because the ferric clusters were much stronger than that with low magnetic field strength.

(3) The *M-B* curves demonstrated that the magnetic property of the MCF slurry was

strengthened when higher CIPs concentration was used within MCF slurry.

(4) The shear stress and viscosity were affected significantly by CIPs concentration and magnetic field strength.

(5) The top tip of the MCF tool was located at a distance D to the revolution center of the MCF tool and performed better ability on removing material. The D could be obtained by using $D = (d_i + d_o)/4$, i.e., the middle portion of the working area. The workpiece was polished to the nano-precision scale. Thus, it was certain that this method was potential for polishing materials.

References

[1] Kunio Shimada, Yongbo Wu and Yat Choy Wong, Effect of magnetic cluster and magnetic field on polishing using magnetic compound fluid (MCF), Jouranl of Magnetism and Magnetic Materials, 262(2003) 242-247

[2] Hideki Kawakubo and Masaki Kamijima. Polishing for Ferromagnetic Materials using Workpiece Oscillation Type Magnetic Polishing Method. The Japan Society for Precision Engineering. 2010; B43; 139-40

[3] Shimada, K., Akagami, Y., Kamiyama, S., Fujita, T., Miyazaki, T., Shibayama, A., 2002.New microscopic polishing with magnetic compound fluid (MCF). J. Intell. Mater.Syst. Struct. 13, 405–408.

Chapter Ⅲ The Novel Doughnut-shaped MCF Tool

3.1 Introduction

As mentioned in the above chapters, MCF slurry performed excellent properties that it produced a larger magnetic pressure and a higher apparent viscosity compared with MF, and had greater stability of particle dispersion than that of MR fluid under the same magnetic field. Moreover, it was a smart slurry that could be governed easily by the magnetic field and shear rate. Hence, a series of applications were recommended such as abrasive slurry used for precision surface finishing, smart damper for absorbing quake, rubber-based smart sensors and so on.

MCF slurry commonly behaved as a Newtonian fluid without the magnetic field. In contrast, once the MCF slurry was exposed to a magnetic field, it was stiffened rapidly and exerted characteristics of the viscoplastic fluid because the internal structure of the MCF slurry was changed in which plenty of chain-shaped ferric clusters were formed by the applied magnetic field [1]. Wu found that the behavior of the MCF slurry under a magnetic field and the performance in polishing surfaces were affected significantly not only by process parameters but also by the motion of the applied magnetic field [2]. It was reported that when a static magnetic field, which the magnetic flux density and the spatial distribution of the magnetic line of force were constant, resulted that the geometrical shape of the formed polishing tool and the size/distribution of the magnetic clusters generated within the MCF slurry were kept as they were. In these cases, APs within the MCF tool

were dispersed unevenly owing to the uneven distribution of magnetic clusters [3]. Therefore, these behaviors were unfavorable for its process performance. In order to overcome these behaviors and improve the process performance of the formed MCF tool, a rotary magnetic field where the magnetic flux density was kept constant but its spatial distribution was always fluctuated was applied by locating the magnet with a distance to its revolution axis. Consequently, the mount-shaped MCF tool was invented in which a certain geometrical shape was formed by itself and APs dispersity was greatly improved due to the even distribution of the magnetic clusters. Guo investigated the formation process of this kind of MCF tool within a period of the magnet revolution and used the MCF tool for surface finishing [4]. The formed clusters changed their orientations during the revolution of the magnet. Simultaneously, the outstanding improvement in finishing variable surfaces was confirmed by Guo and Wang after polishing a series of workpieces construed by different materials. Furthermore, Jiao reported that CIPs within the MCF tool were observed to form the ferric clusters along the magnetic flux lines, and as discovered by Wang, APs were attached or entrapped into the clusters due to the magnetic levitation force acting on the APs [5].

The doughnut-shaped MCF tool was proposed by the inspiration of the methods proposed by Wu and Jiao. A ring-shaped magnet and the eccentric distance were employed to generate the variable magnetic field for forming the novel MCF tool. Although the feasibility of polishing was confirmed experimentally, the formation process of the MCF tool and the behaviors of CIPs and APs were still important to completely understand its characteristics when used in finishing surfaces. In this chapter, the self-shape formation

process of the novel MCF tool under a rotary magnetic field generated by a ring-shaped magnet is first clarified to see how the parameters affected the time required for forming the MCF slurry to its final appearance and the final geometry, followed by the investigation on the observation of the internal structure of MCF tool for clarifying the behaviors of the CIPs and APs. At last, based on the results, a material removal model was proposed.

3.2 Experimental details

To systematically study the characteristic of the novel method and its ability on material removal, experiments were carried out in two steps. In the first step, to achieve the proper doughnut-shaped MCF tool, the formation process of the MCF tool was observed under different process parameters (r, n_c, n_m, V). After then, the distribution of magnetic field within the MCF tool was analyzed and the internal structure of the MCF tool was also observed for confirming the behaviors of CIPs and APs.

Table 1

Experimental conditions in the experiments

Parameters	Value
Working gap h (mm)	1, 1.5, 2, 2.5, 3, 3.5
Volume of MCF supplied V (ml)	1, 1.5, 2, 2.5
Eccentricity r_e (mm)	0, 2, 4, 6, 8
MCF carrier revolution speed n_c (rpm)	0, 100, 200, 300, 400, 500
Magnet revolution speed n_m (rpm)	200, 500, 800, 1100, 1400

Table 1 shows the conditions used in the experiments and the MCF 2 slurry was used in these experiments. In addition, as the magnetic field applied to the MCF slurry is generated

by the ring-shaped permanent magnet and hence its strength was kept constant during polishing.

3.3 Preparation of workpieces

For designers, they are going to design the most optimized optical system with properties of lower weight, higher strength, and stiffness, appropriate thermal conductivity if the composited material is needed, perfect manufacturability and cheap. Hence, they will not only design the structures for the system but also consider the materials for aspheric optical elements to achieve the most perfect performance once the designed products are in application. Conventional materials such as metals, optical plastics, and crystals, IR materials were used widely for the optical system in industry and commerce [6]. Further, CFC, SiC, CSiC, and other specific materials, were invented continually to meet the variable applications, due to the increasing variety of the products and demanding on the high quality. Among those material mentioned above, aluminum and aluminum alloys are considered to be an appropriate material to meet these demands [7] because of their prominent physical properties, stable chemical properties, and low production costs. Thus, the aluminum alloy 6061 was adopted in this work.

The appearance of the conic workpiece is displayed in Fig. 3.1 with approximately a 90-nm initial surface roughness Ra. The distances of the fringes of the polishing area to the top tip of the conic workpiece are l_o and l_i along the generatrix, the corresponding radii are R_{lo} and R_{li}, respectively, and the basic angle α is 20°.

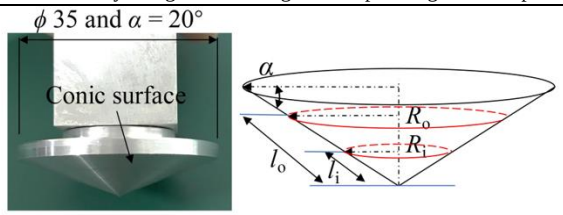

Fig. 3.1. Appearance of workpieces.

3.4 Formation process

The approach used to observe the formation process of the MCF tool is illustrated in Fig. 3.2. Initially (t = 0 s), a given amount of MCF slurry was ejected toward the center of the upper surface of the MCF carrier through the nozzle of an injector without rotational motion of the MCF carrier and the magnet holder. Once the whole MCF slurry was attracted steadily by the magnetic force generated by the magnet, the magnet holder was rotated around its own axis to generate the rotary magnetic field, and the MCF carrier began to rotate synchronously, causing the structure and geometry of the MCF slurry to vary with time from the initial state to form a stable MCF tool. Additionally, the total time required to form the stable MCF tool was regarded as the formation time T. The variation process of the appearance of the MCF tool was captured by observing its side-view and top-view sequentially using high-speed cameras (VW6000 by Keyence Co., Ltd.), as shown in the right portion of Fig. 3.2. The same procedure was repeated for different process parameters.

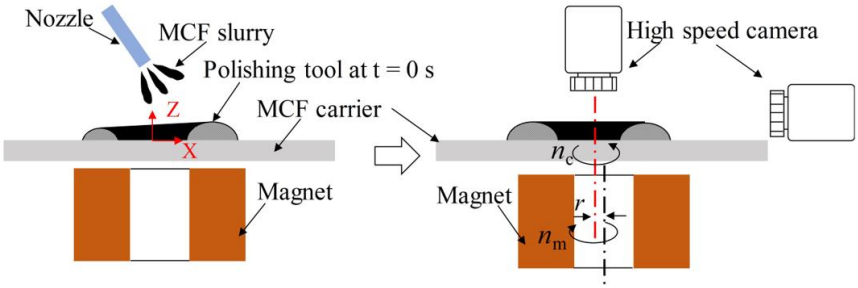

Fig. 3.2. Illustration of MCF tool appearance observation.

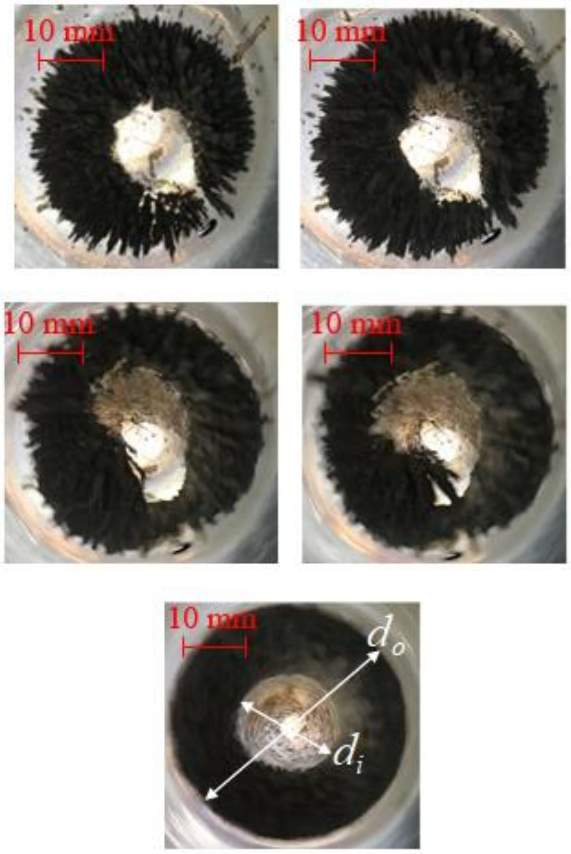

Fig. 3.3. Variation of the appearance of a typical MCF tool with time.

$r_e = 0$ $r_e = 2$

$r_e = 4$

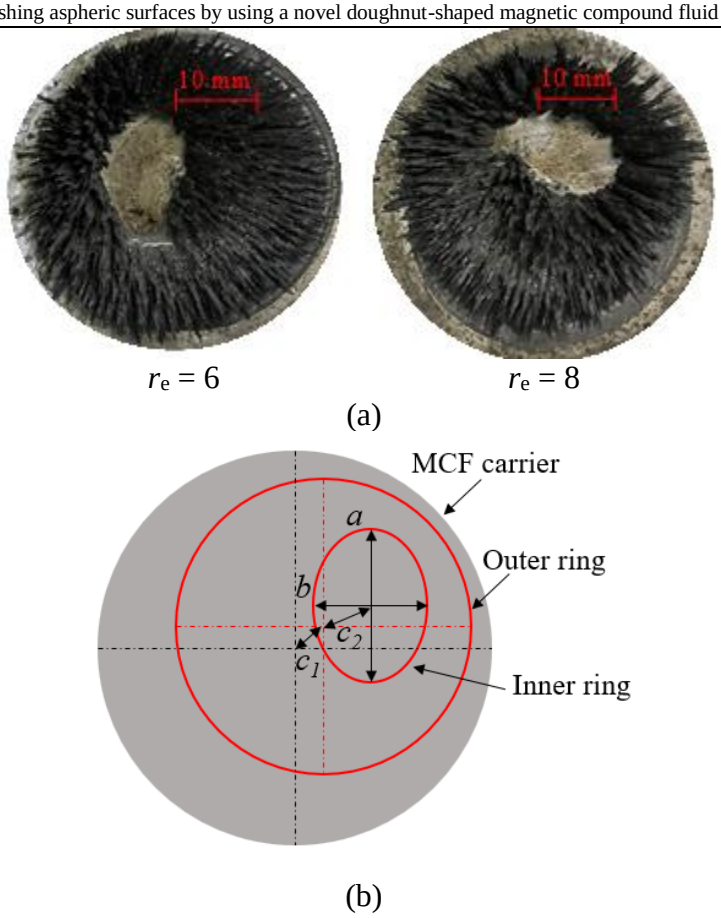

Fig. 3.4. (a) Optical external images of MCF tools formed with different eccentricities and (b) the geometry model of the polishing tool.

Figure 3.3 shows the variation of the appearance of a typical MCF tool with time with V = 1.5 ml and r = 4 mm. A remarkable slit was observed in the initial state (t = 0 s) at the end of ejection. Once the magnet holder and MCF carrier began to rotate at n_m = 500 rpm and n_c = 300 rpm, respectively, the slit was gradually eliminated, causing the external shape of the MCF tool to vary rapidly. Eventually, the terminal doughnut-shaped MCF tool with an inner diameter of d_i and an outer diameter of d_o was obtained in T = 0.2 s. Moreover, the terminal shape of the MCF tool was clean-cut and distinguishable at different eccentricity values, as shown in Fig. 3.4(a). Therefore, it is essential to optimize the process parameters to form the proper MCF tool.

A quantitative investigation on the terminal dimension of the MCF tool and corresponding formation time T under different parameters were conducted. Based on the results in Fig. 3.4(a), the terminal shape of the MCF tool is simplified in the right portion of Fig. 3.4(b). The outer and inner rings of the MCF tool can be respectively regarded as a regular circle and an ellipse with long and short diameters a and b, respectively. The c_1 is the distance of the outer ring center to the axis of MCF carrier, and the c_2 is the distance between the centers of the outer and inner rings. Once the conditions of $a \approx b \approx d_i$, $c_1 \approx 0$, and $c_2 \approx 0$ are satisfied, a MCF tool with a complete terminal shape was achieved. In this case, the deviation of the working area can be avoided as much as possible during polishing with the MCF tool rotating, achieving a stable material removal rate. The detailed results are shown in Figs. 3.5–3.7.

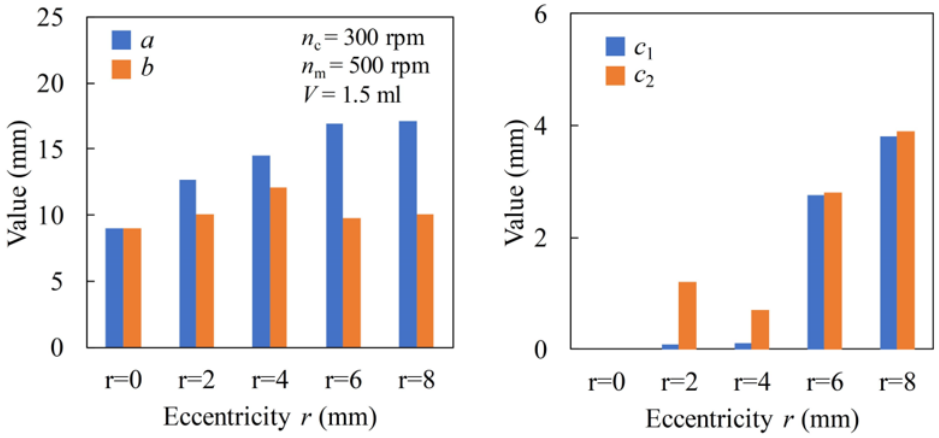

(a) (b)

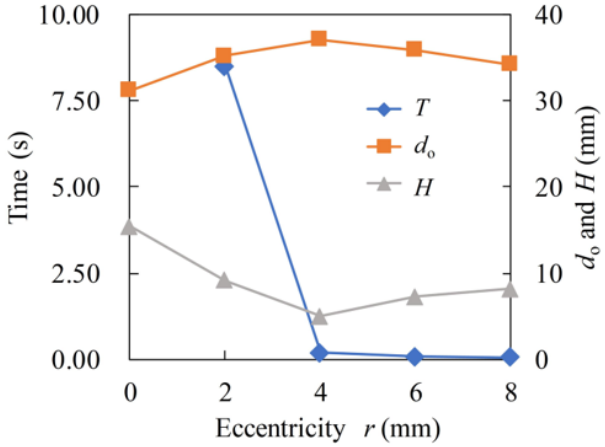

(c)

Fig. 3.5. Effects of r on (a) a and b, (b) c_1 and c_2, and (c) T, d_o, and H.

The effects of the eccentricity r on the terminal dimension and formation time T of the MCF tool are summarized in Fig. 3.5. The differences between a and b at different eccentricities are shown in Fig. 3.5(a). The value of a increased with increasing r, but the rate of increase decreased once r reached 6 mm. However, the value of b increased first and subsequently declined when r was beyond 4 mm. The smallest difference between a and b was found at r = 4 mm. As shown in Fig. 3.5(b), c_1 maintained small values near 0.1 mm and subsequently sharply increased when r was beyond 4 mm. However, c_2 decreased when r = 4 mm compared with that when r = 2 mm, and subsequently ascended as r increased. It must be emphasized that although the MCF slurry gathered to form a real concentric doughnut-shaped MCF tool ($a = b$ = 9.00 mm and $c_1 = c_2$ = 0 mm) when r = 0 mm, a MCF tool with a jagged appearance was eventually formed. However, for the terminal shape of the MCF tool, a well-formed doughnut-shaped MCF tool was eventually obtained at r = 4 mm, as shown in Fig. 3.4(a).

The effects of the eccentricity r on the formation time T, outer ring diameter d_o, and height H of the MCF tool are shown in Fig. 3.5(c). The most notable feature of these curves

is the change of T with increasing r. When r = 0 mm, the terminal shape of the MCF tool was maintained at the initial state due to the concentric rotation of the magnetic field. Thus, the counting of the formation time was meaningless. The eccentricity r = 0 mm was thereby excluded from consideration. When r increased from 2 to 4 mm, T declined sharply. However, the decline rate decreased when r was larger than 4 mm. Moreover, d_o increased to a maximum (37 mm) at r = 4 mm and subsequently decreased gradually. Meanwhile, the opposite variation tendency occurred for the height H because a constant volume of MCF slurry was supplied. Consequently, in the remaining experiments, the eccentricity r was set to 4 mm.

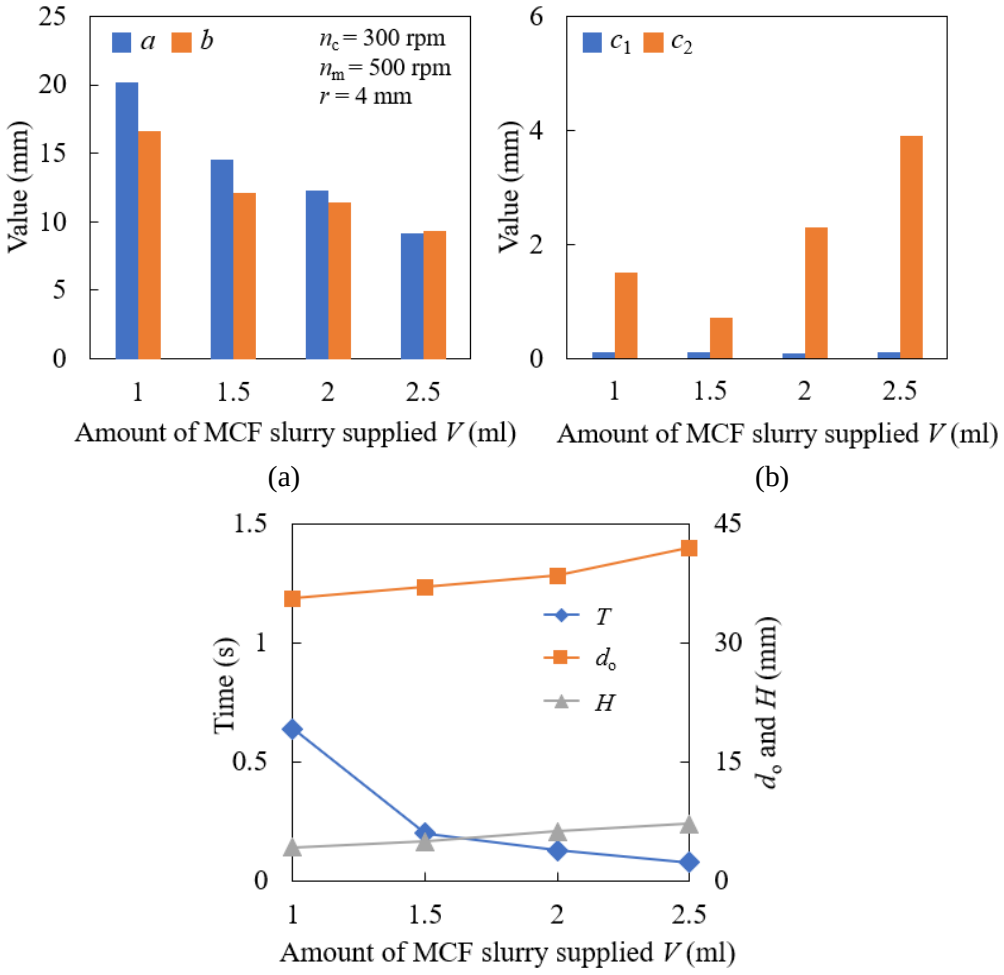

Fig. 3.6. Effects of V on (a) a and b, (b) c_1 and c_2, (c) T, d_o, and H.

The effect of the amount of MCF slurry supplied V on the geometry and formation time T of the MCF tool is displayed in Fig. 3.6. As displayed in Fig. 3.6(a), a and b decreased with the increasing V, but the difference between a and b became smaller as V increased. As displayed in Fig. 3.6(b), the values of c_1 were constant and were close to 0 mm, regardless of the variation of V. c_2 decreased to a minimum first and subsequently increased with increasing V. Moreover, the smallest difference was observed between c_1 and c_2 when 1.5 ml of V was supplied. As shown in Fig. 3.6(c), T decreased, whereas the width and height increased with increasing V. T decreased by almost 64% when V increased from 1 to 1.5 ml, after which the decreasing tendency reduced gradually as V increased. A greater value of V led to smaller slit formation in the initial state, which directly benefited the shortening of T. Thus, a relatively perfect MCF tool could be obtained when 1.5 ml of MCF slurry was supplied.

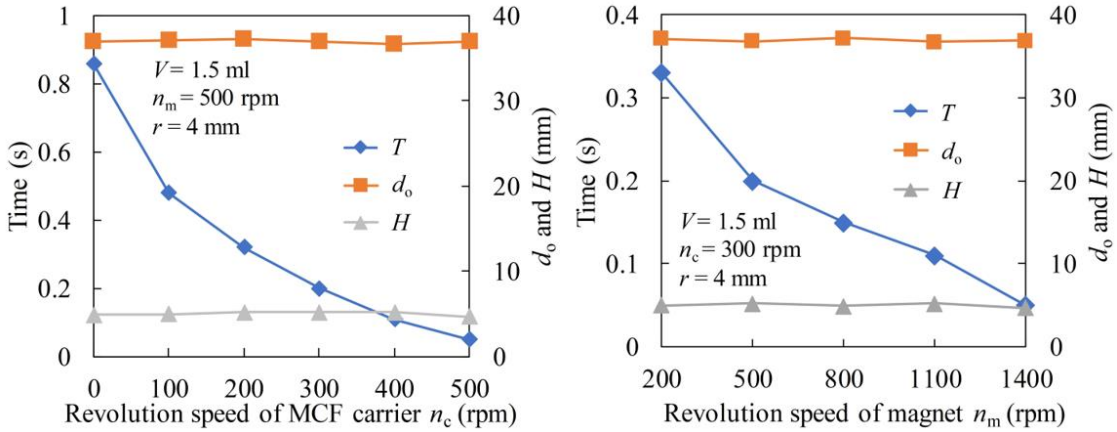

Fig. 3.7. Effects of (a) n_c and (b) n_m on T, d_o, and H.

The effects of the rotation speed of MCF carrier n_c on the formation time T, the outer ring diameter d_o, and the height H of the MCF tool are shown in Fig. 3.7(a). T decreased sharply as n_c increased. However, no significant difference from the dimension of the

formed MCF tool was found, even though n_c increased. The relative motion between the MCF slurry and magnet was intensified when n_c and n_m were applied together, which is beneficial for improving the stirring of the MCF slurry using a rotary magnetic field, resulting in the rapid elimination of the slit. However, the MCF slurry began to spill out due to the high centrifugal force when n_c exceeded 300 rpm. This phenomenon was adverse to maintaining a high polishing efficiency of the MCF tool because the proportion of components contained in the MCF tool changed significantly. Thus, n_c was set at 300 rpm for the remaining experiments. Fig. 3.7(b) shows the effects of the revolution speed of the magnet n_m on the formation time T, the outer ring d_o, and the height H of the MCF tool. As n_m increased, d_o and H were nearly constant, but the formation time decreased sharply. When it exceeded 500 rpm, the ability to shorten the formation time decreased. However, the variation in n_m also had no impact on the geometry of the MCF tool. Therefore, 500 rpm was adopted for the following experiments.

In conclusion, a perfect MCF tool could be obtained when the eccentricity r, the rotation speed of the MCF carrier n_c, the revolution speed of the magnet n_m, and the amount of MCF slurry supplied V were 4 mm, 300 rpm, 500 rpm, and 1.5 ml, respectively, resulting in a MCF tool with dimensions of a = 14.50 mm, b = 12.10 mm, c_1 = 0.12 mm, c_2 = 0.71 mm, d_o = 37 mm, and H = 5.00 mm in the current work. Thereby, this MCF tool was used in the following experiments.

3.5 Internal structure of MCF tool

3.5.1 Preparation of MCF tool sample

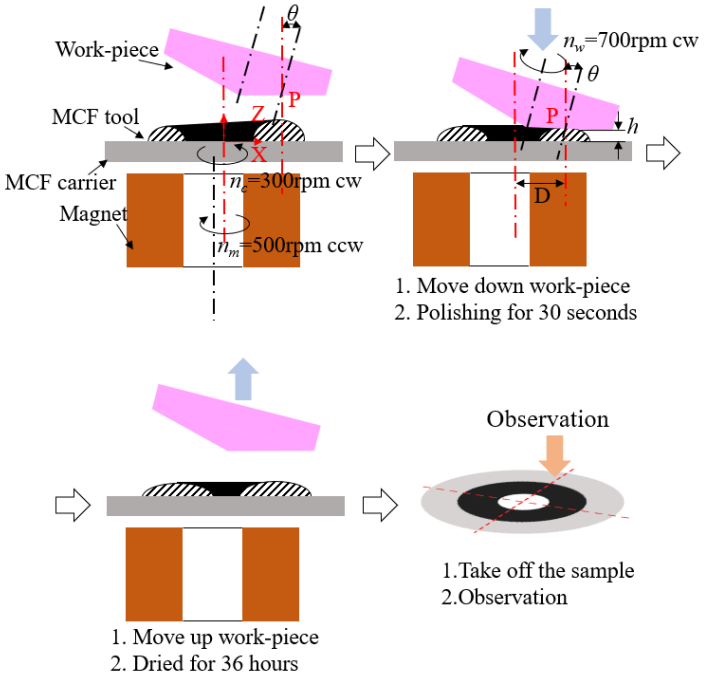

Fig. 3.8. Sample preparation of the MCF tool.

To investigate the behaviors of CIPs and APs, a sample MCF tool used in the conic surface polishing was prepared using the procedure illustrated in Fig. 3.8. First, a stable MCF tool was formed using the optimal parameters. The rotational motions of the MCF carrier and the magnet holder were subsequently stopped. The rotating workpiece (n_w = 700 rpm) was located above the MCF carrier without touching the MCF tool. After adjusting the tilt angle θ, it was moved to the target position (D, h) followed by polishing for 30 s. Thereafter, all the motors were shut down, the workpiece was moved up to detach it from the MCF tool, and it was naturally dried for 36 h. Finally, the sample was removed for observation.

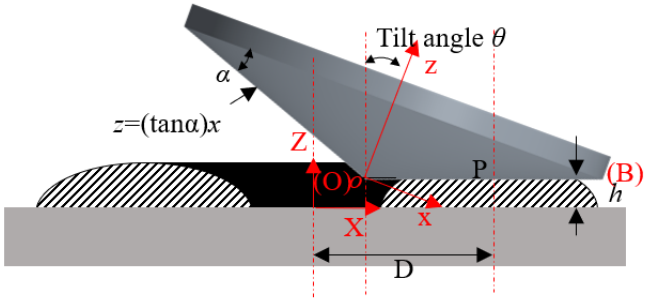

Fig. 3.9. Schematic for locating workpiece.

The values of (D, h), the tilt angle, and the location of point o (X_o, Z_o) in the preparation of a MCF tool sample were determined as follows. As shown in Fig. 3.9, the value of D could be obtained using the formula $D = (d_i + d_o)/4 = 12.58$ mm, where d_i was determined by the average value of a and b, namely $d_i = (14.5+12.1)/2 = 13.3$ mm. The tilt angle was set to arctan ($z_o' = f'(x_o)$) = 20°, where $z_o = f(x_o) = (\tan\alpha)x_o$, due to the choice of the point P ($x_o = 8.00$, $z_o = 3.00$) in xz-plane. Furthermore, the working gap of $h = 1.00$ mm was set. Moreover, point o ($X_o = 4.07$, $Z_o = 1.00$) in XZ-plane can be determined using Eqs. (2-9) and (2-10).

3.5.2 Magnetic field

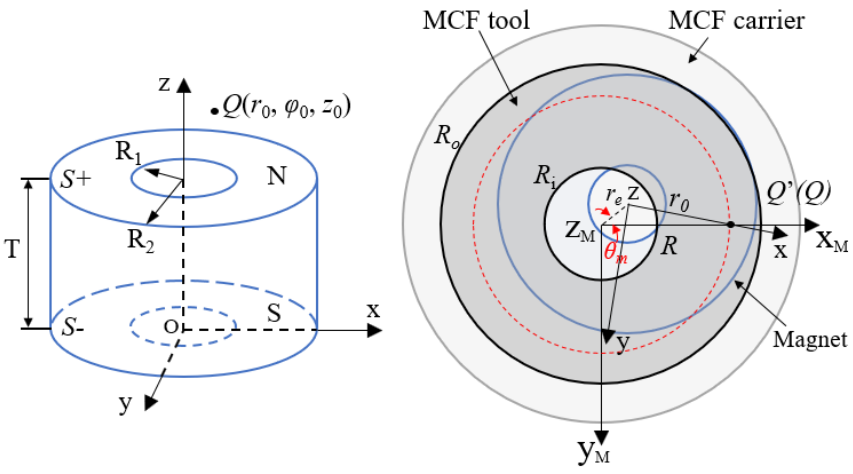

(a) (b)

Fig. 3.10. Model for the analysis of the magnetic field: (a) the dimensions of the magnet and (b) relative positions of the magnet and MCF tool.

To comprehensively understand the effect of the MCF slurry on polishing characteristics, the behavior of ferric clusters and APs within the MCF slurry during polishing should be examined. In conventional MCF polishing, ferric clusters gather in line along the magnetic line of force and stir the APs under the rotary magnetic field. APs are forced onto the work-surface in the working area due to the magnetic field. However, it is yet unclear if similar phenomena occur in the novel method. Thus, the distribution density of the magnetic flux *B* was analyzed firstly. As shown in Fig. 3.10(a), a ring-shaped magnet with an inner radius R_1 (4.5 mm), an outer radius R_2 (15 mm) and a thickness T (20 mm) has been magnetized evenly in its z-axis direction, and thus, the magnetic poles only exit at the upper/lower surfaces of the magnet (S+ and S-) because of the magnetic field [8]. A cartesian xyz coordinate was established at the center of the lower surface of the magnet, according to which a cylindrical coordinate was defined, where the location of an arbitrary point can be expressed as (r_0, φ_0, z_0). Based on the rules of magnetic symmetry and the magnetic scalar potential, the magnetic field intensity *H* and the corresponding components H_{r0}, $H_{\varphi 0}$, and H_{z0} in the cylindrical coordinate should be only considered in the x–z plane ($\varphi_0 = 0$, $H_{\varphi 0} = 0$). Once values of r_0 and z_0 are given to the following equations, the magnetic field intensity *H* can be resolved, followed by obtaining the magnetic flux density *B* acting on point *Q* (r_0, φ_0, z_0).

$$H_{r_0}(r_0, \varphi_0, z_0) = \frac{M}{4\pi} \iint_{S+} \frac{r_0 - x}{\sqrt[3]{(r_0-x)^2+y^2+(z_0-h)^2}} ds - \iint_{S-} \frac{r_0 - x}{\sqrt[3]{(r_0-x)^2+y^2+{z_0}^2}} ds \quad (3\text{-}1)$$

$$H_{\varphi_0}(r_0, \varphi_0, z_0) = \frac{M}{4\pi} \iint_{S+} \frac{y}{\sqrt[3]{(r_0-x)^2+y^2+(z_0-h)^2}} ds - \iint_{S-} \frac{y}{\sqrt[3]{(r_0-x)^2+y^2+{z_0}^2}} ds \quad (3\text{-}2)$$

$$H_{z_0}(r_0, \varphi_0, z_0) = \frac{M}{4\pi} \iint_{S+} \frac{z_0 - h}{\sqrt{(r_0 - x)^2 + y^2 + (z_0 - h)^2}} ds - \iint_{S-} \frac{z_0}{\sqrt{(r_0 - x)^2 + y^2 + z_0{}^2}} ds \quad (3\text{-}3)$$

$$M = B_r / \mu_0 \quad (3\text{-}4)$$

$$B = \mu_0 H \quad (3\text{-}5)$$

$$B(r_0, \varphi_0, z_0) = \sqrt{B_{r_0}^2(r_0, \varphi_0, z_0) + B_{\varphi_0}^2(r_0, \varphi_0, z_0) + B_{z_0}^2(r_0, \varphi_0, z_0)} \quad (3\text{-}6)$$

where M and B_r are the magnetization and remanence of the magnet, respectively, and μ_0 is the permeability in a vacuum. Substituting Eqs. (3-4) and (4-5) into Eqs. (3-1)-(3-3), the components of the magnetic flux density B can be obtained, then the resultant magnetic flux density B (r_0, φ_0, z_0) at point Q (r_0, φ_0, z_0) can be obtained by using Eq. (3-6).

The relative position between the MCF tool and the magnet is illustrated in Fig. 3.10(b). The $x_M y_M z_M$ cartesian coordinate was constructed and fixed in the ground. The x_M-y_M plane was located in x-y plane and z_M was overlapped to the revolution axis of the magnet. Thereby, point Q is represented by Q' in the $x_M y_M z_M$ coordinate system, R is the distance from Q' to the center of the MCF tool, and θ_m is the rotation angle of the magnet when the magnet revolves around the z_M-axis. Thus, r_0 can be determined by R, with $r_0 = R^2 + r_e^2 - 2Rr_e\cos\theta_m$. The magnetic field at point Q' can be also obtained by selecting the values of R, θ_m, and z_M, where z_M is the same as z_0.

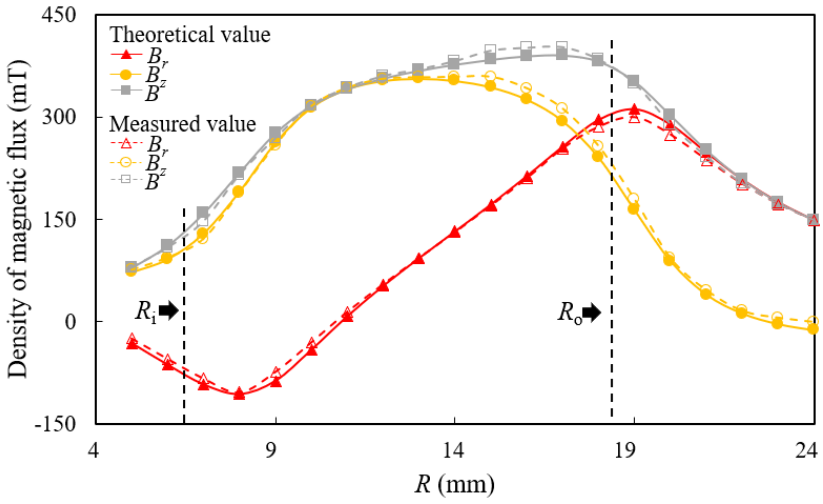

Fig. 3.11. Distribution of B at the point (R, 0, 22) when $\theta_m = 0°$.

The upper surface of the magnet was very close to the lower face of the MCF carrier, and the small clearance between the magnet and MCF carrier could be ignored compared to the working gap h. The thickness t of the MCF carrier was 1 mm, and thus, the relationship between working gap h and the distance of point Q' to the lower surface of the magnet (S-) z_M can be represented by $z_M = t + h + T$.

Fig. 3.11 displays the magnetic flux density at different point Q' along x_M-axis at $z_M = 22$ mm, i.e., $\theta_m = 0°$ and $h = 1$ mm. When the radius of the MCF tool R ranged from the inner ring ($R_i = 6.6$ mm) to the outer ring ($R_o = 18.5$ mm), i.e., r_0 ranged from 2.6 to 14.6 mm, an arbitrary point locating at the line OB (Fig. 3.9) can be presented by point Q'. To confirm the analytical results, the actual magnetic flux density at the corresponding position was measured by a high precision teslameter (5070G/Teslameter), and the results are plotted in the same figure. The theoretical values were similar to the measured ones, and the magnetic flux density B was the greatest near the outer ring of the MCF tool and the smallest near the inner ring of the MCF tool. The maximum B_z was found at $R = 11$ mm and $R = 13$ mm, which were very close to the middle of the working area of the MCF tool ($R = 12.58$ mm).

However, the B_r began to increase with the increase in R when R ranged from 8 to 18 mm, whereas the opposite tendency was found when 4.5 mm < R < 8 mm and 19 mm < R < 24 mm. The analytical method was valid and could be used in the following analysis.

3.5.3 Behavior of ferric clusters

Jiao, et al. confirmed that the ferric clusters formed along the magnetic lines of force during the surface finishing using the MCF wheel [9]. To determine if this behavior also occurred in the current work with the novel MCF tool, a vector graph of the magnetic field in the x_M-z_M plane was constructed based on the results in Fig. 3.11. The vector graph is shown in Fig. 3.12, where the arrows depict the orientations of the magnetic lines of force. The orientation of magnetic lines of force gradually became perpendicular to the surface of the MCF carrier from the inner ring of the MCF tool to near the middle portion of the working area. The magnetic line of force had an angle of 88.8° relative to the surface of the magnet when R reached 11 mm, and even remained nearly vertical with an angle of 75.4° when R reached 13 mm (middle portion of the working area), after which it tended to be parallel to the surface of the MCF carrier until R increased to R_o. Given that the ferric clusters are formed along the magnetic lines of force, the orientation of the ferric clusters would be similar to that of the magnetic lines of force.

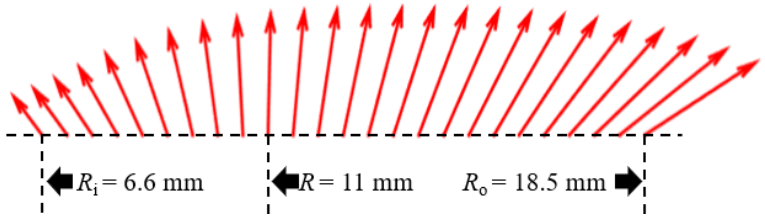

Fig. 3.12. Analysis of the magnetic lines of force.

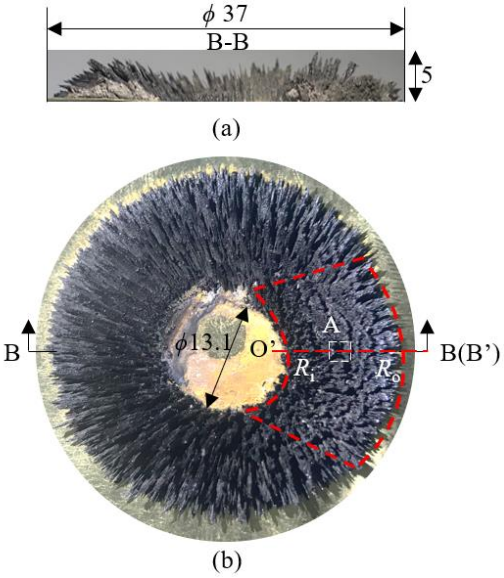

Fig. 3.11. Optical images of the MCF tool with the MCF2 slurry: (a) side view of the B-B cross-section and (b) top view of the whole MCF tool.

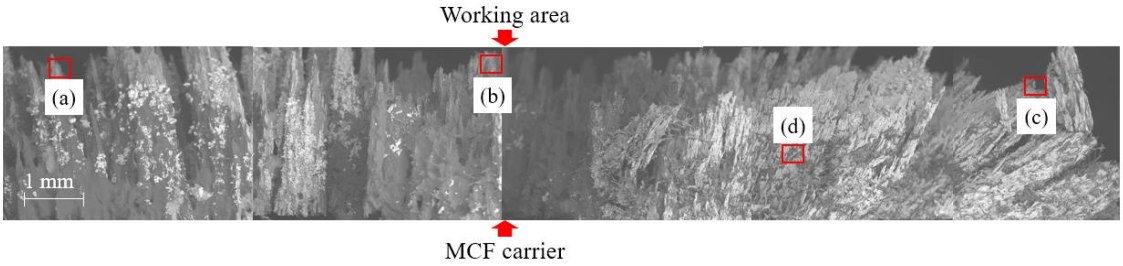

Fig. 3.12. SEM image of the B-B cross-section at O'B'.

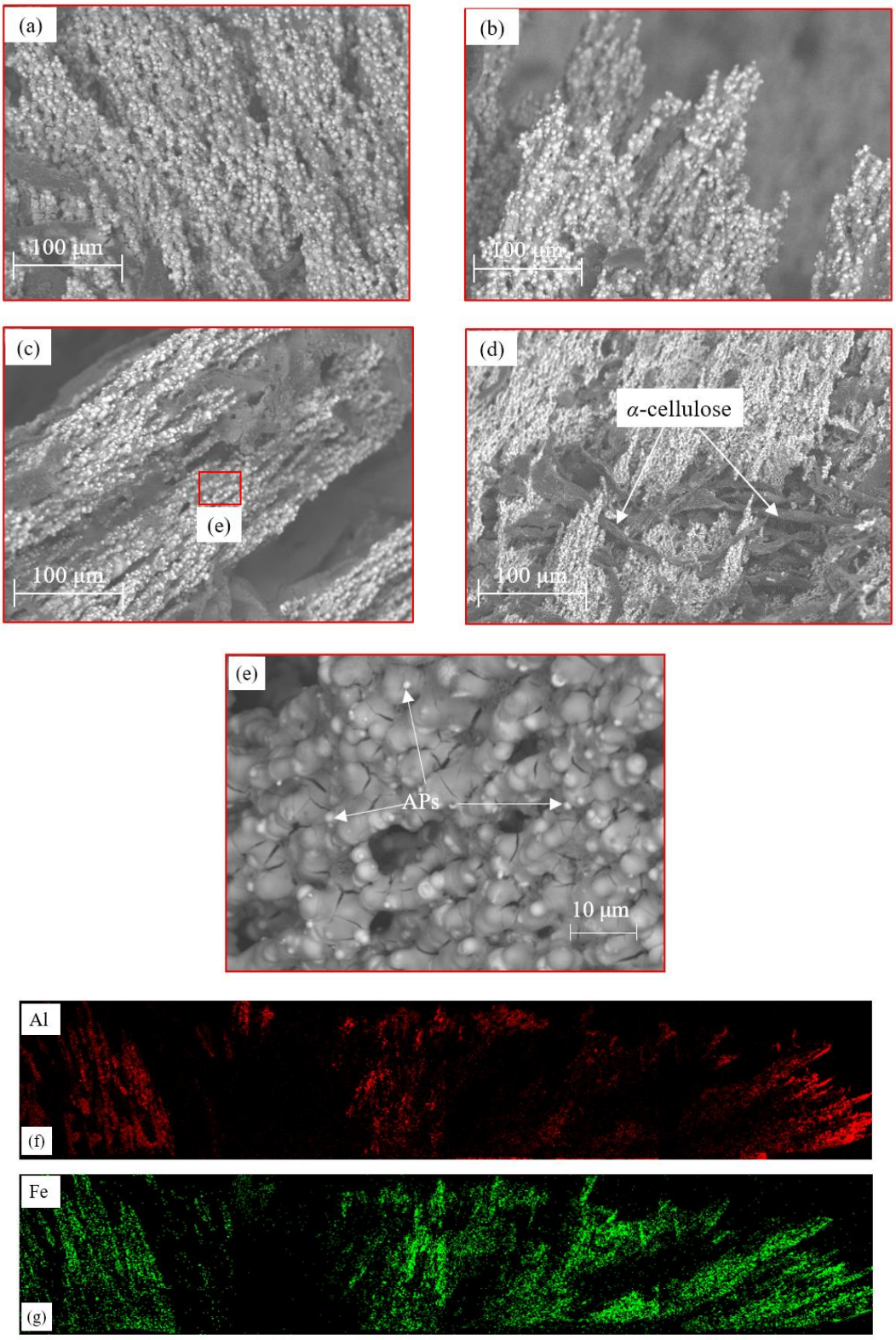

Fig. 3.13. Typical orientation of the ferric clusters: (a) inner side, (b) middle portion, and (c) outer side. Typical distribution of (d) *α*-cellulose, (e) Aps, (f) Al element, and (g) Fe element.

To verify the above-predicted orientation of ferric clusters, a sample of MCF tool with the MCF 2 slurry was prepared using the procedure reported previously. The prepared MCF tool sample is shown in Fig. 3.11, in which the abundant ferric clusters can be observed directly. The portion of the MCF tool being used is highlighted with the red dashed line. The ferric clusters within the working area were further studied using the scanning electron microscopy (SEM) and energy-dispersive X-ray spectroscopy (EDX).

Fig. 3.12 shows the SEM image of the B-B cross-section at O'B'. A number of spikes, as composed of ferric clusters, were observed and their orientations were different at different positions corresponding to those of the magnetic lines of force. The internal structures of the tool at different positions were further observed by enlarging the SEM images at the positions located in (a) the top surface close to the inner ring, (b) the top surface around the middle area, (c) the top surface close to the outer ring, and (d) the inward area between (b) and (c).

Starting from location (a), the clusters gradually changed their orientations clockwise, and the clusters at the location (b) were almost vertical to the upper surface of the MCF carrier. Then, the clusters continued to change the orientations clockwise from being vertical to being in parallel with the upper surface of the MCF carrier. Comparing these results with that in Fig. 3.10, it was indicated that the ferric clusters were formed along the magnetic lines of force within the MCF tool, which was as predicted theoretically. Additionally, α-celluloses were interleaved between the clusters, which increased the shear resistance of the MCF tool, as shown in Fig. 3.13(d). Fig. 3.13(e) is a typical SEM image that was obtained by enlarging a portion of Fig. 3.13(c), showing that the APs appeared

around the clusters. These APs at the designated working gap can be categorized into two types. Some Aps, as located originally in the relatively large working gap, were compressed by the work-surface to the designated working gap, while others were the originally resided ones in the designated working gap.

The EDX mapping results in Figs. 3.13(f) and (g) show the distribution of Al and Fe elements on the B-B cross-section at O'B', implying that the alumina (Al_2O_3) APs were evenly distributed inside the MCF tool, and simultaneously attached to the ferric clusters, which were mainly composed of CIPs. Thus, the clusters can stir the APs effectively as a result of the conical pendulum motions under the rotary magnetic field.

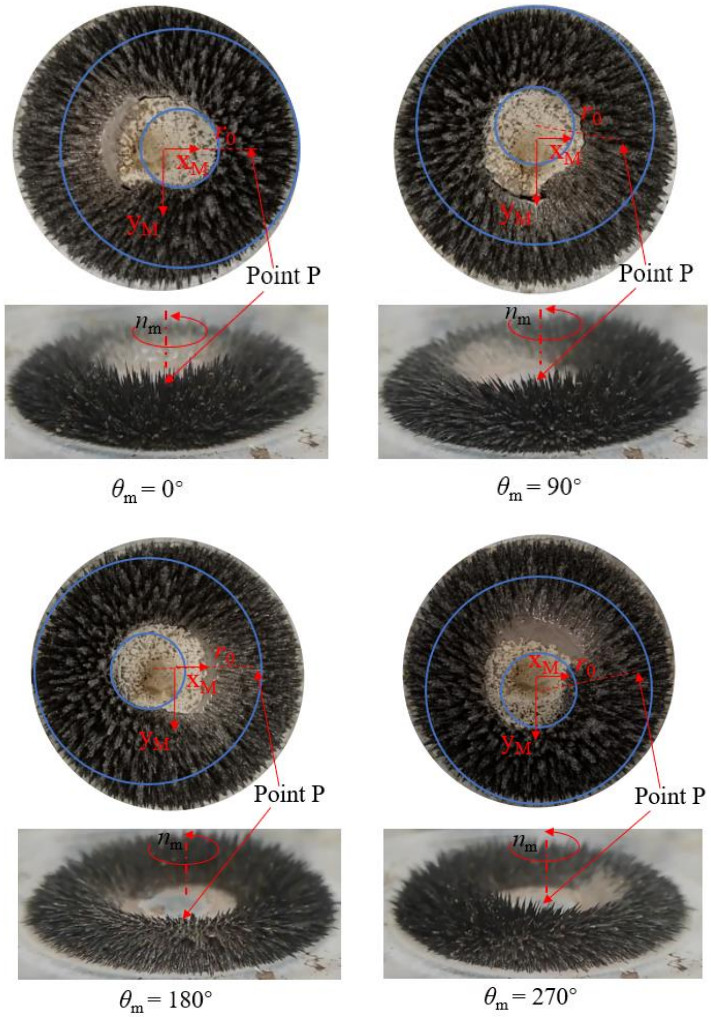

$\theta_m = 0°$ $\theta_m = 90°$ $\theta_m = 180°$ $\theta_m = 270°$

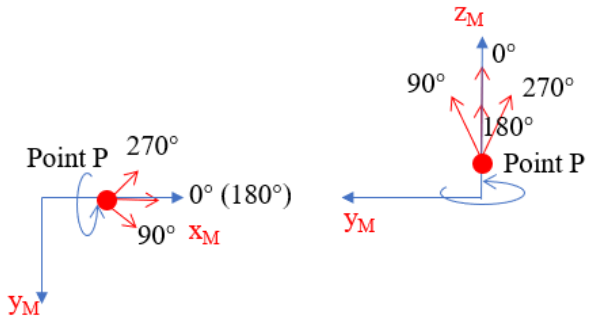

Fig. 3.14. Orientations of clusters at point P with the magnet revolution.

In fact, as the magnet revolved around the axis of MCF carrier, *B* and the orientation of the magnetic line of force at point *Q*' (12.58, 0, 22), i.e., point P, varied continually. This can result in constant variations of the strength and the orientation of ferric clusters. Fig. 3.14 shows the MCF tool with the MCF 2 slurry at different moments during one revolution of the magnet ($\theta_m \in [0°, 360°]$). The conical pendulum motions of the clusters can be obtained from different positions of clusters i.e., $\theta_m = 0°$, 90°, 180°, and 360°, at point P for different moments, indicating that the magnet revolution can alter the orientation of ferric clusters, which contributed to the stir of the particles within the MCF tool.

3.5.4 Behavior of abrasive particles

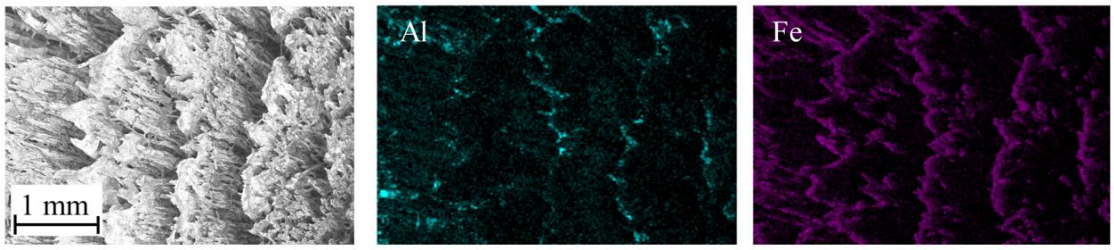

(a) (b) (c)

Fig. 3.15. (a) SEM image of area A. (b) Al and (c) Fe elemental distributions on the top surface of the MCF tool.

In order to observe the distribution of the APs at the upper surface of the MCF sample, the area A at the center of the working area including the portion acting on the point P was selected for observation typically by using an SEM with an EDX mapping function. The

SEM image of area A and EDX mapping results for the distribution of Al and Fe elements in area A are shown in Figs. 3.15(a), (b), and (c), respectively. As shown in the SEM image, many ferric clusters primarily composed of CIPs stood out on the upper surface of the MCF tool, and the EDX mapping results showed that either Al or Fe were distributed well in the entire area A, indicating that the Aps were distributed on the upper surface of the MCF tool. A comparison of the distributions of Al and Fe revealed that the distribution of abrasive particles was also related to the distribution of CIPs on the upper surface of the MCF tool.

As revealed in our previous research [10], the APs within the MCF slurry can always be surrounded by a magnetic medium, mainly under the influence of the magnetic levitation force and gravity. Thus, the APs can squeeze the work-surface at the working gap. However, the direction of the magnetic levitation force was opposite to that of gravity in the current method. Hence, the analysis of the behavior of APs is crucial to the validation of the proposed material removal model. Fig. 3.16 illustrates the forces acting on APs around point P in the B_z direction, where $F_{ap\text{-}z}$ is the magnetic levitation force in the z_M direction and G is the gravitational force. Therefore, the resultant force F is expressed by $F = F_{ap\text{-}z}$ - G. $F > 0$ means that the work-surface is squeezed by the AP at the current position.

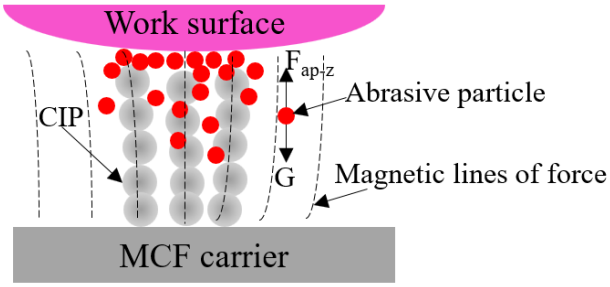

Fig. 3.16. Analysis of the forces acting on APs.

The magnetic levitation force on an AP, $F_{ap\text{-}z}$, can be determined by the magnetic field

strength and magnetic properties of the MCF slurry as follows [11]:

$$F_{\mathrm{ap}-z} = -\mu_0 V_{ap} M \nabla H = -V_{\mathrm{ap}} M_{\mathrm{MCF}} \nabla B_z \qquad (3\text{-}7)$$

where V_{ap} is the volume of the nonmagnetic body, M_{MCF} is the magnetization of the MCF slurry, and ∇B_z is the gradient of the magnetic field. According to the reports by Wang and Guo [12-14], the single AP can be considered spherical. Therefore, the volume of a single AP can be calculated by $V_{\mathrm{ap}} = 4\pi r_{\mathrm{ap}}^3/3$, where r_{ap} is the radius of the AP. Since the variation of magnetization M_{MCF} depends on the applied magnetic field, the fitted *M-B* equations (Eqs. (3-8)-(3-10)) were obtained by using the polynomial fitting method with MATLAB. The experimental results displayed in Fig. 2.11 were used as the input data to be fitted. The results showed that all the determination coefficients (R-squared) were above 0.99, suggesting that the fitted results were accurate and reliable. When $\theta_{\mathrm{m}} = 0°$, the magnetic flux densities B_{z} at points (R, 0, z_{M} = 21.5, 22, 22.5, 23, 23.5, and 24 mm) were simultaneously calculated as shown in Fig. 3.17, in which the gradient command of MATLAB can be directly applied to calculate the ∇B_{z}. It was evident that B_{z} increased with the increase of z_{M} when R was from 9 to 19 mm.

$$M_{MCF1} = -91.526B_z^4 + 423.98B_z^3 - 733.84B_z^2 + 567.81B_z + 0.8949 \text{ (R-squared} = 0.994) \qquad (3\text{-}8)$$

$$M_{MCF2} = -78.428B_z^4 + 364.08B_z^3 - 631.85B_z^2 + 490.27B_z + 0.8855 \text{ (R-squared} = 0.994) \qquad (3\text{-}9)$$

$$M_{MCF3} = -66.167B_z^4 + 307.37B_z^3 - 533.89B_z^2 + 414.46B_z + 0.6458 \text{ (R-squared} = 0.9998) \qquad (3\text{-}10)$$

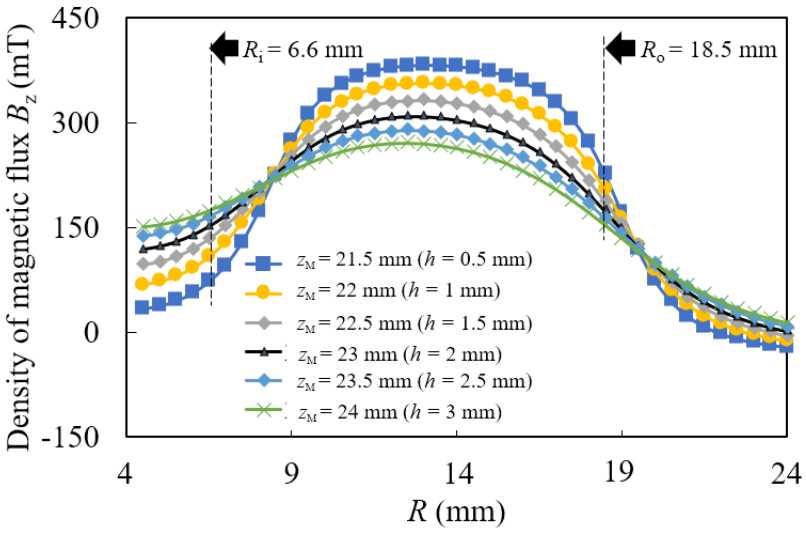

Fig. 3.17. Distribution of B_z at point (R, 0, z_M) when θ_m = 0°.

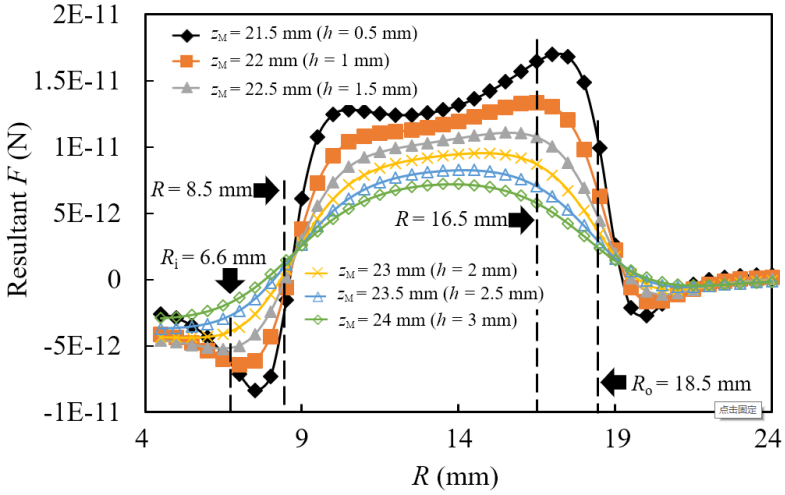

Fig. 3.18. Typical distribution of the resultant F at point (R, 0, z_M) when θ_m = 0°.

The typical distribution of the resultant F along the x_M-axis (θ_m = 0°), for various z_M, i.e., working gap h, is shown in Fig. 3.18. When h =1 mm, the resultant F increased with the increase of R from the inner ring of the MCF tool (R_i) to where R = 16.5 mm, then the resultant F decreased until R reached R_o. It was also found that $F > 0$ for 8.5 mm < R < R_o, indicating that all the APs at these positions can potentially touch the work-surface. However, it can be observed that some points on the work-surface were not squeezed by APs when the magnet was at the initial location, regardless of the given working gap. To find out if a point (R, 0, z_M) has suffered the squeezing of the APs during the entire polishing

process, the following analysis was carried out.

Since the magnet was revolving around the axis of the MCF carrier, i.e., θ_m varied periodically, the resultant F at the point (R, 0, z_M) varied correspondingly. As a result, the resultant F can be expressed as $F = f(\theta_m)$, where θ_m is regarded as the independent variable. θ_m can be determined by $\theta_m = \omega_m t_m = 2\pi n_m t_m$, where $\omega_m = 2\pi n_m$ is the angular velocity of the magnet, and t_m is the revolution time of the magnet. Hence, the resultant F can be then expressed as $F = F(t_m)$. Assuming that the APs can always appear at the work-surface and referring to the calculation process (see Fig. 3.18) where the resultant F at point (R, 0, 22) at $\theta_m = 0°$, i.e., $t_m = 0$ min was calculated, the variations of the resultant F at points (R, 0, 22), where 8.5 mm < R < 16.5 mm with the magnet revolution time t_m, were obtained for one revolution of magnet, i.e., $\theta_m \in [0°, 360°]$ or $t_m \in [0, 0.002]$, as exhibited in Fig. 3.19. As shown in Fig. 3.19, the resultant F at some points can be greater than zero at some moments and less than zero at other moments, suggesting that the corresponding points suffered squeezing from APs at some moments and not at other moments. For different points, the moments with squeezing and without squeezing from APs were different, which was dependent on the relative location of the magnet. Furthermore, the resultant F at different points (R, 0, 22) where 8.5 mm < R < 16.5 mm in an arbitrary moment t_m, i.e., $F = F(t_m)$, can be obtained by fitting the data in Fig. 3.19 and using Eqs. (3-11)-(3-15) where $1/n_m$ is the time for one complete magnet revolution. The determination coefficients (R-squared) of the results were all beyond 0.99, indicating that the proposed model can provide accurate and reliable results. The average resultant F in one revolution of the magnet can be given by Eq. (3-16).

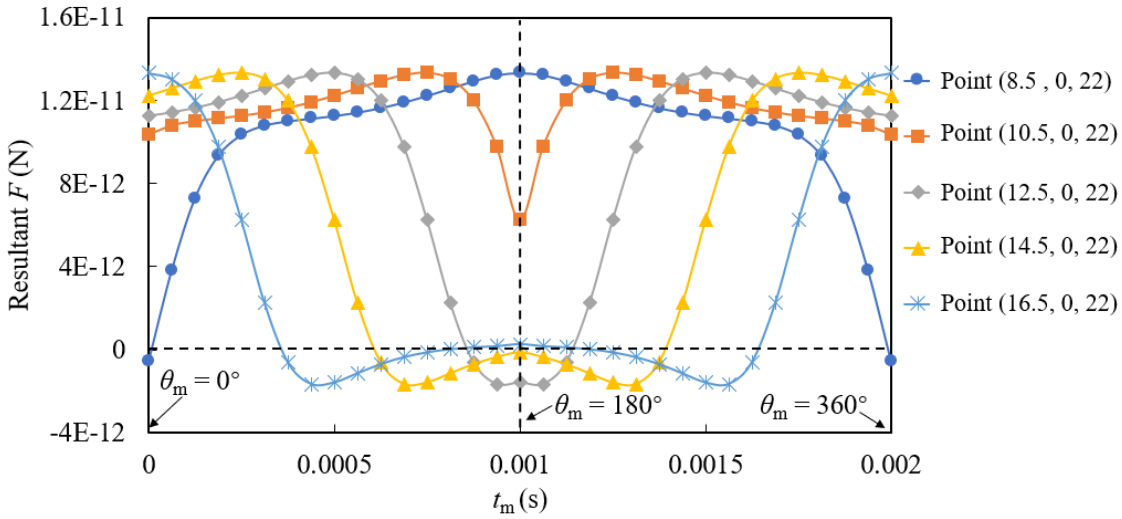

Fig. 3.19 The variations of the resultant F at points (R, 0, 22) during one revolution of the magnet.

$$F(t_m)_{R=8.5} = \begin{cases} \text{-6.5688}t_m^4 + 0.033t_m^3 - \text{6E-05}t_m^2 + \\ \text{4E-8}t_m - \text{6E-13 (R-squared} = 0.9988) \ 0 \leq t_m < 1/2n_m \\ \text{-105.1}t_m^4 + 0.577t_m^3 - \text{1.2E-03}t_m^2 + \\ \text{1E-6}t_m - \text{3E-10 (R-squared} = 0.9988) \ 1/2n_m \leq t_m < 1/n_m \end{cases} \quad (3\text{-}11)$$

$$F(t_m)_{R=10.5} = \begin{cases} \text{-5.9344}t_m^4 + 0.0183t_m^3\text{-2E-05}t_m^2 + \\ \text{7E-9}t_m + \text{1E-11 (R-squared} = 0.9955) \ 0 \leq t_m < 1/2n_m \\ \text{-94.951}t_m^4 + 0.6133t_m^3 - \text{1.5E-03}t_m^2 + \\ \text{2E-6}t_m - \text{6E-10 (R-squared} = 0.9955) \ 1/2n_m \leq t_m < 1/n_m \end{cases} \quad (3\text{-}12)$$

$$F(t_m)_{R=12.5} = \begin{cases} 15678t_m^5 - 66.147t_m^4 + 0.0875t_m^3 - \text{4E-05}t_m^2 \\ + \text{9E-9}t_m + \text{1E-11 (R-squared} = 0.997) \ 0 \leq t_m < 1/2n_m \\ -501704t_m^4 + 3958.7t_m^3 - 12.301t_m^2 + 0.0188t_m \\ - \text{1E-05}t_m + \text{4E-09 (R-squared} = 0.997) \ 1/2n_m \leq t_m < 1/n_m \end{cases} \quad (3\text{-}13)$$

$$F(t_m)_{R=14.5} = \begin{cases} \text{-22922}t_m^5 + 114.54t_m^4 - 0.1874t_m^3 + \text{1E-4}t_m^2 \\ + \text{2E-8}t_m + \text{1E-11 (R-squared} = 0.9935) \ 0 \leq t_m < 1/2n_m \\ 733519t_m^4 - 5502.6t_m^3 + 16.181t_m^2 - 0.0233t_m \\ + \text{2E-05}t_m + \text{5E-09 (R-squared} = 0.9935) \ 1/2n_m \leq t_m < 1/n_m \end{cases} \quad (3\text{-}14)$$

$$F(t_m)_{R=16.5} = \begin{cases} 16330t_m^5 - 94.606t_m^4 + 0.1936t_m^3 - \text{2E-4}t_m^2 \\ + \text{3E-8}t_m + \text{1E-11 (R-squared} = 0.9928) \ 0 \leq t_m < 1/2n_m \\ -522575t_m^4 + 3715.1t_m^3 + 10.342t_m^2 + 0.0141t_m \\ - \text{1E-05}t_m + \text{3E-09 (R-squared} = 0.9928) \ 1/2n_m \leq t_m < 1/n_m \end{cases} \quad (3\text{-}15)$$

$$F_{average} = \frac{\int_0^{tm} F(t_m)dt_m}{1/n_m} \quad (3\text{-}16)$$

To assess the degree of the APs squeezing in one magnet revolution at points along the radius of the MCF tool, the average resultant F, $F_{average}$, was calculated using Eq. (3-16). In the calculation process, the resultant F was set at 0 for negative values since there were no

squeezing happened. In this way, $F_{average}$ at points (R, 0, z_M) (8.5 mm < R < 16.5 mm, 21.5 mm < z_M < 24 mm) were obtained as displayed in Fig. 3.20.

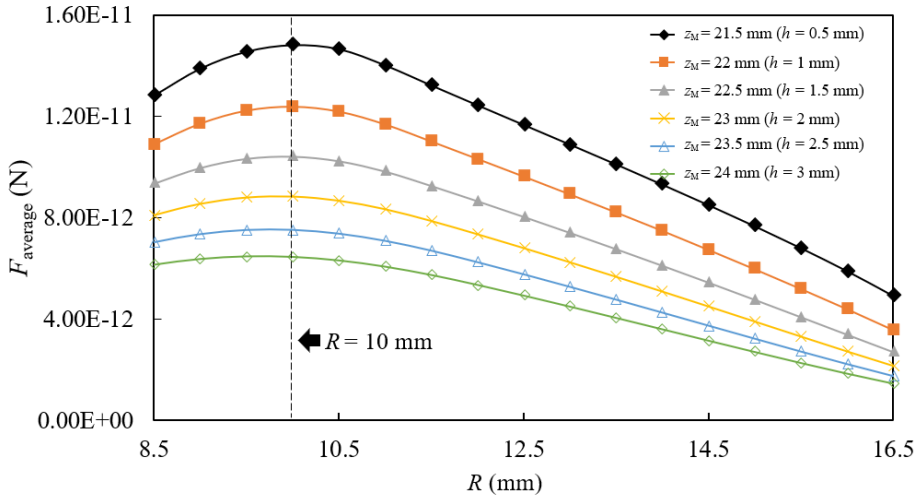

Fig. 3.20. Distribution of $F_{average}$ along the radius of the MCF tool at different z_M.

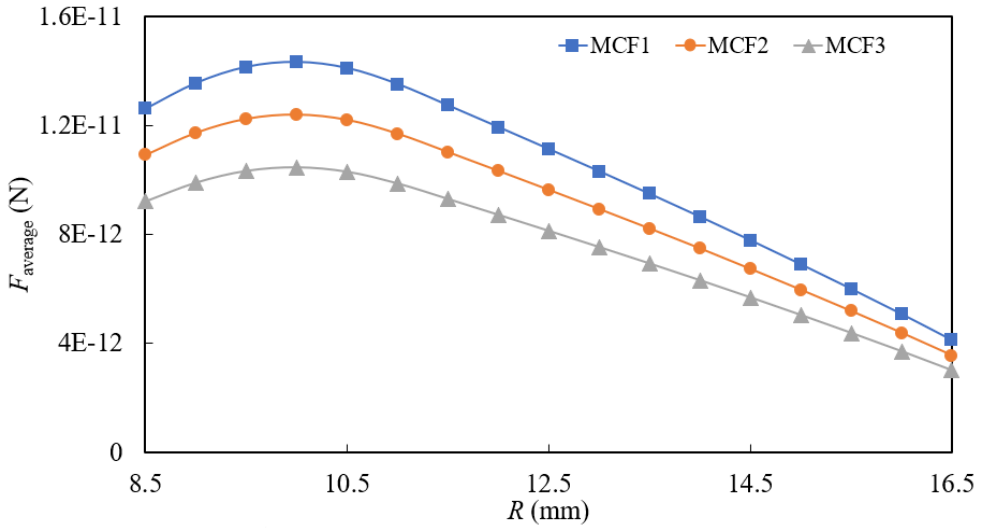

Fig. 3.21. Distribution of $F_{average}$ along the radius of the MCF tool at z_M = 22 with different MCF slurries.

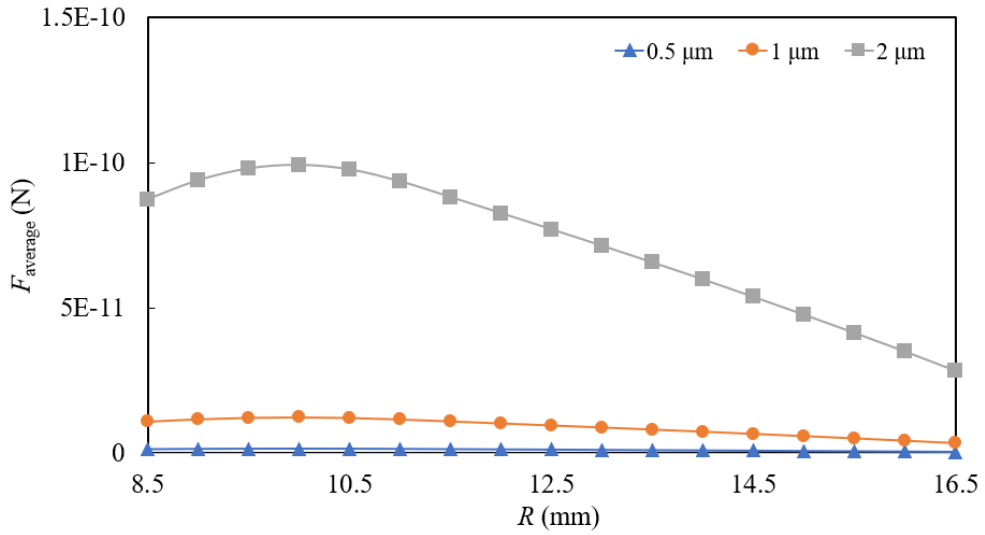

Fig. 3.22. Distribution of $F_{average}$ along the radius of the MCF tool at z_M = 22 for APs with different sizes.

As shown in Fig. 3.20, $F_{average}$ was observed to be greater than zero, indicating that the work-surface can always be squeezed by the APs as the magnet revolved, regardless of the working gap. Moreover, $F_{average}$ increased first when R increased from the inner ring to R = 10 mm, after which $F_{average}$ began to decrease as R increased to the outer ring, regardless of the working gap. Additionally, as mentioned above, the APs, as initially located in the large working gap, were compressed to the smaller working gap, where the effect of the magnet field was more evident, resulting in the increase in polishing forces. Therefore, the more the MCF tool was compressed, the higher material removal ability became.

As illustrated in Fig. 3.21, when MCF1-3 slurries were applied, $F_{average}$ increased with the increase of the CIPs concentration, i.e., increased magnetization M_{MCF}. The variations of $F_{average}$ with different sizes of the APs are displayed in Fig. 3.22. The results showed that $F_{average}$ increased with the increase of APs sizes. Figs. 3.21 and 3.22 demonstrate that higher material removal ability can be obtained when larger APs and higher CIPs concentration

were used within MCF tool.

Additionally, the shear stress of the MCF slurry was strongly related to the magnetic field strength and the CIPs concentration. Therefore, the induced tangential forces of the APs, which acted on work-material, increased when the APs were closer to the upper surface of the magnet and when the MCF slurry was used with a higher concentration of CIPs. In these situations, the material removal ability can be enhanced significantly.

3.6 Model of material removal

Based on the experimental results and theoretical analysis above, a reasonable material removal model of the proposed method is proposed as shown in Fig. 3.23.

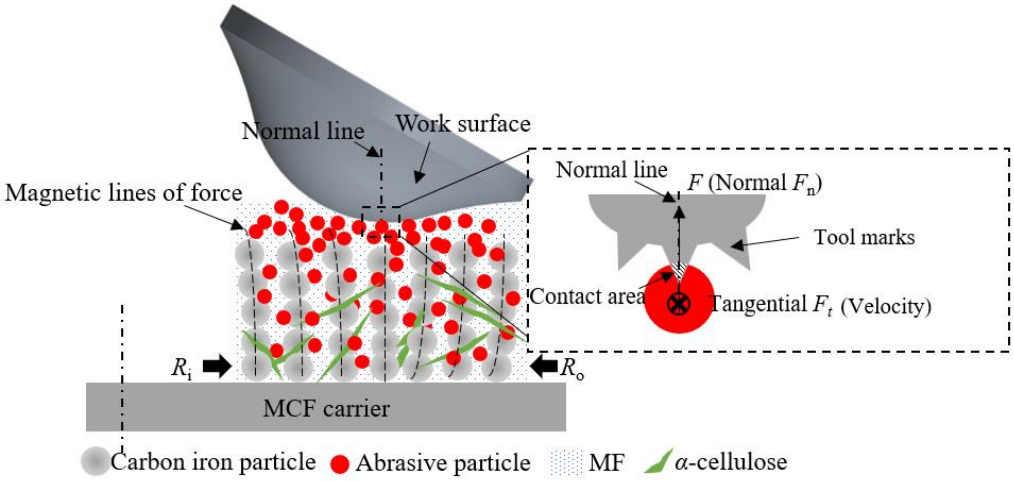

Fig. 3.23. Model of material removal.

Ferric particles gather along the magnetic line of force to form chain-shaped clusters, APs become entrapped or attached to the surfaces of the clusters, and the α-celluloses intersperse in the clusters to improve the cluster toughness. Due to the compression of the MCF tool, some APs are forced to move downwards to the given working gap, and these APs are affected strongly by the magnetic field and squeeze the work-surface under the action of the magnetic levitation force and gravity. The resultant force F acting on an AP is

always vertical to the surface of the MCF carrier. Thus, it overlaps the normal line of point P, and the normal force acting on work-surface can be regarded as the resultant F. Once the relative motion between the MCF tool and the workpiece is given, the shear stress i.e., the tangential force, is thereby generated. Under the combined function of the normal/tangential forces and the velocity, the work-material is removed by the micro-cutting action of the APs. Moreover, under the rotary magnetic field, the ferric clusters change their orientations with the magnetic line of force, which contributes to the stirring the abrasive particles and refreshing of their cutting edges to maintain the polishing performance.

Summary

(1) The formation process of the MCF tool was affected by the eccentricity r_e, the rotation speed of the MCF carrier n_c, the revolution speed of the magnet n_m, and the amount of MCF slurry supplied V. Apart from the revolution speed of the magnet n_m, above parameters also affect significantly the geometry of the MCF tool.

(2) A perfect MCF tool could be obtained when the eccentricity r_e, the rotation speed of the MCF carrier n_c, the revolution speed of the magnet n_m, and the amount of MCF slurry supplied V were 4 mm, 300 rpm, 500 rpm, and 1.5 ml, respectively, resulting in a MCF tool with dimensions of a = 14.50 mm, b = 12.10 mm, c_1 = 0.12 mm, c_2 = 0.71 mm, d_o = 37 mm, and H = 5.00 mm.

(3) The CIPs were gathered to form the ferric clusters along the magnetic flux lines.

(4) The Aps, at a given working gap, can squeeze the work-surface. The squeezing action was much more intense when larger APs and the MCF slurry with a higher

magnetization were employed.

(5) The material removal model suggested that the material was removed due to the APs and the relative motion between the work-surface and APs.

References

[1] Shimada K, Wu Y, Matsuo Y, Yamamoto K. Float polishing technique using new tool consisting of micro magnetic clusters. Journal of Materials Processing Technology. 2005;162:690-5.

[2] Wu Y, Shimada K, Wong YC. Fundamental performance of magnetic compound fluid (MCF) polishing tool in metal surface finishing. International Journal of Machining & Machinability of Materials. 2009;5:232.

[3] Sato T, Wu YB, Lin WM, Shimada K. Study of Three-Dimensional Polishing Using Magnetic Compound Fluid (MCF). Advanced Materials Research. 2009;76-78:288-93.

[4] Feng M. Nano-precision polishing of aspherical surfaces with doughnut-shaped MCF (Magnetic Compound Fluid) polishing tool. 2017.

[5] Feng M, Wu YB. Fundamental Investigation on the Polishing Aspheric Elements with Doughnut-Shaped MCF Slurry. Key Eng Mater. 2018;792:179-84.

[6] Feng M, Wu YB, Youliang Wang, Bitoh T, et al. Investigation on the polishing of aspheric surface with a doughnut-shaped magnetic compound fluid tool [J]. Precision Engineering.

[7] Wang D. Effect of particle size and temperature on magnetization properties of carbonyl iron powder. Function materials. 2014;45:6-9.

[8] Shimada K, Wu Y, Wong YC. Effect of magnetic cluster and magnetic field on polishing using magnetic compound fluid (MCF). J Magn Magn Mater. 2003;262:242-7.

[9] Jiao L, Wu Y, Wang X, Guo H, Liang Z. Fundamental performance of Magnetic Compound Fluid (MCF) wheel in ultra-fine surface finishing of optical glass. International Journal of Machine Tools and Manufacture. 2013;75:109-18.

[10] Wang RK, Zuo HF, Meng LV. Analytical Calculation and Simulation for Magnetic Field Distribution of Ring Magnet. Aeronautical Computing Technique. 2011.

[11] Guo H, Yongbo Wu, Jiao L, Cao J, Yaguo LI. Ultrafine Polishing of Nickel Phosphorus Plating with Magnetic Compound Fluid Slurry. Journal of Mechanical Engineering. 2013;49:73.

[12] Wang Y, Wu Y, Nomura M. Feasibility study on surface finishing of miniature V-grooves with magnetic compound fluid slurry. Precis Eng. 2016;45:67-78.

[13] Wang Y, Wu Y, Nomura M. Fundamental investigation on nano-precision surface finishing of electroless Ni–P-plated STAVAX steel using magnetic compound fluid slurry. Precis Eng. 2017;48:32-44.

[14] Sidpara AM, Jain VK. Nanofinishing of freeform surfaces of prosthetic knee joint implant. Proceedings of the Institution of Mechanical Engineers, Part B: Journal of Engineering Manufacture. 2012;226:1833-46.

Chapter Ⅳ Evolution and Equivalent Control Law of Surface Roughness

4.1 Introduction

Magnetic-field-assisted polishing has been recognized as a promising finishing technique [1], which can obtain a mirror surface with better surface quality than conventional methods. Many representative magnetic-field-assisted polishing processes were invented over the past years, such as MAF (magnetic abrasive finishing), MRFF (magnetorheological fluid-based finishing), MRAFF (magnetorheological abrasive flow finishing), MRJF (magnetorheological jet finishing), BEMRF (ball end magnetorheological finishing). Magnetic abrasive finishing (MAF) improved the surface roughness of an HRC55 workpiece from Ra 0.25 to 0.05 μm within 10 min [2]. A variety of materials ranging from optical glasses to hard crystals was been polished successfully by MRFF process to sub-nanometer scale [3]. Workpieces with internal surfaces were finished by MRAFF (magnetorheological abrasive flow finishing) process [4]. MR jet finishing was developed for finishing of cavities, steep concave and dome optics surfaces [5]. BEMRF (ball end magnetorheological finishing) [6] process was invented for finishing the flat or 3D complex surfaces. It was obvious that magnetorheological (MR) finishing based techniques have been widely used for polishing workpiece surfaces with promising removal efficiency [7]. However, the MRF slurry used by magnetorheological (MR) finishing based techniques has poor dispersity of particles, which is unfavorable for nano

precision surface finishing. To overcome the disadvantages of MRF slurry, the magnetic compound fluid (MCF) slurry was developed by Shimada et al. [8]. Due to the disadvantages of the mount-shaped MCF tool on polishing aspheric surfaces, and inspired by the works of Guo and Jiao, a ring-shaped magnet was consequently employed to replace the disk-shaped magnet to form the doughnut-shaped MCF tool in our previous chapters.

The formation process was experimentally investigated, the MCF tool with proper appearance was obtained by appropriately selecting the process parameters, i.e., the rotation speed of MCF carrier, the revolution speed and the eccentricity of the magnet, and the volume of MCF slurry supplied, the effect of the components of MCF slurry on the polishing was investigated. The material removal mechanism was still unclarified in detail for explaining the evolution process of the surface roughness. It was concluded in Guo's work that surface was smoothed due to the polishing forces, namely the normal force and tangential force, and the tangential force contributed more to the removal of material rather than normal force during surface polishing. In order to clarify the reduction rules in surface roughness, Kansal simulated the polishing forces by establishing the indentation model of the single abrasive particle where the magnetic levitation force acting on APs was considered as the indentation force, i.e., normal force, and the normal force was the resultant force of shear force acting on APs and the resistant force of the material, and concluded that surface was smoothed only when the shear force was larger than the resistant force [9]. Thus, the polishing forces were one of the most important factors for understanding clearly on surface finishing.

Towards the development of the novel polishing method with the doughnut-shaped MCF

tool, the material removal mechanism of the novel polishing tool is further studied systematically in this chapter. Firstly, the experimental detail is described. Secondly, the model of polishing forces is established based on the indentation model of the single abrasive particle, and the simulation in the surface roughness is conducted for predicting the polishing results. Thirdly, the polishing experiments are given out to confirm the theoretical analysis.

4.2 Experimental details

Table 4.1. Experimental conditions

Parameter	Values
n_c	300 rpm
n_m	500 rpm
n_w	4000, 700, 1000 rpm

To experimentally study the evolution and equivalent control law of surface roughness with the novel polishing tool, experiments were carried out. The conic surface was polished to verify the simulation results in surface roughness. The revolution speed of the workpiece n_w was crucial for investigating the variation rules of the polishing forces and the induced surface roughness, in order to conveniently applying to the industry. Thus, the revolution speed of the workpiece n_w was set at 400 rpm, 700 rpm, and 1000 rpm for the rest of the work.

4.3 Kinematic analysis

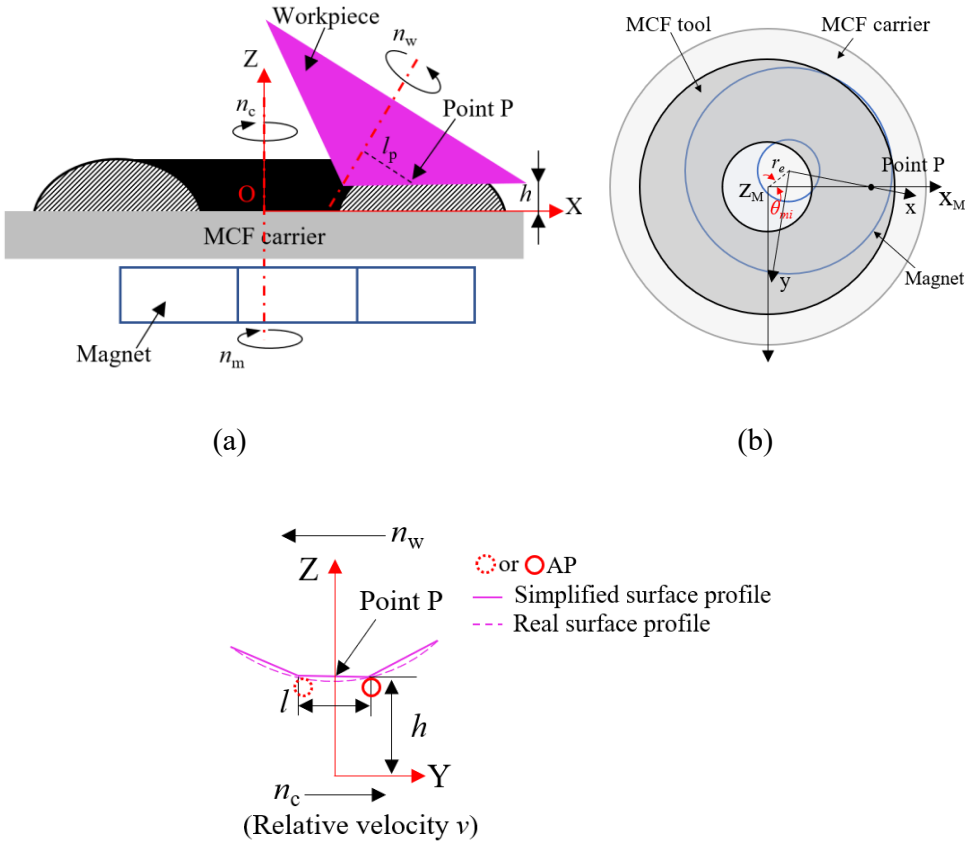

Fig. 4.1 Schematic for kinematic analysis during polishing: (a) relative arrangement of the workpiece to MCF tool, (b) the relative location of the magnet to point P at i^{th} revolution of workpiece, (c) relative motion of MCF tool to point P.

As shown in Fig. 4.1(a), the relative arrangement of the workpiece to MCF tool is displayed where the point P is polished by the middle portion of the MCF tool with an h of working gap. The relative location of the magnet to point P at i^{th} revolution of workpiece is pictured in Fig. 4.2(b). Initially, the magnet is located below point P with $\theta_{m0} = 0°$, then point P and the magnet revolve in n_w and n_m, respectively. When point P arrives again at the initial location after i^{th} revolutions, the magnet stops at θ_{mi}. The time assumption for i^{th} revolutions of point P is $t = i^{th}/n_w$, so that θ_{mi} is obtained by $\theta_{mi} = \omega_m t = 2\pi n_m t$, where θ_{mi}

$\in$ (0, 2π). As shown in Fig. 4.1(c), the surface curves of the workpiece are simplified to be composited by many short lines with an l in length and each line represents a point on the work surface. Therefore, the polishing process of point P in one revolution of workpiece can be assumed that a single AP move alongside the surface profile to remove the material with the relative velocity v of the MCF tool to point P, from the left (location of the dashed circle) to the right (location of the solid circle). The polishing process occurs consecutively as point P arrives again at its initial location after one revolution.

The relative velocity v of the point P to the MCF tool can be obtained by

$$v = \omega_c R_P - \omega_w l_P \quad (4\text{-}1)$$

where ω_c is the angular velocity of the MCF carrier, thus $\omega_c = 2\pi n_c$, R_P is the distance of point P to the revolution center of the MCF tool, ω_w is the angular velocity of the workpiece, thus $\omega_w = 2\pi n_w$. l_P is the rotary radius of point P, thus $l_P = R_P \sin\alpha$.With the relative velocity v, the shear rate $\dot{r}$ at point P is thereby obtained by

$$\dot{r} = \frac{v}{h} \quad (4\text{-}2)$$

4.4 Indentation model

In doughnut-shaped MCF tool, the indentation of a single abrasive particle into the surface of workpiece attributes to the normal force applied on it due to the squeezing of the AP which was demonstrated in detail in chapter 3. The following assumptions are adopted for modeling of forces during polishing process:

- All APs have the same size and are spherical in shape.
- Only abrasive particles contact with workpiece surface and they are assumed uniformly distributed within the MCF tool.

- Because the amount of the removed material is low throughout the whole polishing process, the impact of the removed material mixed with MCF slurry on the properties of MCF tool, including magnetic field distribution, rheological behavior of the MCF slurry, and mechanism, is negligible.

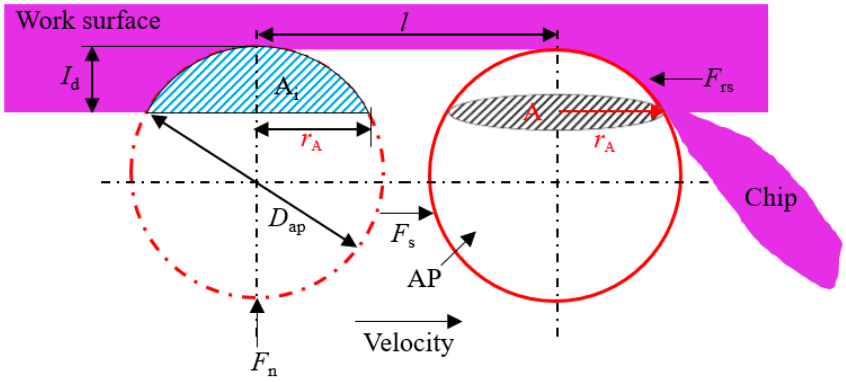

Fig. 4.2. Indentation model of the single abrasive particle.

To get an insight into the reasons for variation in the reduction in surface roughness Ra in this novel method, it is required to develop a mathematical model to predict the forces acting on abrasive particles during processing. As demonstrated in chapter 3, the APs can squeeze the work surface due to the resultant force F, i.e., normal force F_n, owning to the magnetic levitation force and gravitational force, and the tangential force on the work surface was contributed by the rheological behavior of the MCF slurry and the resistant force of work material. Based on these results, the indentation model of the single abrasive particle in an arbitrary revolution is established, as shown in Fig. 4.2, where D_{ap} is the diameter of a single AP, I_d is the induced indentation depth, A_i is the cross-section of the induced indentation, A is projection area of the induced indentation to the work surface along the direction of F_n, r_A is the radius of A, F_s is the shear force induced by the rheological behavior of the MCF slurry, F_{rs} is the resistant force of the work surface, and l

is the length of the trace of the AP.

If abrasive particles contact with the work surface, workpiece material will produce elastic deformation, elastic-plastic deformation and plastic deformation as polishing pressure and shear force caused by abrasive particles are different. The indentation depth depends on normal force F_n of particles and material physical or chemical properties. When the cutting depth is very small, work surface can only produce elastic and elastic-plastic deformation, at this time, material cannot be removed. When the cutting depth reaches a certain value, work surface can produce plastic deformation and indentation caused by action of abrasive, then material can be removed. The material removal process of the novel method at point P can be depicted as follows:

In i^{th} revolution of point P, the magnet stops with θ_{mi}. The AP is indented into the work surface with an I_d of depth due to the external indentation force F_n acting on AP. Once the relative velocity v is applied to the AP and work surface, the shear force F_s is induced and AP will be pushed to go forward if F_s is powerful than the resistant force F_{rs}, the resultant force generated by shear force F_s and resistant force F_{rs} is namely the tangential force F_t, which leads the chip generated and finally cut off from work surface during the AP.

The magnetic levitation force on an abrasive particle is determined by the magnetic field strength and magnetic properties of the MCF slurry. The magnetic levitation force $F_{ab\text{-}z}$ is expressed as Eq. 3 [10]:

$$F_{ap-z} = -V_{ap} M_{MCF} \nabla B_z \qquad (3)$$

where V_{ap} is the volume of the nonmagnetic body, M_{MCF} is the magnetization of the MCF slurry, and ∇B_z is the gradient of the magnetic field. If the magnetic field is strong

enough, the AP is always suspending inside the MCF tool without attaching the clusters although it squeezes the work surface. However, it was found that abundant APs were attaching to the clusters inside the MCF tool in our previous works, because the counter-acting force of the work surface to the APs when APs indented into the work surface made the APs to squeeze the CIPs. In other words, the CIPs have to support the energy for APs to indent into the work surface. Therefore, the magnetic attraction force acting on the CIP will be also considered in this work. The magnetic attraction force acting on a CIP for supporting the AP can be obtained by Eq. 4 [11]:

$$F_{\mathrm{CIP}-z} = -mM_{\mathrm{CIP}}\nabla B_z \quad (4)$$

where m is the mass of the magnetic body, M_{CIP} is the magnetization of the CIPs. So far, the normal force F_{n} acting on work surface in this work can be obtained by Eq. 5.

$$F_{\mathrm{n}} = F_{\mathrm{ap}-z} + F_{\mathrm{CIP}-z} - G \quad (5)$$

According to the relationship in geometry between I_{d}, D_{ap}, and r_{A} (Eq. (4-3)), the depth of the indentation I_{d} is thereby obtained [12].

$$I_d = \frac{1}{2}\left(D_{ap} - \sqrt{D_{ap}^2 - 4r_A^2}\right) \quad (4\text{-}3)$$

The Brinell hardness number (BHN) proposed by Swedish engineer Johan August Brinell in 1900, it was the first widely used and standardized hardness test in engineering and metallurgy. BHN is designated by the most commonly used test standards (i.e. conforming to standard ASTME10-12 and ISO6506-1:2005) as HBW (H represents hardness, B represents Brinell and W represents the material of the indenter, tungsten (wolfram) carbide). H_{HBW} of the workpiece can be correlated for the depth of indentation as follows:

$$H_{HBW} = \frac{1}{g}\frac{2F_n}{\pi D_{ap}(D_{ap}-\sqrt{D_{ap}^2-4r_A^2})} \quad (4\text{-}4)$$

where g is the acceleration due to gravity and equal to 10 m/s^2. The hardness of the workpiece is measured by micro-hardness testing machine. r_A is calculated by substituting the workpiece hardness value and normal force F_n. The normal force F_n was obtained by referring to the method used in investigating the behavior of abrasive particles in chapter 3. Al6061 is used for the work material throughout the work, so the H_{HBW} of the work material was around 120 HBW. Thus, by comparing Eqs. (4-3) with Eq. (4-4) and being simplified, I_d can be resolved.

The cross-sectional area A' and the projection area A of the contact area are derived from the followings:

$$A' = \frac{D_{ap}^2}{4}\arcsin\frac{2\sqrt{I_d(D_{ap}-I_d)}}{D_{ap}} - (\frac{D_{ap}}{2}-I_d)\sqrt{I_d(D_{ap}-I_d)} \quad (4\text{-}5)$$

$$A = \pi r_A^2 \quad (4\text{-}6)$$

Consequently, the shear force F_s and the resistant force F_{rs} are derived by Eqs. (4-7) and (4-8), where σ_w denotes the yield strength of the material to be finished and is measured by the hardness meter. Based on the analysis above, the tangential force F_t can be obtained by Eq. (4-9). The shear force F_s was determined by the shear stress τ of the MCF slurry which was related to the magnetic flux density B and the shear rate $\dot{r}$, the results about the rheological behavior of the MCF slurry in chapter 2 was employed for resolving the shear force F_s. For obtaining the resistant force F_{rs}, the shear yield stress of workpiece surface σ_w should be measured by the hardness meter. However, when $F_s \leq F_{rs}$, i.e., F_t is negative, meaning that the material is unable to be removed, in the case of which, A' is expressed by Eq. (4-10) for judging this situation during simulation.

$$F_s = \tau(A - A') \quad (4\text{-}7)$$

$$F_{rs} = \sigma_w A' \quad (4\text{-}8)$$

$$F_t = F_s - F_{rs} \quad (4\text{-}9)$$

$$A' \geq \frac{A\tau}{\sigma_w + \tau} \quad (4\text{-}10)$$

4.5 Prediction model of surface roughness

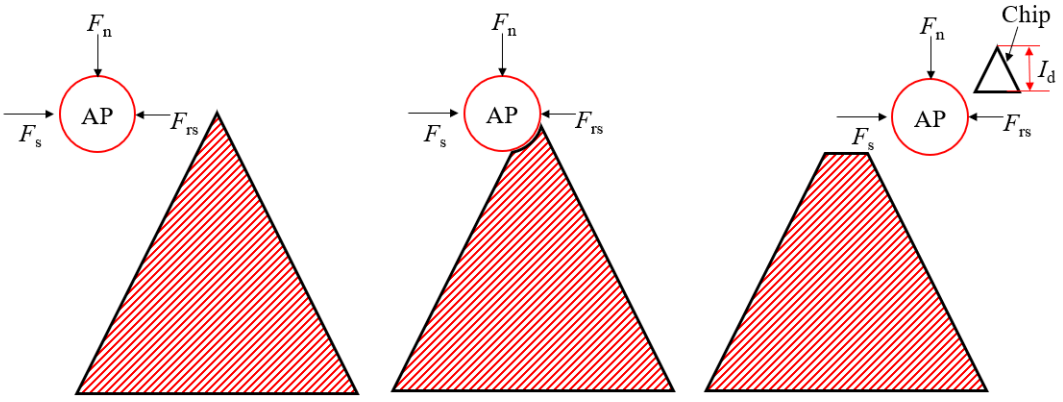

(a)

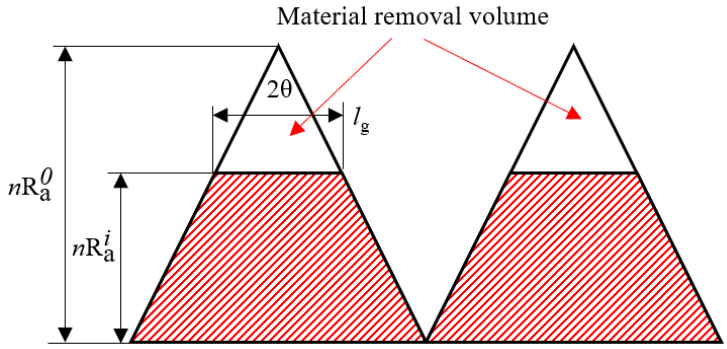

(b)

Fig. 4.3 Typical theoretical model of surface roughness: (a) material removal process of a peak by the single AP on the roughness profile, (b) surface roughness model.

The typical theoretical model of surface roughness is illustrated in Fig. 4.3. The peak of the initial roughness profile on the work surface is considered as a triangle with 2θ of vertex angle [13]. The peaks on the work surface have the priority to contact with APs than valleys. As shown in Fig. 4.3(a), the removal process of the peak by the single AP is given out. The

AP forced initially by the forces tries to shear the material off from the peak ((in the left of Fig. 4.3(a)), and then AP is cutting the material off (in the middle of Fig. 4.3(a)), the removal process is finished when the chip with an I_d of height is dropped from the work surface (in the right of Fig. 4.3(a)). This removal process of material is repeated continuously during the whole polishing process.

The initial work surface is assumed to be the triangular profile with the surface roughness Ra, as shown in Fig. 4.3(b). The peaks are uniformly distributed at initial surface roughness and partially sheared off from the surface profile in each cycle. Along the direction of the abrasive particle, it can be calculated that the volume of material removed by a single abrasive grain, M_{Vp}, is given by

$$M_{\mathrm{Vp}} = A'(1 - \frac{R_a^i}{R_a^0})l \quad (4\text{-}11)$$

The total numbers of the active APs in per revolution is N_p. Thus, the total volume of the removed material M_v in i^{th} revolution should be $M_v = N_p M_{vp}$. According to the geometry arrangement in Fig. 7, M_V can be also written as follows:

$$M_{\mathrm{V}} = (1 - \frac{R_a^i}{R_a^0})l\,(nR_a^{i-1} - nR_a^i)r_A \quad (4\text{-}12)$$

In terms of comparing Eq. 4-11 with Eq. 4-12, then being simplified, we obtain the equality as follows:

$$nR_a^i = \left|nR_a^{i-1} - \frac{N_P A'}{r_A}\right| \quad (4\text{-}13)$$

4.6 Results and discussion

4.6.1 Polishing forces

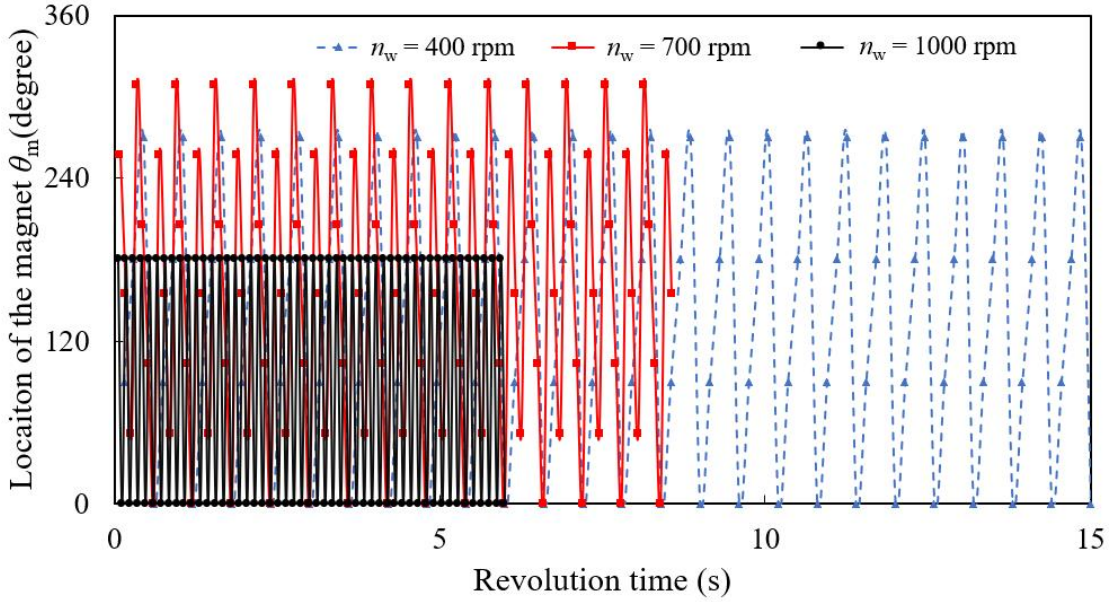

Fig. 4.4 Typical variation of the magnet location θ_{mi} with revolution time t.

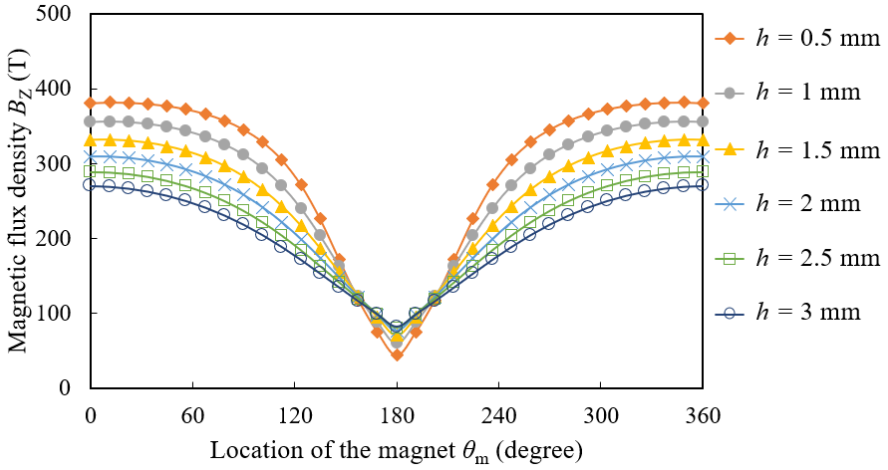

Fig. 4.5 Variation of magnet flux density B_z with the magnet location θ_m in an arbitrary revolution.

Within 100 revolutions, the typical variation of the magnet location θ_{mi} with revolution time t is illustrated in Fig. 4.4 when n_m = 500 rpm and n_c = 300 rpm. It was found that the location of the magnet changed with an obvious rule in which the magnet stopped at different locations within the first some revolutions, and then the locations of the magnet

were repeated continuously in the following revolutions. When working gap h ranges from 0.5 to 3 mm, the variation of magnetic flux density B_z with the magnet location θ_m in an arbitrary revolution is shown in Fig. 4.5. It was obvious that the magnetic flux density B_z gradually decreased when the magnet revolved from $\theta_m = 0°$ to $\theta_m = 180°$, then it increased when the magnet returned to the initial location, and when $\theta_m = 180°$ was selected as the symmetry axis, the curve was totally symmetric. In the case of the given conditions, the shear rate $\dot{r}$ = 425.1, 450.6, 475.8 1/s were calculated by Eq. (4-2), respectively. When the θ_{mi} was determined, the normal force F_n acting on the point P at the i^{th} revolution was obtained, referring the mentioned method, and the shear force F_s acting on the point P at the i^{th} revolution was obtained by giving the shear stress τ which was obtained by substituting magnetic flux density B_Z and shear rate $\dot{r}$ into Eq. (2-1). Al6061 is used for the work material throughout the work, the hardness of the work material H_{HBW} and the yield strength of the material σ_w was nearly 120 HBW and 220 MPa, respectively. So far, substituting the parameters into equations mentioned above, the polishing forces were resolved follows:

Within 100 revolutions, the variation of normal force F_n with the revolution time t is displayed in Fig. 4.6 when D_{ap} = 1 μm. Apparently, the normal force F_n varied as the same tendency with the location of the magnet. Smaller difference and value of the normal forces is found when n_w = 1000 rpm, rather than others. Moreover, the variation of tangential force F_t with revolution time t is illustrated in Fig. 4.7, the tangential force F_t also performed the same tendency with the location of the magnet. Higher values and smaller deviation are observed when n_w = 700 rpm. It is evident that all the polishing forces, i.e., F_n and F_t, are

larger than zero, meaning that material is capable of being removed under these conditions.

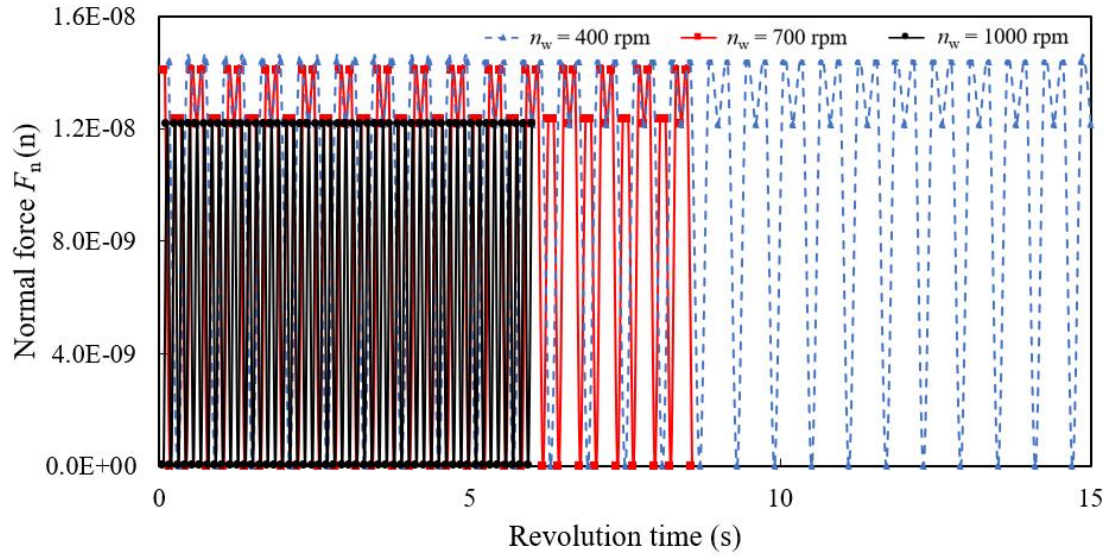

Fig. 4.6 Variation of normal force F_n with the revolution time t.

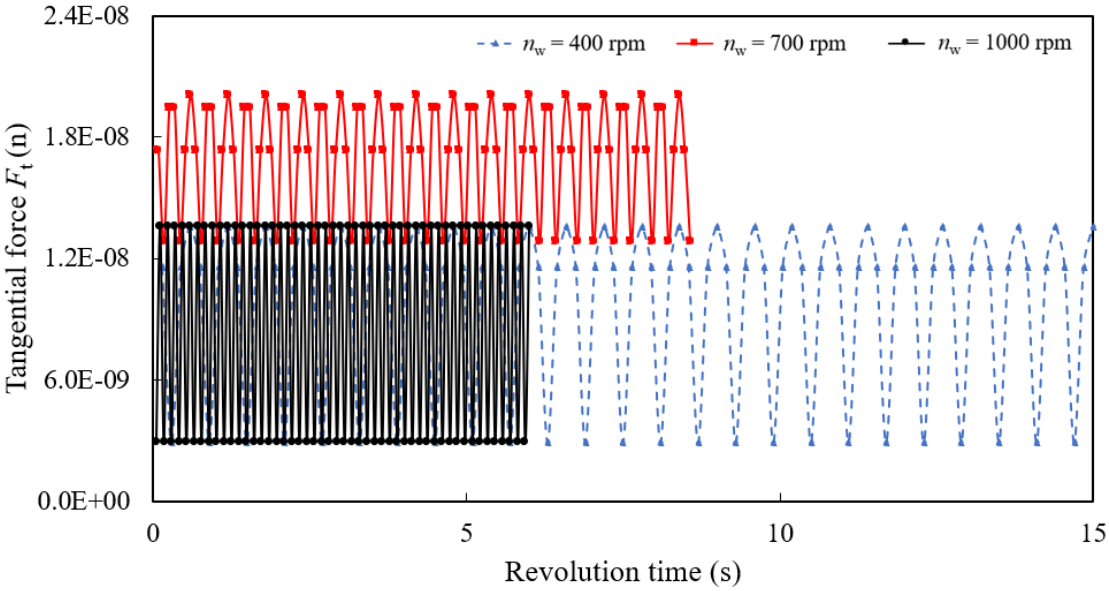

Fig. 4.7 Variation of tangential force F_t with revolution time t.

4.6.2 Surface roughness

As mentioned above, surface roughness Ra is one of the key factors for evaluating the performance of the proposed process. It is necessary to verify the predication model by comparing the experimental results with the predicted values. Considering the revolution speed of the workpiece is more adjustable conveniently than other

parameters when applying the method to industry, the experiments and simulations were thereby carried out with variable revolution speeds of the workpiece, n_w. In the simulations, only one abrasive particle is counted to take participate into cutting, because the point P suffers point-contact with the MCF tool in reality. The initial surface roughness Ra and ratio n are 89 nm and 2, respectively. The experimental and simulated surface roughness Ra after polishing for 60 min are shown in Fig. 4.7. It is found in the simulated results that the surface roughness Ra decreases with the increase in the revolution speed of the workpiece. However, the surface roughness Ra at n_w = 1000 rpm slightly increases than n_w = 700 rpm in experiments. This is not only because of the difference in theoretical polishing forces, but also because that higher revolution speed of the workpiece splits more MF out from the MCF tool and the rheological behaviors of the MCF slurry is weakened, leading to the decrease of the polishing forces in reality. As a result, the simulated result exerts the same tendency in polishing performance and is well compatible with the experimental results, demonstrating that the prediction model is established effectively.

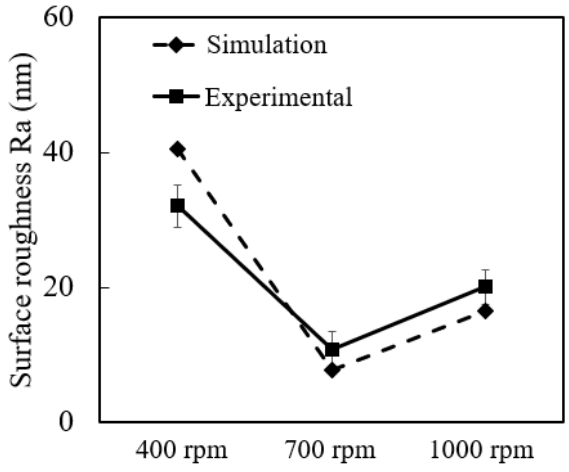

Fig. 4.8 Variation of tangential force F_t with revolution time t.

According to the results of polishing forces and surface roughness, it is concluded that the surface roughness evolves instantly when the peaks at the surface profile are continuously sheared off from the workpiece. In this case, the polishing conditions for desired surface roughness can be predicted by the surface roughness prediction model in advance, and then obtained conveniently in practice by giving the corresponding revolution speed of the workpiece when the polishing method is applied to the industry.

Summary

(1) The material removal was explained by establishing the material removal model with the signal abrasive particles in this chapter. Once normal force induces the AP to insert into the work surface and tangential force is powerful to shear the material off from the surface, the surface roughness changes instantly.

(2) The numerical model for predicting surface roughness was established successfully and was verified to be effective through the experiments. The effective polishing conditions can be obtained in advance for obtaining the desired surface roughness.

References

[1] Barman A, Das M. Simulation of Magnetic Field Assisted Finishing (MFAF) Process Utilizing Smart MR Polishing Tool[J]. Journal of The Institution of Engineers (India): Series C, 2017, 98(1):75-82.

[2] D. Golini, W.I. Kordonski, P. Dumas, S. Hogan, Magnetorheological finishing (MRF) in commercial precision optics manufacturing. 1999, Proc. SPIE 3782:80–91.

[3] A. Katiyar, A.N. Singh, P. Shukla, T. Nandi, Rheological behavior of magnetic nanofluids containing spherical nanoparticles of Fe–Ni. Powder Technol. 2012, 224:86–89.

[4] Jha S, Jain V K. Modeling and simulation of surface roughness in magnetorheological abrasive flow finishing (MRAFF) process[J]. Wear, 2006, 261(7):856-866.

[5] Stradling A W. The physics of open-gradient dry magnetic separation [J]. International Journal of Mineral Processing, 1993, 39(1-2):1-18.

[6] Shinmura T, Takazawa K, Hatano E, et al. Study on Magnetic Abrasive Finishing [J]. CIRP Annals - Manufacturing Technology, 1990, 39(1):325-328.

[7] Kansal H, Singh A K, Grover V. Magnetorheological nano-finishing of diamagnetic material using permanent magnets tool [J]. Precision Engineering, 2017, 51:30-39.

[8] Torres A, Luis C J, Puertas I. EDM machinability and surface roughness analysis of TiB2 using copper electrodes [J]. Journal of Alloys and Compounds, 2016, 690:337-347.

[9] Singh A K, Jha S, Pandey P M. Mechanism of material removal in ball end magnetorheological finishing process[J]. Wear, 2013, 302(1-2):1180-1191.

[10] Sidpara A, Jain V K. Analysis of forces on the freeform surface in magnetorheological fluid-based finishing process[J]. International Journal of Machine Tools and Manufacture, 2013, 69(3):1-10.

[11] Sidpara A, Jain V K. Experimental investigations into surface roughness and yield stress in magnetorheological fluid-based nano-finishing process[J]. International Journal of Precision Engineering and Manufacturing, 2012, 13(6):855-860.

[12] Li M, Lyu B, Yuan J, et al. Evolution and equivalent control law of surface roughness in shear-thickening polishing[J]. International Journal of Machine Tools and Manufacture, 2016, 108:113-126.

[13] Shiou F J, Asmare A. Parameters optimization on surface roughness improvement of

Zerodur optical glass using an innovative rotary abrasive fluid multi-jet polishing process[J]. Precision Engineering, 2015, 42:93-100.

Chapter Ⅴ Experimental Investigation on Polishing Aspheric Surfaces

5.1 Introduction

As engineering applications, the MCF slurry was successfully applied to polish various surfaces with different materials, including flat workpieces constructed by stainless steel, polymers, optical glasses, ceramics, linear/circle-shaped V-groove made up of oxygen-free copper and Ni-P plated STAVAX [1]. According to the reports of Wu, Guo, and Wang, the polishing conditions was one of the key impacts on the polishing performance. For example, Furuya et al. polished a metal work surface utilizing the MCF polishing technique and optimized the experimental parameters [2]. Wu et. al. successfully polished a flat workpiece made of CVD-SiC and a Nano-precision surface was obtained by optimal polishing conditions, and a stainless-structured surface with deep rectangle grooves was also polished by them when the proper polishing trace, revolution speed of magnet and working gap were given together. Guo et al. performed the polishing of a Ni-P plating layer [3] and PMMA [4] with the mount-shaped MCF polishing tool using a zirconia-coated CIP-based MCF slurry to the nanometer-level without causing scratches or the embedding of particles, and the results showed that the tool marks were diminished totally and ZrO_2-coated CIPs based MCF slurry produced smoother work surface at a higher improvement rate than ZrO_2-coated CIPs based MR fluid slurry, and the MCF slurry with 70 wt.% CIPs concentration and without APs and α-cellulose resulted in better surface roughness (R_a < 1 nm).

Considering high material removal rate, form accuracy, and surface quality by using the mount-shaped MCF polishing tool, Wang et al. polished efficiently a miniature V-groove using MCF slurry after optimizing the polishing conditions with revolution of MCF carrier 10 rpm, MCF slurry supplied amount 1 ml, and oscillation parameter 30 Hz [5]. Furthermore, Wang et. al investigated the effect of parameters on polishing circle-shaped V-groove and the results showed that the higher rotational speed of workpiece contributed to the better surface roughness and form accuracy [6]. In the report of Jiao [7], it was found that the Nano-precision surface of the optical glass was obtained with a high material removal rate when the higher rotation speed of the MCF wheel and smaller working gap were employed. According to the reports, it was implied that the performance of the MCF polishing tool was highly dependent on the polishing conditions, in the case of which, in order to polish aspheric surface, the investigation on the effect of parameters on polishing results were crucial.

As summarized in previous chapters, the polishing feasibility using the MCF tool was confirmed, the optimal MCF tool was obtained, and the material removal model was clarified. However, the works on polishing aspheric surfaces were still not conducted. As mentioned in the introduction, the polishing was mainly used for removing the tool marks and improving the surface quality. Hence, the investigations on the effect of parameters on polishing results in terms of material/tool marks removal, and surface quality were experimentally studied in this chapter, followed by the polishing aspheric surface with the optimized polishing conditions.

5.2 Experimental details

5.2.1 Experimental conditions

To systematically study the characteristic of the novel method and its polishing ability on aspheric surfaces, experiments were carried out in two steps. In the first step, the conic surface, which was regarded as a special aspheric surface, was polished to reveal the fundamental processing characteristics of the proposed method. The process parameters (*h*, *V*, n_c, CIP concentration, APs size) were subsequently optimized in terms of the material removal rate *MRR*, the polishing area, and the surface roughness. Finally, the aspheric surface was polished using the optimized MCF tool and the parameters to confirm the performance of the novel method.

Table 1 Experimental conditions in the experiments

Parameters	Value
Working gap *h* (mm)	1, 1.5, 2, 2.5, 3, 3.5
Volume of MCF supplied *V* (ml)	1, 1.5, 2, 2.5
Eccentricity r_e (mm)	4
MCF carrier revolution speed n_c (rpm)	200, 300, 400

Table 2 Different MCF slurries

	CIPs (wt.%) with diameter ~ 5μm	MF (wt.%)	APs (wt.%)	*α*-cellulose (wt.%)
MCF 1	55	30		
MCF 2	45	40	12 (1 μm)	
MCF 3	35	50		3
MCF 4	45	40	12 (0.5 μm)	
MCF 5	45	40	12 (2 μm)	

Table 1 shows the conditions used in the experiments by considering the variations in the working gap h, the volume of MCF slurry supplied V, and the revolution speed of MCF carrier n_c. Then, the MCF 1-5 slurries were supplied by changing the CIPs concentration and APs size, as shown in Table. 2.

5.2.2 Preparation of workpieces

The conic workpiece used in chapter 3 was considered as the workpiece in the first step. An aspheric element pre-turned by SDPT with design parameters k = -1 and c = 0.1 (Fig. 3(b)) was prepared with approximately a 49-nm initial surface roughness Ra.

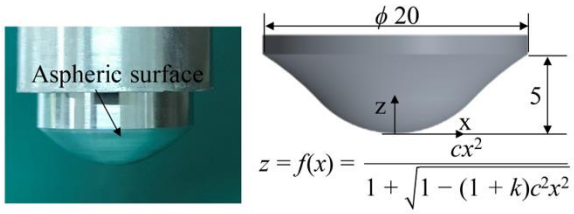

Fig. 5.1. Appearance of the aspheric surface.

5.3 Typical material removal

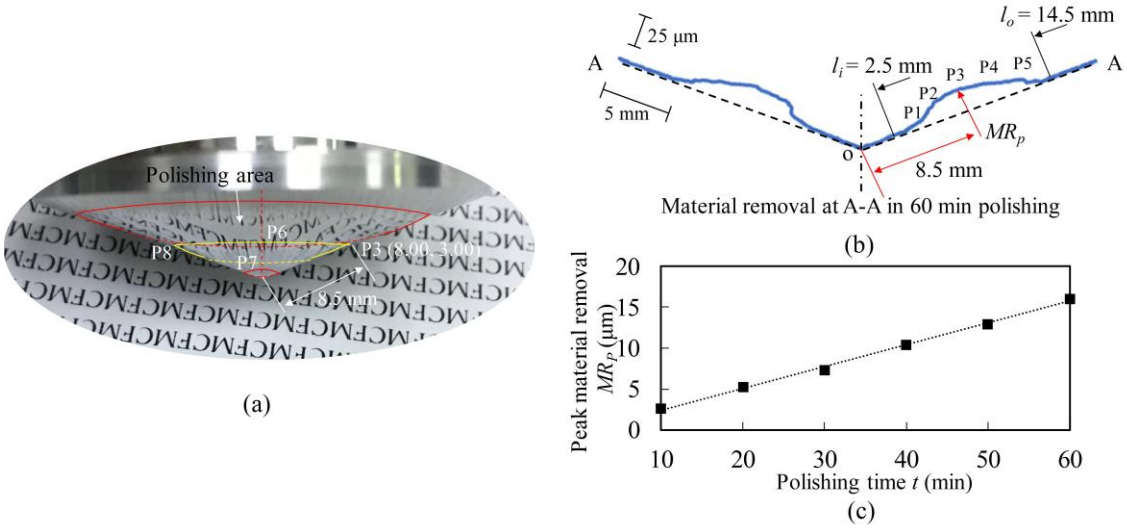

Fig. 5.2. (a) The polished workpiece, (b) surface profile, and (c) the peak material removal.

A conic surface was polished using the optimized MCF tool obtained in chapter 3. The geometric arrangement between the workpiece and the MCF tool was the same as that used in chapter 3. An optical photograph of the polished workpiece is presented in Fig. 5.2(a), demonstrating that the annular mirror surface was obtained successfully after polishing. Additionally, the symmetrical V-shaped generatrix at the A-A surface profile is shown in Fig. 5.2(b). The annular polished area (displayed in Figs. 5.2(a)) was obtained with l_o = 14.5 mm and l_i = 2.5 mm (shown in Figs. 5.2(b)). The polishing area S can be calculated by the equation $S = S_{l_oRl_o} - S_{l_iRl_i} = \pi l_o R_{l_o} - \pi l_i R_{l_i}$, where the radii, i.e., R_{l_o} and R_{l_i}, can be calculated as follows: $R_{l_o} = l_o\cos\alpha$, $R_{l_i} = l_i\cos\alpha$. Therefore, about 580 mm^2 of the polishing area was obtained in this experiment.

To systematically study the material removal, several points on the A-A profile with different depths of material removed were selected, as shown in Fig. 5.2(b). The peak of material removal, i.e., the maximal depth of the polishing area MR_P, was found at point P3, which was about 8.5 mm from point o along the generatrix. Thus, the material removal rate (MRR_p) was calculated by dividing the MR_P by the polishing time, e.g., a 0.27 μm/min material removal rate was obtained at P3. The MRR_ps were determined at several other points. P1 and P5, where the MRRs were about 0.05 μm/min, were located 3 and 4.7 mm from P3, respectively. P2 and P4, where the MRR_ps were about 0.13 μm/min, were located 2.8 and 3.2 mm from P3, respectively. Moreover, as shown in Fig. 5.2(c), the material was removed stably at P3 during the processing. Compared with previous methods [8–11], the novel method used in this experiment is suitable for removing material controllably due to

the steady material removal ability, which is convenient for planning a polishing path to polish the whole aspheric surface.

5.4 Removal process of tool marks

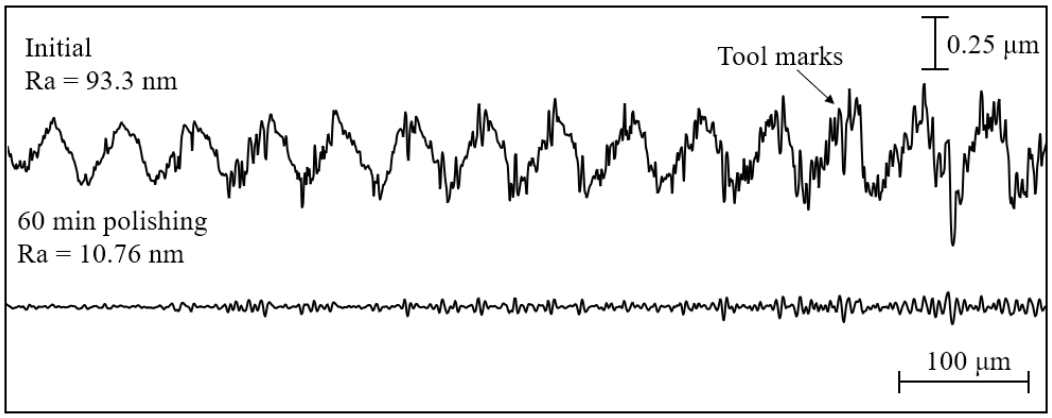

Fig. 5.3. Removal of tool marks.

An enlarged cross-section profile of the annular polished area around point P is displayed in Fig. 5.3 to compare the tool marks before and after polishing and confirm the ability of this novel method to remove the cutting marks. As is evident in this figure, the initial surface profile was composed of periodic peaks and valleys (maximum peak-to-value distance (PV): 0.749 μm) with a certain frequency, and the surface roughness Ra was approximately 93 nm. After polishing for 60 min, the surface roughness decreased to Ra 10.76 nm, and the surface profile was mainly composed of periodic peaks and valleys (PV: 0.147 μm) with a relatively high frequency, indicating that the removal of tool marks was successfully realized. The removal rate of tool marks, MRR_t, was obtained by dividing the difference of the PV before and after polishing by the polishing time, e.g., an MRR_t of 0.01 μm/min was obtained at point P.

5.5 Typical surface roughness

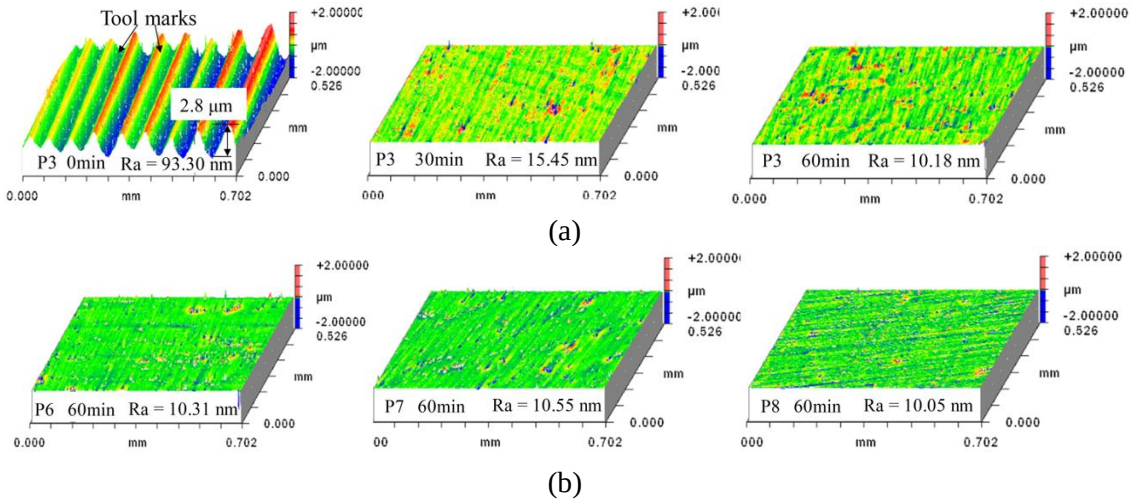

Fig. 5.4. (a) Surface roughness topographies at P3 after different polishing times and (b) surface topographies in different positions along the circumference of the polishing area after 60 min of polishing.

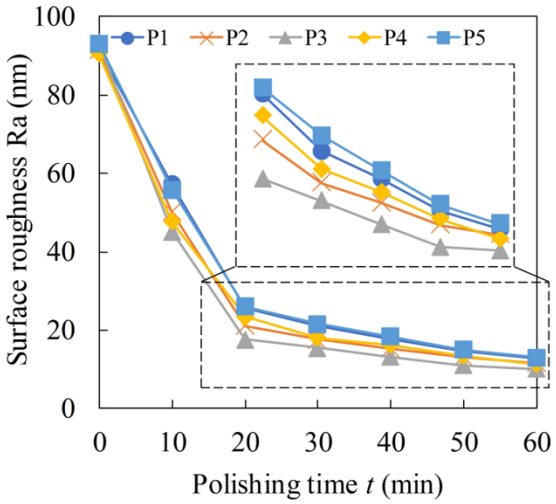

Fig. 5.5. Variations in the surface roughness at P1–P5 during polishing.

The typical variations in surface topographies with the polishing time at P3 are presented in Fig. 5.4(a). The tool marks with a maximum depth of 2.8 μm on the initial surface were progressively eliminated after polishing due to the gradual removal of material. This led to a vast improvement in the surface quality at P3, with Ra values ranging from 93.3 to 10.18 nm. To compare the surface roughnesses at different

positions along the circumference of the polishing area, P6, P7, and P8 were selected with a constant interval along the circle on which P3 was located, as shown in Fig. 5.2(a). After, the surface topographies at P6–P8 after 60 min of polishing were investigated, as shown in Fig. 5.4(b). All the surfaces were smoothed without tool marks. Furthermore, small deviations of the surface roughness at P3 and P6–P8 were found because the stable capacity of the material removal allowed the tool marks to be removed evenly and equally at the circumference. Hence, the investigation of surface roughness at the circumference is not considered henceforth.

The variations in the surface roughness at P1–P5 were investigated, as shown in Fig. 5.5. Regardless of the selected points, the surface roughness decreased continually during polishing. The surface roughness at P3 decreases rapidly in the first 20 min, after which the decrease rate decreased gradually. Similar trends were observed at other points. Analyzing the results, it was concluded that the best surface roughness was obtained at P3. Small deviations of the surface roughness were found between P1 and P5 and P2 and P4. However, a better surface roughness was observed at P2 and P4 than at P1 and P5. This was due to the higher *MRR*, which corresponded to fewer remaining tool marks at the surface, resulting in a better surface roughness.

5.6 Effect of process parameters

5.6.1 Effect of working gap *h*

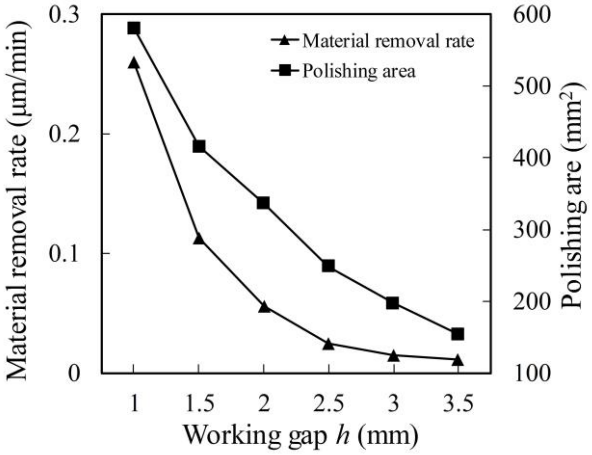

(a)

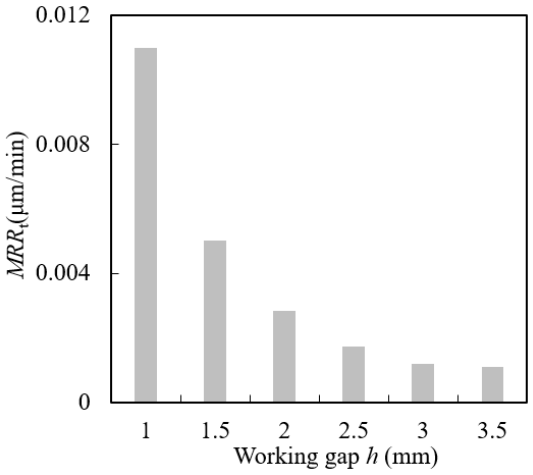

(b)

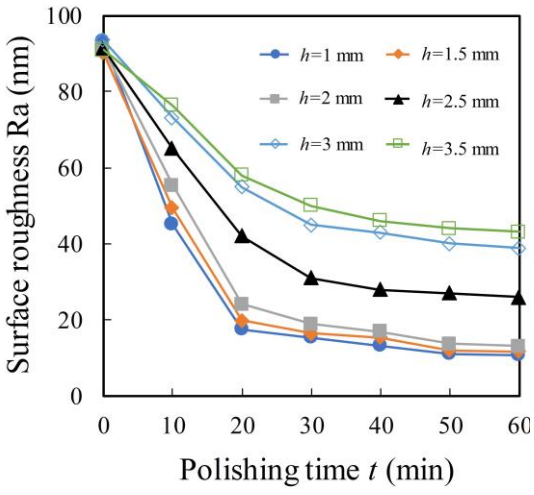

(c)

Fig. 5.6. Effect of working gap *h* on (a) MRR_p, polishing area, (b) MRR_t and (c) surface

roughness.

The effects of the working gap h on the MRR_p, polishing area, MRR_t and surface roughness are reviewed in Fig. 5.6. As shown in Fig. 5.6(a), the MRR_p and polishing area significantly decreased as h was adjusted from 1 to 2.5 mm and slightly decreased as h increased from 2.5 to 3.5 mm. During this period, the polishing area was more affected than the MRR_p. As h increased, the MCF slurry within the working area became less compressed and stiffer, eventually resulting in a decreased indented pressure of the particles on the work surface and less working area, corresponding to a lower MRR_p and smaller polishing area.

The effect of the working gap h on the removing tool marks is investigated, as shown in Fig. 5.6(b). The removal efficiency of tool marks came up to 0.011 μm/min when working gap h reached to 1 mm. As the increase of the working gap h, the removal efficiency of tool marks sharply decreased, especially when working gap h increased from 1 mm to 2.5 mm, then the decreasing tendency slowed down.

As the typical results in Fig. 5.6(c), the effect of the working gap h on the surface roughness at P3 is investigated. The surface roughness decreased with the increase in polishing time. The same tendency for the surface roughness variation was found, although h was varied. Once h exceeded 2 mm, a conspicuous deviation of the surface roughness was observed by comparing it with other conditions. The best surface roughness was achieved when h was 1 mm.

5.6.2 Effect of n_c

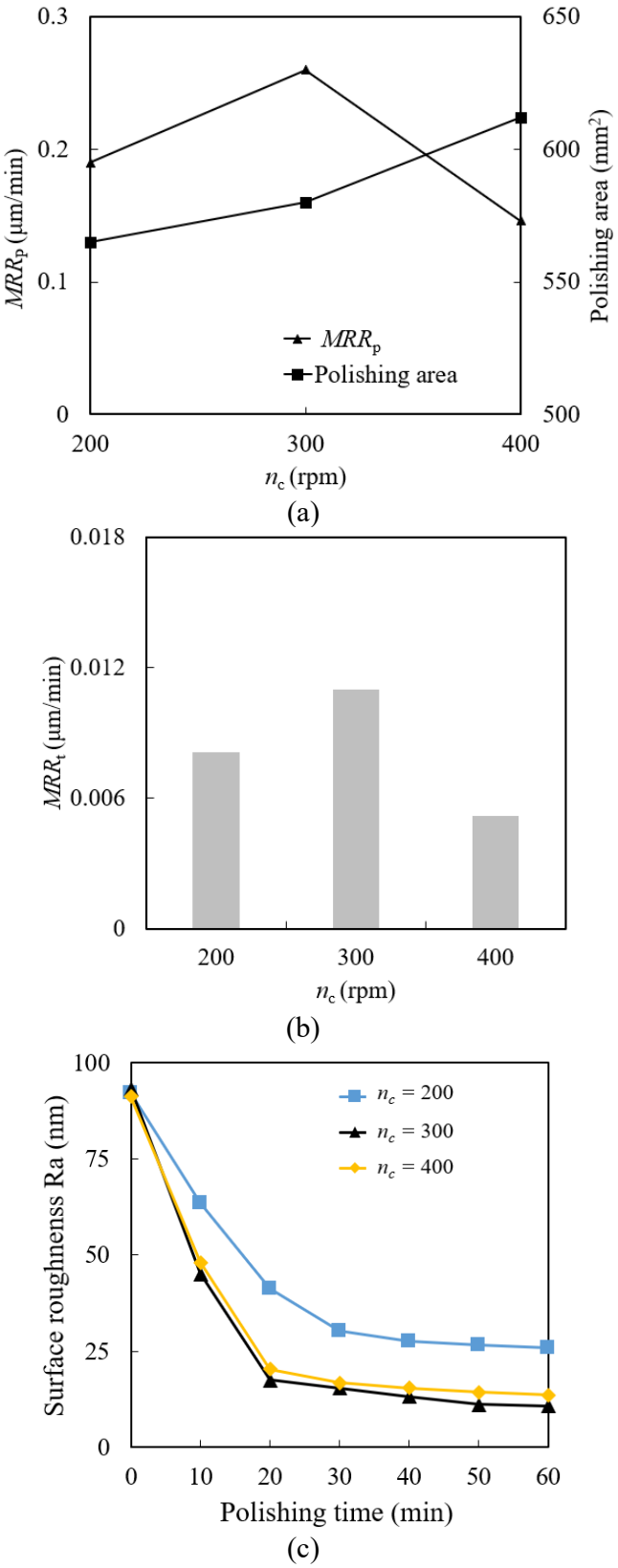

Fig. 5.7. Effect of n_c on (a) MRR_p, polishing area, (b) MRR_t and (c) surface roughness.

The effects of the working gap h on the MRR_p, polishing area, MRR_t and surface roughness are reviewed in Fig. 5.7. Fig. 5.7(a) shows that the MRR_p increases first from 200 rpm to 300 rpm. It was concluded from Guo's work that MRR_p had a positive relationship to the relative speed between MCF tool and workpiece, because higher speed resulted in the increase of shear stress, i.e., tangential force. However, the MRR_p decreased when n_c increased from 300 to 400 rpm. When n_c was raised to 400 rpm, the components within the MCF slurry, especially the abrasive particles, were split out from the MCF tool, due to the overlarge centrifuge force. Thus, the slight decrease in MRR_p occurs. As to the polishing area, it was a slight increase with the increase in n_c due to the splitting out of MF and other components. As shown in Fig. 5.7(b), the removal efficiency on tool marks increases when n_c increased from 200 rpm to 300 rpm, then it decreased at 400 rpm. The reason should be that the viscosity and the shear stress were changed abruptly due to the change of the compositions of the MCF tool.

The evident differences in the surface roughness are found with different n_c, as shown in Fig. 5.7(c). When n_c was set at 200 rpm, the final surface roughness Ra was much worse than that at 300 rpm and 400 rpm. However, worse surface roughness was found at 400 rpm compared with 300 rpm. This was because the amount of CIPs taking participate into cutting material off was sharply increased after APs were split out from the MCF tool also due to the overlarge centrifuge force. These results exerted that n_c = 300 rpm was suitable for this polishing method though overall consideration.

5.6.3 Effect of volume of MCF slurry supplied

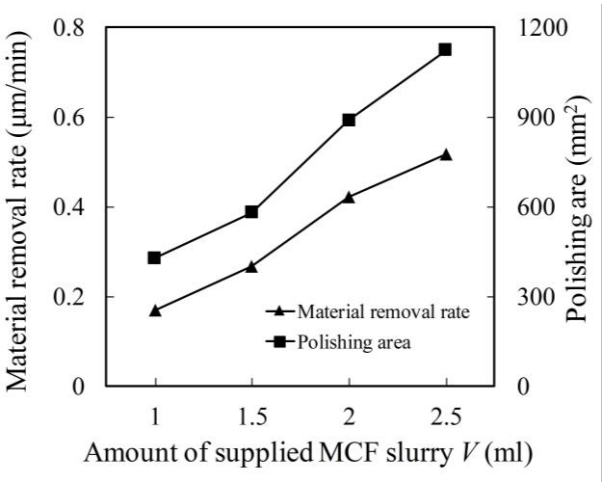

(a)

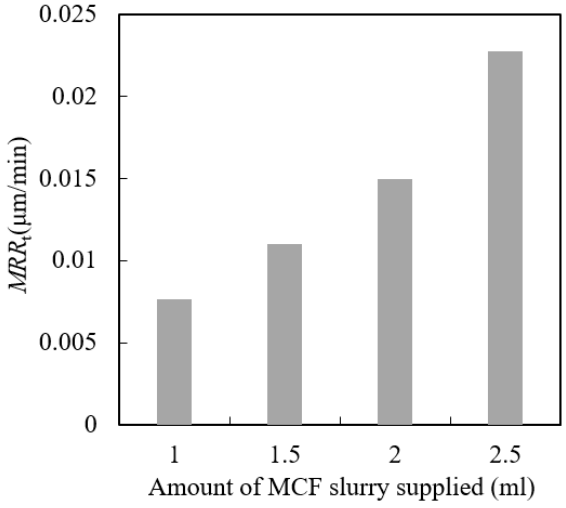

(b)

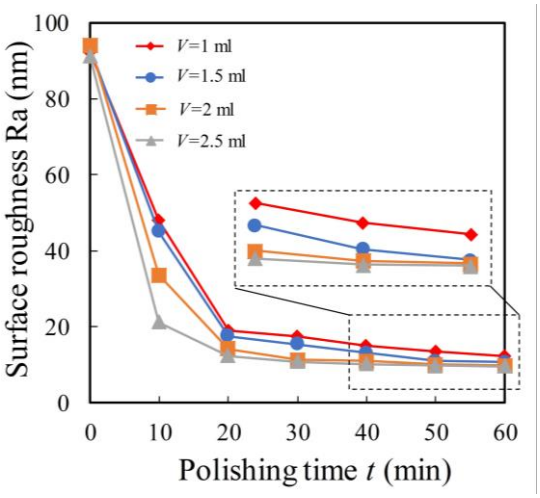

(c)

Fig. 5.8. Effect of amount of MCF slurry supplied on (a) MRR_p, polishing area, (b) MRR_t and (c) surface roughness.

Fig. 5.8 shows that the effect of the amount of MCF slurry supplied on MRR_p, polishing area, and MRR_t. As shown in Fig 5.8(a), MRR_p and polishing area increased almost linearly with the increase in V. It was concluded from chapter 3 that a wider and higher MCF tool was obtained with a larger V, demonstrating that longer clusters formed. Once longer clusters were compressed to the same h, higher indented pressure and larger working area were obtained, leading to a higher MRR_p and larger polishing area. As displayed in Fig. 5.8(b), MRR_t increased as the increase in amount of MCF slurry supplied. When the amount of MCF slurry increased, the number of CIPs within MCF tool was enhanced, resulting in an increase in the number ferric clusters. Consequently, the ability on removal of material/tool marks was improved.

As to the variation of the surface roughness under different amounts of MCF slurry supplied with polishing time, there were no evident differences in Fig 5.8(c) in the surface roughness after 60 min of polishing when V was greater than 1 ml. This occurred because the varied parameters led to a different MRR_p, which resulted in a different surface roughness at the work surface, as was concluded in the previous section. Based on an overall consideration of the appearance of the MCF tool shown in chapter 3, and the polishing results, 1.5 ml of the MCF slurry was suitable for polishing the aspheric surface.

5.6.4 Effect of CIPs concentrations

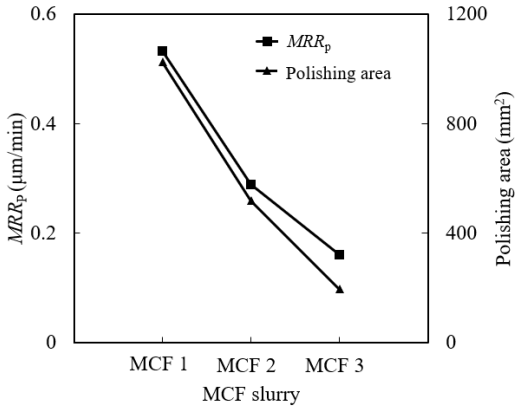

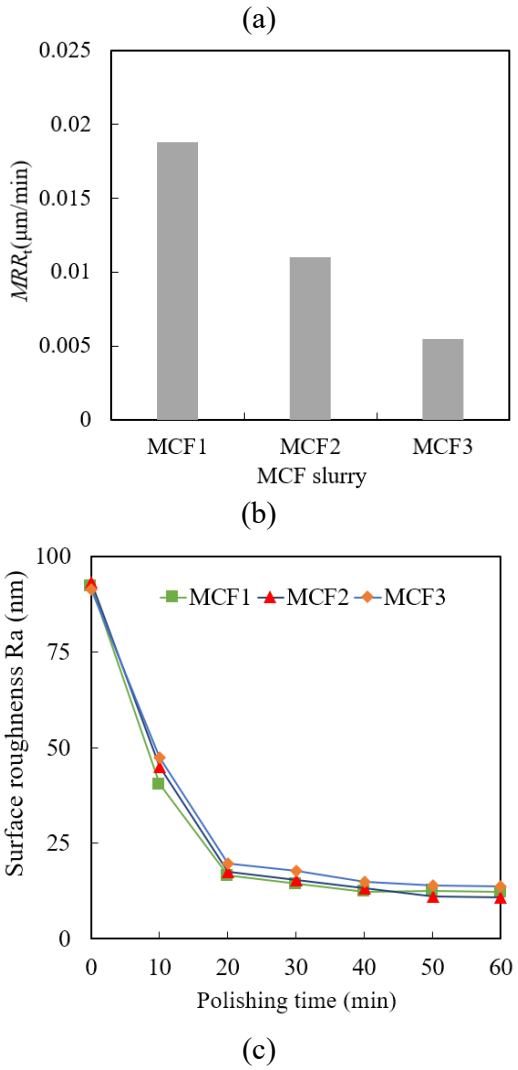

Fig. 5.9. Effect of the CIPs concentration on the (a) MRR_p and polishing area, (b) MRR_t, and (c) Surface roughness Ra.

Fig. 5.9 shows the effect of the CIPs concentration on MRR_p and polishing area, MRR_t and surface roughness Ra obtained using different MCF slurries with different CIPs concentrations. The MCF 1 slurry with the highest CIPs concentration enabled the formed MCF tool to achieve the highest MRR_p, polishing area, and MRR_t, as shown in Figs. 5.9(a) and (b). With a decrease in the CIPs concentration, the MRR_p, polishing area, and MRR_t decreased. As for the work-surface roughness (Fig. 5.9(c)), the work-surface could be polished using the MCF tools formed with different MCF slurries. However, MCF 1 exhibited the greatest polishing efficiency in the first 40 min

polishing, whereas the surface roughness Ra began to worsen after 40 min. In contrast, other MCF slurries smoothed the surface gradually with increased polishing time.

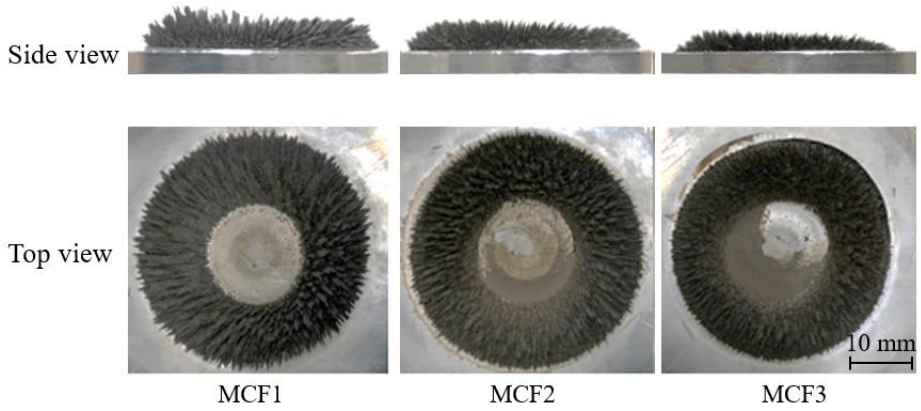

Fig. 5.10. Appearances of the MCF tools.

Optical images of MCF tools with different CIPs concentrations are shown in Fig. 5.10. With the MCF 1 slurry, the MCF tool with the longest ferric clusters was obtained. With the decrease in the CIPs concentration, the geometry of the MCF tools was reduced, because of the decrease in the amount of CIPs within the MCF slurries, leading to a decrease in the number and the lengths of the formed ferric clusters.

As the CIPs concentration decreased, the corresponding *M* gradually decreased under the applied magnetic field. Consequently, the ferric clusters were prone to becoming fractured during polishing, decreasing the shear stress, as summarized in chapter 2. Furthermore, the magnetic properties of the slurry were weakened, which also weakened the effect of the APs. Thus, the polishing forces were reduced, directly leading to a decrease in the capacity to remove material/tool marks. Although the MCF 1 exhibited a prominent polishing ability, its working life was limited due to the rapid evaporation of water during polishing and the subsequent significant change of the viscosity, which were adverse to the surface polishing. Based on the characteristics of the obtained MCF tools, different MCF tools can be used in different processes. For example, MCF 1 can be selected for rough

polishing because it exhibited the highest MRR_p and MRR_t, and MCF 2 can be used for fine polishing. In the rest of this study, only MCF 2 slurry was used to examine the polishing efficiency and final surface roughness.

5.6.5 Effect of APs sizes

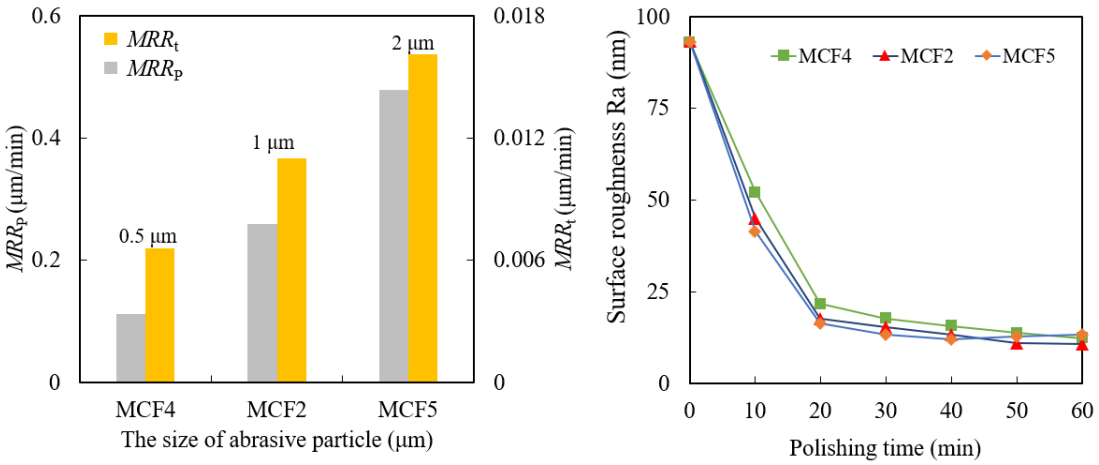

(a) (b)

Fig. 5.11. Effect of the sizes of APs on (a) MRR_p and MRR_t, and (b) the surface roughness Ra.

The effects of the sizes of the APs on MRR_p, MRR_t, and the surface roughness Ra are shown in Fig. 5.11. As shown in Fig. 5.11(a), MRR_p and MRR_t gradually increased as the size of APs increased, indicating that larger APs were beneficial for the removal of work-material and tool marks. As for the surface quality, the surface roughness Ra could be improved by using different APs, as shown in Fig. 5.11(b). Different variation tendencies of Ra during polishing were found. When the sizes of APs were 2 μm, within the first 40 min of polishing, the greatest polishing efficiency was obtained. However, in the following 20 min of polishing, the surface roughness Ra tended to deteriorate.

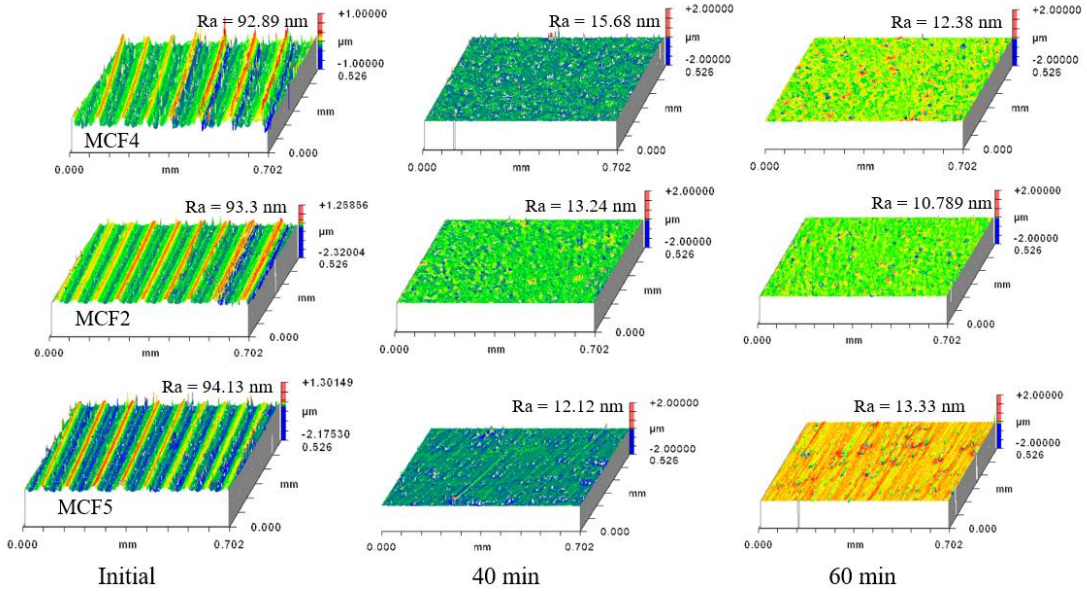

Fig. 5.11. Surface topography in the initial state and after 40 min, 60 min of polishing with the MCF 4, MCF 2, and MCF 5 slurries.

To illustrate the reason for the different variations of Ra, the variation of the work-surface morphologies during polishing is shown in Fig. 5.11. The meteor-shaped tracks (localized pits followed by long tails, as indicated in Fig. 5.11) induced by APs on the work-surface were evident when the sizes of the APs were 2 μm, which were not present when other APs were used. When larger APs were used, although the number of the APs participating in polishing was reduced per unit time, the influence of the magnetic field on every individual abrasive particle in the working area was significantly strengthened, and thus, the interference between the abrasive particle and work-surface was greater. Thus, the APs squeezed the work-surface more tightly and could even be embedded in the work-surface. In this way, the cutting depth induced by a single abrasive particle increased, hindering the micro-cutting and rolling motions of the abrasive particle when an abrasive particle had a velocity relative to the work-surface, creating meteor-shaped tracks on the work-surface. Additionally, although more materials could be removed due to the greater cutting depth,

the sub-surface damage including the micro-cracks and residual stress were induced inevitably by the large abrasive particle, which was harmful to the surface quality. On the contrary, small cutting depth and much more fluent cutting motion were obtained when smaller APs were employed. Therefore, better surface quality could be obtained, but the removal efficiency of the material/tool marks decreased. APs with 1 μm of diameter were used in this work.

5.7 Aspheric surface polishing

An aspheric workpiece pre-manufactured by SPDT was used to prove the capability of the proposed method to polish aspheric surfaces. The tilt angle was ensured at 20° by the choice of Point P (3.60, 0.52) in the x_0oz_0-plane on the work surface. Under the same conditions with conic surface polishing, an experiment on polishing aspheric surfaces was conducted for 60 min. During polishing, the MCF slurry was refreshed every 5 min to prevent the polishing ability of the MCF tool from being deteriorated.

The typical 3D-micro optical images of the surface morphology at point P during polishing are shown in Fig. 5.12. The tool marks, which were distributed regularly on the initial surface, were removed gradually during polishing. At the end of polishing, the tool marks almost disappeared. To reflect intuitively the variation in the surface roughness, the typical C-C profiles on the corresponding surface morphologies (shown in Fig. 5.12) are shown in Fig. 5.13. The surface was smoothed successfully, and Ra decreased from 49.81 to 10.77 nm after 60 min of polishing.

Furthermore, the A-A surface profiles before and after polishing were compared to discuss the shape retention, as shown in Fig. 5.14. The active polishing area was limited

between -8.30 and 8.30 mm. The shape retention was evaluated by the index Pearson correlation coefficient (Pcc), which is employed widely to estimate the agreement of a linear correlation with a series of samples. This procedure can be executed in MATLAB using built-in functions. The Pcc reached 0.9981, meaning that this method exhibited a high shape retention ability for polishing this kind of aspheric surface.

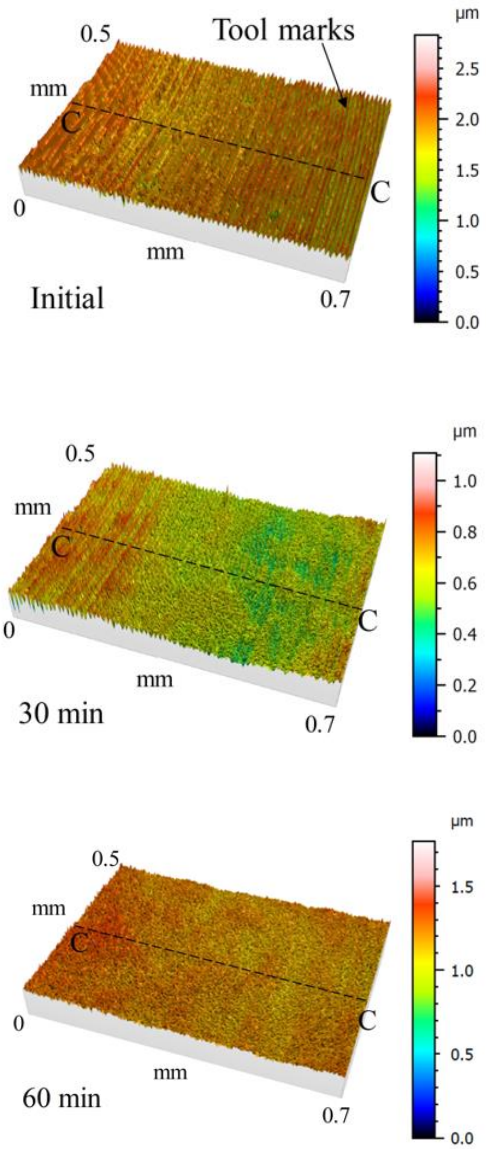

Fig. 5.12. The typical 3D micro-optical image of the surface morphology initially, after 30 min of polishing, and after 60 min of polishing.

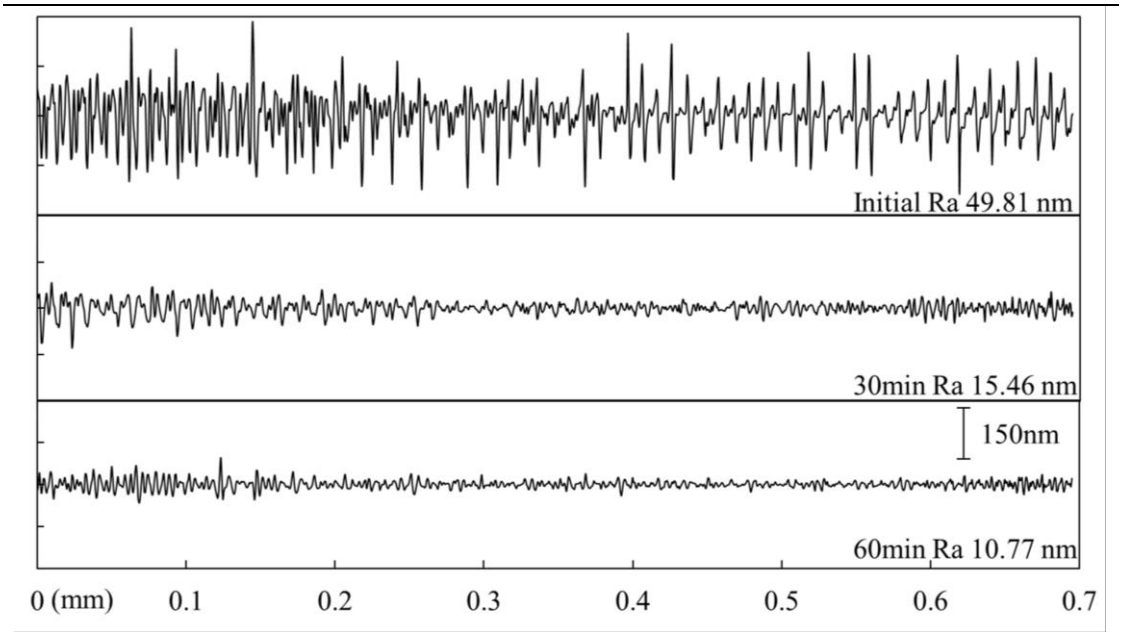

Fig. 5.13. The typical surface roughness initially, after 30 min of polishing, and after 60 min of polishing.

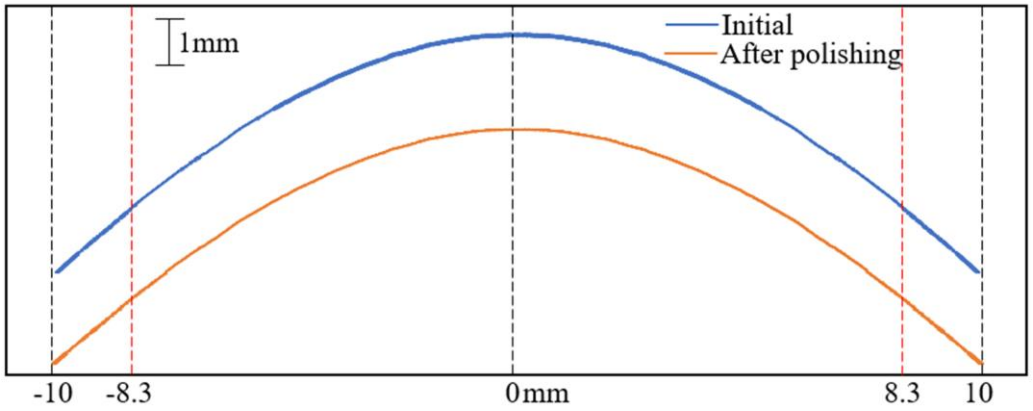

Fig. 5.14. Work surface profiles before and after polishing for 60 min.

As can be figured out also, in this work, only the convex work surface was dealt with because the purpose of the present work was to confirm the feasibility of the proposed method on polishing aspheric surfaces. However, under the similar consideration as mentioned above, the doughnut-shaped MCF tool has the potentiality for polishing concave work surfaces as long as the MCF tool is prepared with appropriate structure and dimension

and the polishing conditions including the motion path of the MCF tool are determined properly. The details will be discussed in future works.

Summary

(1) A V-shaped generatrix was obtained on the polished conic surface. A similar surface roughness at the circumference and different surface roughness on the generatrix were found. The tool marks composited of periodic peaks and valleys with relatively low frequent were diminished gradually with the polishing time.

(2) A smaller working gap was proper for polishing. The 1 mm of working gap h was selected in the experiments.

(3) The larger amount of MCF slurry was applied, and a larger material removal rate, larger polishing area, and better surface roughness were achieved.

(4) Higher revolution speed of MCF carrier n_c was beneficial for obtaining higher material removal rate, larger polishing area, higher efficiency in removing tool marks and better surface roughness.

(5) The CIPs concentration affected positively the magnetization M of the MCF slurry, leading to better performance on the material/tool marks removal rate when a higher CIPs concentration was applied. However, the best surface quality was attained with the CIPs concentration of 45 wt.% in this study, rather than 55 or 35 wt.%.

(6) Larger APs were beneficial for obtaining higher material/tool marks removal rates. However, a better surface quality was achieved when the APs of 1 μm in diameter were preferred rather than 0.5 or 2 μm.

(7) The aspheric surface was polished successfully without the tool marks on the surface. Furthermore, the shape of the workpiece was kept in a favorable extent.

References

[1] Guo H, Wu Y. Ultrafine polishing of optical polymer with zirconia-coated carbonyl-iron-particle-based magnetic compound fluid slurry. Int J Adv Manuf Tech 2015;85:253-61.

[2] E. J. Polishing PMMA and other optical polymers with magnetorheological finishing. 2003.

[3] Singh AK, Jha S, Pandey PM. Design and development of nanofinishing process for 3D surfaces using ball end MR finishing tool. International Journal of Machine Tools & Manufacture. 2011;51:142-51.

[4] Khan DA, Alam Z, Jha S. Nanofinishing of Copper Using Ball End Magnetorheological Finishing (BEMRF) Process. International Mechanical Engineering Congress & Exposition 2016.

[5] Sidpara A, Jain VK. Analysis of forces on the freeform surface in magnetorheological fluid based finishing process. International Journal of Machine Tools and Manufacture. 2013;69:1-10.

[6] Nikitin DB, Evteev GV, Khimich YP. Optical shaping of a large aspheric mirror composed of silicon carbide. Journal of Optical Technology C/c of Opticheskii Zhurnal. 2007;74:133-4.

[7] Shimada K, Akagami Y, Kamiyama S, Fujita T, Miyazaki T, Shibayama A. New Microscopic Polishing with Magnetic Compound Fluid (MCF). Journal of Intelligent Material Systems and Structures. 2002;13:405-8.

Chapter Ⅵ Conclusions and Future Suggestions

Aspheric elements have become essential optical surfaces for modifying optical systems due to their abilities to enhance the imaging quality. However, the tool marks and sub-damage were remained inevitably by the pre-manufacture techniques, such as the single point diamond turning (SDPT) and the high precision grinding. In order to improve the surface quality, the polishing process was demanded to eliminate these defects. The magnetic field-assisted polishing method was prominent for this purpose. A magnetic compound fluid (MCF) was developed by compositing a magnetic field (MF) and a magnetorheological (MR) fluid. The MCF contains not only μm-sized iron particles but also nm-sized magnetite particles, whereas there are no nm-sized magnetite particles within the MR fluid. MCFs exhibited higher magnetic pressure and apparent viscosity than MFs and a better dispersity of nonmagnetic particles than MR fluids under a magnetic field while maintaining a fluid-like behavior. The MCF slurry contains usually carbonyl-iron-particles (CIPs), water-based MF with nm-sized magnetite particles, abrasive particles, and α-cellulose. By the inspiration of conventional MCF polishing tool, i.e., mount-shaped MCF tool and MCF wheel, a novel doughnut-shaped MCF tool was proposed for polishing aspheric surfaces. Under a rotary magnetic field generated by the revolution of the ring-magnet, the magnetic flux density was constant but the magnetic lines of force constantly revolved around the MCF carrier, leading the clusters formed by CIPs to alert their orientations to stir abrasive particles. The renewing working area prolonged the life of the

MCF tool to a limited extent. In this study, polishing with the novel MCF polishing tool under a rotary magnetic field was extensively studied from the investigation on feasibility polishing, the fundamental properties of the MCF tool (including the formation process, the optimal geometry of the MCF tool, and behavior of CIPs and APs), the analysis of the material removal (including the material removal model, polishing forces), and the investigation experimentally on the effect of parameters on removal of material/tool marks and surface quality. According to the results, the aspheric surface was polished successfully.

After recognizing the rules of the rheological behaviors of MCF slurry and thereby constructing the polishing setup, the investigation on feasibility polishing was conducted. The shear stress of the MCF 2 slurry increased with the increase in shear rate and magnetic field strength. Regardless of the magnetic field, when shear rate increased from 0 to 100 1/s, shear stress enhanced sharply and then a little decreased before shear rate reached 300 1/s, at last, it kept almost a small increase rate with the increase of shear rate. The maximum shear stress was almost 100 KPa when 0.8 T of magnetic flux density B and 1000 1/s of shear rate were applied. The viscosity of the MCF 2 slurry decreased with the increase in shear rate and increased with the increase in magnetic flux density B. When shear rate increased from 0 to 100 1/s, the viscosity decreased quickly, and then kept a small decrease rate as the increase in shear rate. With high magnetic field strength, MCF slurry was hard to change the character from a solid-like to a liquid, because the ferric clusters were much stronger than that with low magnetic field strength. Thus, the shear stress and viscosity were affected significantly by CIPs concentration and magnetic field strength. The top tip of the MCF tool was located at a distance D to the revolution center of MCF tool and

performed better ability on removing material. The D could be obtained by using $D = (d_i + d_o)/4$, i.e., the middle portion of the working area. The workpiece was polished to the nano-precision scale. Thus, it was certain that this method was potential for polishing materials.

The formation process of the MCF tool was affected by the eccentricity r_e, the rotation speed of the MCF carrier n_c, the revolution speed of the magnet n_m, and the amount of MCF slurry supplied V. Apart from the revolution speed of the magnet n_m, above parameters also affect significantly the geometry of the MCF tool. A perfect MCF tool could be obtained when the eccentricity r_e, the rotation speed of the MCF carrier n_c, the revolution speed of the magnet n_m, and the amount of MCF slurry supplied V were 4 mm, 300 rpm, 500 rpm, and 1.5 ml, respectively, resulting in a MCF tool with dimensions of a = 14.50 mm, b = 12.10 mm, c_1 = 0.12 mm, c_2 = 0.71 mm, d_o = 37 mm, and H = 5.00 mm. The CIPs were gathered to form the ferric clusters along the magnetic flux lines. The Aps, at a given working gap, can squeeze the work-surface. The squeezing action was much more intense when larger APs and the MCF slurry with a higher magnetization were employed. The material removal model suggested that the material was removed due to the APs and the relative motion between the work-surface and APs.

The material was removed by the normal force and tangential force. The normal force was contributed mainly by the resultant force of the magnetic levitation force and the gravitational force, whereas the tangential force was resulted by the shear force from APs and the resistant force from the workpiece. Once the indented depth of the AP was proper, and the shear force was greater than the resistant force of the material, the material was thereby removed. Models for simulating the polishing forces (the indentation model of a

single abrasive particle) and for predicting surface roughness were established according to the principle of material removal.

A V-shaped generatrix was obtained on the polished conic surface. A similar surface roughness at the circumference and different surface roughness on the generatrix were found. The tool marks composited of periodic peaks and valleys with relatively low frequent were diminished gradually with the polishing time. The surface roughness was no different in the circumference, but the different results were found along the generatrix. A smaller working gap was proper for polishing. The 1 mm of working gap h was selected in the experiments. The larger amount of MCF slurry was applied, and a larger material removal rate, larger polishing area, and better surface roughness were achieved. Higher revolution speed of MCF carrier n_c was benefit for obtaining higher material removal rate, larger polishing area, higher efficiency in removing tool marks and better surface roughness. The CIPs concentration affected positively the magnetization M of the MCF slurry, leading to better performance on the material/tool marks removal rate when a higher CIPs concentration was applied. However, the best surface quality was attained with the CIPs concentration of 45 wt.% in this study, rather than 55 or 35 wt.%. Larger APs were beneficial for obtaining higher material/tool marks removal rates. However, a better surface quality was achieved when the APs of 1 μm in diameter were preferred rather than 0.5 or 2 μm. The aspheric surface was polished successfully without the tool marks on the surface. Furthermore, the shape of the workpiece was kept to a favorable extent.

Future work should be done in order to clarify the work-life of the MCF tool, investigate the effect of the polishing path on the whole surface polishing and simulate the material

removal function. Based on the characteristic removal function, doughnut-shaped MCF tool has potential in finishing not only aspheric surfaces but also free-form surfaces by designing a certain polishing path.

Acknowledgements

This thesis work was finished within three years with the kindhearted help and full-hearted support of many people. This work would be impossible to be accomplished without them, they deserve the respects and appreciations. It is my pleasure to give my gratitude to those people who have continuously supported me over the past several years.

First and foremost, the sincere appreciation is given to my advisors, one is Prof. Yongbo Wu of Southern University of Science and Technology who has always supported my living and given suggestions to the thesis work with his patience, knowledge, and guidance, which are the best gifts in my study career. His rigorous attitude towards scientific research and life will guide me in my future research work and inspire me to go forward. I couldn't thank him more for his help in finishing this thesis work. The other one is Prof. Teruo Bitoh of Akita Prefectural University who gives me great supports in living in Japan and applying for my degree.

I would like to express my sincere gratitude to my advisor of master's course, Prof. Julong Yuan of Zhejiang University of Technology, for his continuous encouragement and support in my study. Thanks to his kindhearted recommendation for offering me such a precious opportunity to study under the guidance of Prof. Wu. These experiences learned from Prof. Yuan during the master's course have greatly benefited me in pursuing my doctoral degree.

Gratitude is also for Profs. Tsunehisa Suzuki, Mitsuyoshi Nomura, Tatsuya Fujii and Shi

Jian of Akita Prefectural University for their willingness to give the best help to me during my study.

My cordial thanks are extended to Prof. Youliang Wang of Lanzhou University of Technology, Dr. Sisi Li, Dr. Qiang Wang and Mr. Zongliang Yao for their kindly help, advice, and assistance in my work. The discussions with them always enlighten my thoughts and make things easier to deal with. Thanks also to Prof. Weixing Xu, Prof. Yaguo Li, Prof. Jianguo Cao, Prof. Huiru Guo for sharing their valuable experiences with me.

I would like to acknowledge the financial supports of Akita Prefectural University and Southern University of Science and Technology for my study and living.

Special gratitude goes to my friends and relatives in China for their encouragement and support.

Finally, I would like to express my heartiest appreciation to my parents, my sister and her family for their unconditional support and encouragement. I owe them a lot and appreciate their generous dedication to me. With their warm concerns, I will never feel lonely.

Accomplishments

- **国内学術講演会**

[1] 馮銘, 呉勇波, 野村光由，藤井達也. MCF スラリーを用いた自由曲面のロボット研磨に関する基礎研究. (2016. 10. 08)日本精密工学会东北支部秋季学術講演会.

[2] 馮銘，呉勇波，野村光由，藤井達也. ドーナツ型 MCF(磁気混合流体)研磨ツールを用いた非球面のナノ精度研磨．(2017. 03. 13)日本精密工学会春季学術講演会.

- **国際学術会議**

[1] Ming Feng, Yongbo Wu*, et.al. Fundamental research on polishing aspheric surfaces by the doughnut-shaped MCF (magnetic compound fluid) tool. (2017. 06. 09) The 14th China academic conference on cutting and advanced manufacturing technology.

[2] Ming Feng, Yongbo Wu*, et.al. Fundamental research on aspheric surface polishing using doughnut-shaped MCF polishing tool. (2017. 12. 03) The 20th International Symposium on Advances in Abrasive Technology.

[3] Ming Feng, Yongbo Wu*, et.al. Fundamental investigation on the polishing aspheric elements with doughnut-shaped MCF slurry. (2018. 09. 10) The 1th International Symposium on Extreme Optical Manufacturing and Laser-Induced Damage in Optics.

[4] Tengjiao Wang, Ming Feng, Yongbo Wu*. A Study on Surface Finish of Zirconia Ceramics Obtained by Magnetic Compound Fluid (MCF) Polishing. (2018. 09. 10) The 1th International Symposium on Extreme Optical Manufacturing and Laser-Induced Damage in Optics.

[5] Ming Feng, Yongbo Wu*, et.al. Aspheric surface polishing by using a doughnut-

shaped MCF polishing tool. (2018. 09. 26) The 7th International conference on Engineering and Innovative Materials.

[6] Wang Q, Wu Y B*, Lu D, Teruo Bitoh, Ming Feng. Experimental Investigation on the Tilt Helical Milling of Carbon Fiber Reinforced Plastics (CFRP). (2018. 09. 26) The 7th International conference on Engineering and Innovative Materials.

[7] Ming Feng, Yongbo Wu*, et.al. Polishing investigation on zirconia ceramics using magnetic compound fluid (MCF) slurry. (2019. 12. 08) The 22th International Symposium on Advances in Abrasive Technology.

[8] Youliang Wang, Feng Ming, Wu Y B*. Fundamental study on S-136 aspheric surface using magnetic compound fluid slurry. (2019. 12. 08) The 22th International Symposium on Advances in Abrasive Technology.

[9] Yingrui Xie, Yongbo Wu*, Ming Feng, et.al. Investigation on polishing of concave surfaces with magnetic compound fluid (MCF) slurry. (2019. 12. 08) The 22th International Symposium on Advances in Abrasive Technology.

- **学術論文**

【本学位論文に関連するもの】

[1] Feng M, Wu Y B*, Bitoh T, et al. Fundamental Investigation on the Polishing Aspheric Elements with Doughnut-Shaped MCF Slurry [J]. Key Engineering Materials, 2018, 792:179-184. (Ei)

[2] Feng M, Wu Y B*, Youliang Wang, Bitoh T, et al. Investigation on the polishing of aspheric surface with a doughnut-shaped magnetic compound fluid tool [J]. Precision Engineering, 2020, 61: 182-193. (IF: 2.685)

[3] Feng Ming, Youliang Wang, Bitoh T, Mitsuyoshi Nomura, Tatsuya Fujii, Wu Y B*. Polishing investigation on zirconia ceramics using magnetic compound fluid (MCF) slurry [J]. International Journal of Abrasive Technology. (Accepted, Ei)

[4] Feng M, Wu Y B*, Bitoh T, et al. The effect of the component of magnetic compound fluid (MCF) slurry on the polishing characteristics in aspheric surface finishing with the doughnut-shaped MCF tool, Precision Engineering. (Under

review, IF: 2.685)

【その他に関連するもの】

[5] Feng M, Wu Y B*, et al. Processing of high-precision ceramic balls with a spiral V-groove plate [J]. Frontiers of Mechanical Engineering, 2017, 12:132-142. (IF: 0.989)

[6] Wang Q, Wu Y B*, Lu D, Teruo Bitoh, Ming Feng. Experimental Investigation on the Tilt Helical Milling of Carbon Fiber Reinforced Plastics (CFRP) [J]. Key Engineering Materials, 2018, 792:173-178. (Ei)

[7] Youliang Wang, Feng Ming, Wu Y B*. Fundamental study on S-136 aspheric surface using magnetic compound fluid slurry [J]. International Journal of Abrasive Technology. (Under review, Ei)

- **特許**

[1] Wu Yongbo, Feng Ming. The novel polishing setup for polishing aspheric surface, CN 2019105222699

[2] Wu Yongbo, Feng Ming. The novel polishing method for polishing aspheric surface, CN 2019105222985

[3] Wu Yongbo, Feng Ming. The novel polishing setup for polishing aspheric surface, CN 2019209145076

[4] Wu Yongbo, Wang Tengjiao, Feng Ming. A novel polishing method with magnetic compound fluid (MCF) slurry, CN 2019105216895

[5] Wu Yongbo, Wang Tengjiao, Feng Ming. A novel polishing setup with magnetic compound fluid (MCF) slurry, CN 2019105216927

[6] Wu Yongbo, Wang Tengjiao, Feng Ming. A novel polishing setup with magnetic compound fluid (MCF) slurry, CN 2019209071867